NUMERICAL SIMULATION OF PARTICLE-LADEN FLOWS IN CURVED PIPES

By

Pusheng Zhang

A DISSERTATION

Submitted to
Michigan State University
in partial fulfillment of the requirements
for the degree of

DOCTOR OF PHILOSOPHY

Mechanical Engineering

2012

ABSTRACT

NUMERICAL SIMULATION OF PARTICLE-LADEN FLOWS IN CURVED PIPES

By

Pusheng Zhang

Particulate flows in curved pipes are commonplace in a variety of settings and involve aerosol deposition in airways as well as solids or droplets impacting pipe walls. The presence of bends in such flows is well-known to be associated with large pressure drops and phase separation due to the centrifugal force. The consideration of bends is thus important in designing multiphase flow equipment and pipes. For example, natural gas transported in pipes is often wet and water droplets, as they pass through the bend, may impact the bend wall where they form a film; this may well influence the performance of separation equipment located downstream. Phenomena associated with flows through curved pipes, such as the formation of secondary flow patterns, are thus studied in this work in order to evaluate their effects on the disperse phase. In addition, the accuracy of the numerical simulations for such flows is often in question when compared with experiments. This may be due to a number of factors which include the selection of an appropriate multiphase model and turbulence closure, or numerical aspects such as the quality of the treatment of the near wall behavior.

In the first part of this work, dilute particle flows in curved pipes are modeled using one-way and two-way coupled models. In one-way coupling simulations, the influence of the particles on the carrier phase is ignored. The influence of turbulence closures on the flow and particle trajectories are investigated. The "standard" k- ϵ model and the Reynolds Stress Model (RSM) based on the Reynolds-Averaged Navier-Stokes (RANS) equation are employed with different near-wall treatments. For two-way coupling simulations, the drift flux model based on the

mixture theory is used to consider the interaction between the phases. A realizable k- ϵ model is employed to close the RANS equation and the Enhance Wall Treatment (EWT) is applied for the flow in the near-wall region. Results show that the pressure drop of a single phase flow along the curved pipe is well predicted by the turbulent closures studied.

For one-way coupled simulations, RSM with EWT is accurate in estimating grade efficiency curves. Compared to other possible combinations, using RSM with EWT can improve the accuracy by as much as 19% in a 90° bend and up to 30% in a 180° bend. The results of these simulations have allowed the development of an improved correlation for predicting grade efficiency curves. For two-way coupled simulations, results show that the pressure drop is significantly affected by the disperse phase. The computed pressure has a good agreement with the empirical correlation of Paliwado. Bend design using the mixture model shows that 90° and 180° bends with the curvature ratios equal to 5 and 7 respectively can be used to achieve a high deposition efficiency with a relatively low pressure drop.

Following the above studies, a modification of the Immersed Boundary (IB) method, an approach for the simulation of particles moving in a fluid, is introduced to perform a preliminary validation of the closures used in multiphase flow modeling. An algorithm is implemented to combine the MacCormack scheme with the IB method. The technique is applied to particulate-laden flow simulations. This data is used to verify the performance of the mixture model on estimating particle behaviors in Couette flows and Poiseuille flows. Results show that IB method based on the MacCormack scheme is promising in dealing with fluid-structure interaction especially for particulate-laden flows. Comparison between the DNS data and the mixture model indicates that the mixture model is not able to capture particle migration. To improve the performance, the lift force needs to be considered in the model used to close the slip velocity.

Dedicate this work to my parents and my wife, Shaowen.

ACKNOWLEDGMENTS

I would like to give my deepest gratitude to my advisor, Dr. André Bénard for his invaluable guidance, understanding, and constant encouragement during the entire period of 4 years of the present research at MSU. His patience and support helped me overcome many difficulties and finish this dissertation.

I am deeply grateful to Dr. Charles Petty for his countless assistance and guidance to always keep my research on the right track. I am also thankful to him for the many valuable discussions that helped me understand my research area better.

I would like to gratefully and sincerely thank Dr. Randy Roberts for his insightful comments and constructive criticisms at different stages of my research.

I would like to acknowledge Dr. Farhad Jaberi for setting high standards in his teaching and helping his students to achieve those standards in the class.

I also want to thank Dr. Neil Wright's help for his serving my dissertation defense committee and reviewing the manuscript of my dissertation.

I want to thank all my instructors at MSU, who taught and encouraged me to reach this point. I want to thank department staffs for their secretarial support on my study and life at MSU.

I would like to thank my family for their generous support, and in particular, to express my deep appreciation to my wife, Shaowen, for her patience, assistance, continuous encouragement, and support.

Finally, I gratefully acknowledge the support for this work from the NSF-I/UCRC grant IIP-0934374 on Multiphase Transport Phenomena and the Chevron Energy Technology Company.

TABLE OF CONTENTS

LIST OF TABLES	ix
LIST OF FIGURES	X
1 INTRODUCTION	1
1.1 Background	1
1.2 Objectives of this work	4
1.3 Outlines of this dissertation	7
2 SIMULATION OF DILUTE PARTICULATE-LADEN TURBULENT F CURVED PIPES USING A EULERIAN-LAGRANGIAN METHOD	
2.1 Introduction	9
2.2 Modeling the Continuous Phase	11
2.2.1 Governing Equations	13
2.2.2 Near-wall Treatment	14
2.3 Modeling the Discrete Phase	14
2.3.1 Stochastic Turbulent Model	16
2.3.2 Empirical Models for Grade Efficiency	17
2.4 Numerical Approaches	19
2.5 Test Cases	20
2.6 Results and Discussions	26
2.6.1 Flow Patterns and Secondary Flow Intensity	26
2.6.2 Pressure Drop along Curved Pipes	30
2.6.3 Modeling Particle Deposition	35
2.7 Summary	48
3 SIMULATION OF DILUTE TURBULENT MIST FLOW IN CURVED	
USING AN EULERIAN-EULERIAN METHOD	
3.1 Introduction	
3.2 Multiphase flow modeling	
3.2.1 Multiphase turbulent flow modeling	
3.2.2 Turbulence closure	57

3.2.3 Near-wall treatment	57
3.3 Numerical methodologies	58
3.4 Geometry and meshing	58
3.5 Results and discussion	59
3.5.1 Model assessment	59
3.5.2 Applications	66
3.6 Summary	77
4 SIMULATION OF FLUID-STRUCTURE INTERACTION USING AN ELASTIC	C
FORCING METHOD BASED ON AN IMMERSED BOUNDARY METHOD	
4.1 Introduction	78
4.2 The MacCormack/IB method	82
4.2.1 Elastic forcing method	84
4.2.2 Construction of the Dirac delta function δ_h	87
4.3 Algorithm	90
4.4 Results and discussion	93
4.4.1 Poiseuille flow	93
4.4.2 Flow passing a stationary cylinder	98
4.4.3 Particle impinging on a wall	103
4.5 Summary	107
5 DIRECT NUMERICAL SIMULATION OF PARTICULATE-LADEN FLOW USING AN FICFICIOUS DOMAIN METHOD BASED ON THE IMMERSED	
BOUNDARY METHOD	109
5.1 The fictitious domain method	109
5.2 Collision scheme	111
5.3 Test cases	114
5.3.1 Flow passing a stationary cylinder	114
5.3.2 Particle sedimentation	115
5.3.3 Particle behavior	127
5.4 Validation of the mixture model in FLUENT	136
5.4.1 Transport of a non-uniform shear flow	137
5.4.2 Transport of a uniform unidirectional flow	141
5.5 Summary	144
CONTRACTOR CONTRACTOR AND DESCRIPTION OF THE PROPERTY OF THE P	
6 SUMMARY, CONCLUSIONS, AND RECOMMENDATIONS	146

6.1 Summary and Conclusions	146
6.2 Recommendations for future work	149
APPENDICES	152
A. Realizable k-ε equation for two-phase flows	
B. Analysis of force acting on a particle	
BIBLIOGRAPHYS	156

LIST OF TABLES

Table 2.1: Summary of the parameters used in the test case studies	20
Table 2.2: Boundary conditions used in all simulations	21
Table 2.3: Mesh grid nodes used for the solution independent study	24
Table 3.1: Boundary conditions used in all simulations	59
Table 3.2: Summary of the parameters used in the test cases	66
Table 3.3: Pressure drop and deposition efficiency in a U-bend with different incline angles7	73
Table 4.1: Differencing sequence for the space derivative discretization	92
Table 4.2: Mesh dependence study in space and time for flow with Re=100 10	03
Table 5.1: Comparison of results from the current schemes and other methods (Re=100) 1	15

LIST OF FIGURES

Figure 1.1: Flow chart shows the structure of this dissertation
Figure 2.1: Schematic display of 3D geometric parameters of a bend with a bend angle θ 22
Figure 2.2: O-type structured mesh used for a cross section; this mesh allow easy refinement close to the wall and prevents a singularity at the center of the pipe
Figure 2.3: Independent study of particle deposition using RSM with (a) SWF and (b) EWT
Figure 2.4: The streamlines show the development of flow patterns in a tight bend (δ =1.5); the secondary flows are also shown at different cross-sections
Figure 2.5: The streamlines associated with secondary flow patterns are studied at a 45°, 90° and 135° deflection and shown in (a), (b) and (c) by the stand k-ε model and in (d), (e) and (f) by the RSM.
Figure 2.6: Plots of the streamlines associated with the in–plane flow patterns at 135° in a U-bend with δ =5.6 to demonstrate the effect of an increasing flow Re number
Figure 2.7: A comparison between the computed (markers) and estimated (lines) pressure drop values by using different closure models combined with EWT
Figure 2.8: A comparison between the computed (markers) and estimated (lines) pressure coefficient (Cp) from near-wall treatments is made at the outer bend, inner bend, and the sides
Figure 2.9: A comparison between computed and experimental data for the grade efficiency shows a discrepancy occurs at small value of St for SWF and NEWF and great improvement by using EWT in: (a) the 90-degree bend, (b) the 180-degree bend
Figure 2.10: Comparison of the models (makers) and the empirical models (lines) shows that the k- ϵ model over-estimates particle deposition when particles experience a longer residence time in (b) the 180° bend (τ =4.4ms) than in (a) the 90° bend (τ =2.2ms)
Figure 2.11: Comparison of grade efficiency shows that the particle cutsize is 30% smaller in the 180 °bend due to the longer particle residence time
Figure 2.12: Comparison of bends with a varying curvature ratio for a fixed flow Reynolds number in a 90 ° bend shows the grade efficiency is increased with the increase of the curvature ratio.

Figure 2.13: Comparison of results for curved pipes with different curvature ratio and fixed particle residence time shows the grade efficiency is increase with the decrease of bend curvature ratio.
Figure 2.14: (a) Comparison shows that the models are not appropriate for varying δ in a 90° bend (b) Comparison shows the new model match the results relatively well for δ between 3 and 8 but has reduced accuracy at extreme curvature ratios
Figure 2.15: Comparison of grade efficiency shows a deviation of 9% when the Re number increases by a factor of 10
Figure 2.16: Comparison results show the particle cutsize is increased as the increase of the pipe dimension
Figure 2.17: Estimation of deposition patterns of particles changes with Stokes number 48
Figure 3.1: The air and water streamlines show the development of the flow patterns and the interaction between two phases. The contour of α_p shows the liquid film formation along the 180 °bend. "G" and "L" denotes gas and liquid, respective
Figure 3.2: Water film forms at the inner bend wall affected by the secondary flow pattern 63
Figure 3.3: Volume fraction distribution of the water phase shows the location of liquid film at the pipe wall of the outlet cross section
Figure 3.4: Comparison shows good agreement of the numerical results with the Paliwoda's empirical model
Figure 3.5: Comparison between the single-phase air flow (b) and the air-water flows (c-f) on the secondary flow patterns at the cross section of 90° deflection (a) changing with different droplet size
Figure 3.6: Volume fraction distribution shows the liquid film location at the cross section of 90 °deflection changing with different droplet size
Figure 3.7: Secondary flow patterns and flow intensity at the cross section of 90 $^{\circ}$ deflection for flow with a different α_p
Figure 3.8: Pressure drop of the bend section changing with (a) the droplet size, (b) volume fraction of the water phase
Figure 3.9: Droplet deposition efficiency changing with (a) the droplet size, (b) volume fraction of the water phase

Figure 3.10: Schematic of a U-bend changing from horizontal position to vertical position with an increment of 15°. For interpretation of the references to color in this and all other figures, the reader is referred to the electronic version of this dissertation
Figure 3.11: Tendency of bend pressure drop and droplet deposition efficiency in a horizontal 90 °bend and a 180 °bend shows the bend geometry is optimal at curvature ratio equal to 5 and 7, respectively
Figure 4.1: Schematic configuration shows a Eulerian mesh for the fluid domain Ω_f and a Lagrangian mesh around the fluid-object interface ∂S
Figure 4.2: Schematic of spring construction for a movable rigid structure using a Lagrangian forcing method
Figure 4.3: Schematic configuration shows two mesh systems and the Eulerian points involved in a spreading procedure and an interpolation procedure for one Lagrangian point 89
Figure 4.4: Distribution of $\phi(r)$ shows how the Dirac delta function works
Figure 4.5: Schematic of a flow passing two parallel planes (a) without an immersed cylinder and (b) with an immersed cylinder
Figure 4.6: Comparison of the velocity profiles between the analytical solution and the numerical results cross the channel shows a very good agreement
Figure 4.7: Comparison of the vector and the vorticity between (a) a Poiseuille flow (b) a Poiseuille flow interacted with a stationary structure
Figure 4.8: Comparison of the velocity profiles along Line AB between two cases
Figure 4.9: Comparison of the pressure distribution along Line CD between two cases
Figure 4.10: Schematic of the computational domain used for flow passing a stationary cylinder
Figure 4.11: The developing vorticity patterns with a changing time shows the flow eventually breaks into a periodic K árm án Vortex Street
Figure 4.12: Schematic of computational domain for a disc settling under gravity and a stationary wall
Figure 4.13: The vertical velocity and center location of the disc changing with time shows the settling disc is (1) accelerated, (2) with constant velocity, (3) decelerated, and (4) at rest.

Figure 4.14: Schematic of velocity contour shows a disc is settling under gravity and impinging on a stationary wall
Figure 5.1: Schematic of the collision scheme used to prevent collision between (a) two particles (b) a particle and a stationary wall
Figure 5.2: A curve shows the repulsive force acting on a rigid particle is decreased dramatically as the increase of particle distance within the safety zone and is zero out of the safety zone
Figure 5.3: Comparison of (a) disc position and (b) disc velocity between the elastic forcing method and the fictitious domain method shows that the fictitious domain method (short dash) outperforms the elastic forcing method (solid line) in estimating the terminal velocity of a disc falling in a flow with Re=100
Figure 5.4: Comparison of (a) disc position and (b) disc velocity between the elastic forcing method and the fictitious domain method shows that both methods are numerically symmetric in estimating the terminal velocity of a disc falling in a flow with small Reynolds number (Re=10 for the fictitious domain method).
Figure 5.5: Schematic demonstration of two particles (a) drafting, (b) kissing, (c) tumbling and (d) being apart after tumbling
Figure 5.6: Schematic demonstration of 240 particles doing sedimentation under gravity in a sealed container at (a) t=0s, (b) t=2.5s, (c) t=5s, (d) t=7s, and (e) t=20s
Figure 5.7: Schematic of computational domain for a neutrally buoyant elliptical disc moving in a Stokes shear flow
Figure 5.8: Comparison of results from the DNS method for different Re_p and Jeffery's solution shows that the angular velocity and the period are well predicted by the present DNS scheme for Re_p =0.4.
Figure 5.9: Schematic of the computational domain dimension $[L_1 \ L_2]$ and the initial location of an elliptical disc located at $(1/4L_1, 1/5L_2)$ in a Couette flow with Re=700
Figure 5.10: Comparison of the particle location changing with time in the vertical direction shows that particles attain the centerline in a Couette flow regardless of the size and shape of a particle
Figure 5.11: Schematic of the computational domain dimension $[L_1 \ L_2]$ and the initial location of an elliptical disc located at $(1/4L_1, 7/16L_2)$ in a Poiseuille flow with Re=700 133

Figure 5.12: Comparison of the particle location changing with time in the vertical direction shows that particles attain approximately the location 60% from the centerline to the wall in a Poiseuille flow regardless of the size and shape of a particle
Figure 5.13: Schematic demonstration of the velocity contour and the concentration distribution of a uniform particulate-laden flow with α_p =10% in a Couette flow at t=0s, 5.5s, 100s, 125s, 135s and 160s.
Figure 5.14: Schematic demonstration of the velocity contour and the concentration distribution of a uniform particulate-laden flow with α_p =10% in a Poiseuille flow at t=0s, 1s, 30s, 60s, 100s and 416.0 s
Figure 5.15: Initial condition shows the concentration of the dispersed phase in the computational domain for (a) the present scheme (b) the mixture model
Figure 5.16: Comparison of the concentration of the dispersed phase at t=10s for (a) the present scheme (b) the mixture model
Figure 5.17: Comparison of the concentration of the dispersed phase at t=25s for (a) the present scheme (b) the mixture model
Figure 5.18: Comparison of the concentration of the dispersed phase at t=60s for (a) the present scheme (b) the mixture model
Figure 5.19: Schematic of the computational domain for a uniform flow with $\alpha_p=10\%143$
Figure 5.20: Comparison of volume fraction distribution along a vertical cross-section between two methods at t=50s and t=100s shows that the mixture model fails to predict a higher concentration near the center for a uniform particulate-laden shear flow
Figure 5.21: Comparison of volume fraction distribution along a vertical cross-section between two methods at t=20s and t=40s shows that the mixture model fails to predict a higher concentration close to the wall for a uniform particulate-laden pressure-driven flow (Re=700).

CHAPTER 1

INTRODUCTION

1.1 Background

A particulate-laden flow is a two-phase flow in which one phase is continuously connected called carrier phase and the other phase composes of discrete immiscible particles. Particulate-laden flows in curved channels are commonplace in nature and often seen in a variety of setting associated with biological, chemical, nuclear, pharmaceutical and food industries. They involve phenomena as varied as aerosol deposition in airways or pollution control systems, as well as solids or droplets impacting pipeline walls. Flows in most industrial applications are turbulent. Therefore understanding of the behavior of particle turbulent flows in curved pipes is of tremendous importance to help industries in cost saving and productivity increase.

Compared to single-phase flows, particulate-laden flows are significantly more complex. New parameters are introduced due to the presence of particles such as the particle volume fraction α_p , mass loading φ , Stokes numbers St, and particle Reynolds number Re_p. The discrete phase can impact the pressure drop and the turbulent intensity of the carrier phase in a significant way. In general, the pressure drop of a particulate-laden flow is increased with the increase of the particle volume fraction (Hoang & Davis 1984). However, Marcus et al. (1990) observed that in some cases involving a small mass loading (φ <4) and transport of fine particles (in an order of 10^{-5} m), the increasing α_p can actually decrease the pressure drop due to a reduction in the gas-phase stress. The particle diameter d_p , volume fraction α_p , and Reynolds number Re_p have been shown to be responsible for turbulent intensity modulation. Theofanous & Sullivan (1982) showed

theoretically that the turbulence intensity is a function of the particle volume fraction. Gore & Growe (1989) provided a critical parameter $d_p/\Lambda \approx 0.1$, where Λ is the fluid integral length scale, to predict turbulence attenuation and augment. Turbulence intensity is suppressed for $d_p/\Lambda < 0.1$ and enhanced for $d_p/\Lambda > 0.1$. Hetsroni (1989) stated that particles with Re $_p$ larger than 400 would enhance the turbulence due to particle vortex shedding.

The Stokes number provides a measure of response time of the particles to the flow and is defined as $St \equiv \tau_p / \tau_f$ where τ_p is the particle relaxation time and τ_f is the fluid characteristic time scale. Particles with a small Stokes number ($St \ll 1$) would follow the carrier flow closely and particles with a large St (St > 1) would go across the flow streamlines. Starkey (1956) experimentally observed the non-uniform distribution of particles in pipe flows and demonstrated that neutrally buoyant spherical particles under certain conditions have lateral migration in a Poiseuille flow. Particle behavior such as particle clustering is not fully understood to date.

To study particulate-laden flows, it is helpful to classify the flows into two distinct categories: dilute flows and dense flows. Elghobashi (1991) used the mean distance S between the centers of two neighboring particles to define a suspension flow. He stated that the flow is considered to be dilute if $S > 10d_p$ and dense if $S < 10d_p$. Crowe et al. (1998) defines a particulate-laden flow based on the forces dominated to control the particle motion. A flow is dilute if the particle motion is determined by hydrodynamic forces, such as drag and lift and is dense if controlled by particle collision. A simple classification of dilute and dense flows is based on the volume fraction of the dispersed phase α_p . For industrial processes, flows are considered dilute if $\alpha_p < 10\%$. Depending on the mass loading (or mass fraction) used for the dispersed phase, dilute

flows can be further classified into one-way coupling and two-way coupling. If the particle mass fraction is small, it is reasonable to neglect the influence of the dynamics of the dispersed phase on the carrier phase called one-way coupling. However, a dilute flow has to be considered two-way coupling if the mass fraction is so large that the influence of the dispersed phase on the carrier phase cannot be neglected.

Recent advances on computational fluid dynamics (CFD) software and computer simulations provide an efficient approach for studying dilute flows. Models describing particulate-laden flow by convention can be divided into two groups: Eulerian-Lagrangian methods (Maxey and Riley 1983) and Eulerian-Eulerian methods (Manninen et al. 1996). Although all of the approaches treat the carrier phase as a continuum, the particle phase is treated differently in these two groups. In the Eulerian-Lagrangian approaches, the particles are marked as discrete objects in the fluid flow. The motion of each particle is computed through a force balance equation. The Eulerian-Lagrangian methods seem quite efficient in dealing with flows of one-way coupling. However, the methods are shown to be computationally expensive when a large number of particles are involved and their impact on the carrier phase becomes significant due to a high mass loading. A more sophisticated way of dealing with two-way coupling in industrial applications is to employ a Eulerian-Eulerian method or a two-fluid model which treats both phases as continua. The interaction between the phases is considered in a momentum term which requires to be closed by models.

An alternative approach of studying particulate-laden flow is direct numerical simulation (DNS). To tackle the interaction between the phases, the no-slip boundary condition has to be imposed on the surface of the moving particles. A popular approach in dealing with such problems is to enforce the no-slip boundary condition directly on the structure surface which

requires an adaptive mesh to be built on the particle interface and extended to the fluid domain (called body-conformal mesh). However, building a body-conformal mesh is cumbersome even for a simple geometry like particles. This can be overcome by using a non-body conformal Cartesian grid. Because the structure surface does not line up with the Cartesian grid, modification to the fluid equation is required in the vicinity of the boundary. Clarke et al. (1986) proposed a cut-cell approach which imposes the boundary conditions through a cut-cell procedure. Majumdar et al. (2001) introduced a ghost-cell method where the boundary conditions are imposed by fixing suitable values of the solution on the ghost cells outside the computational domain. The most efficient and flexible method in this category is called the immersed boundary (IB) method which considers impact of the immersed structure in the force density term of the fluid equation. The IB method is therefore employed in this dissertation for DNS of particulate-laden flow. Although solving a turbulent flow using DNS is still challenging nowadays due to the limited computational power, DNS data for flows with a moderate Reynolds number can be used as experimental data to validate multiphase flow models.

1.2 Objectives of this work

Dilute particulate-laden flow systems constitute one of the most widely used conveying systems in industrial applications. This dissertation considers dilute flows conveying in curved pipes. A Eulerian-Lagrangian particle tracking method and a Eulerian-Eulerian method in the commercial software ANSYS FLUENT are employed to model one-way coupling and two-way coupling dilute flows, respectively. Direct numerical simulations of dilute suspension flows in 2-D Couette and Poiseuille flows are conducted using an immersed boundary method for model validation.

The objectives of this work are:

(1) Provide computational guidelines for modeling pressure drop and particle deposition of one-way coupling dilute gas/solid flow in the turbulent regime in curved pipes and develop an empirical model for estimating particle grade efficiency including the impacts of particle Stokes number, bend angle and curvature ratio.

The accuracy of using the Discrete Phase Model (DPM) (a Eulerian-Lagrangian method) in FLUENT in predicting particle deposition of one-way coupling dilute turbulent flows in curved pipes is often in question when compared with experiments. This may be due to a number of factors which include the selection of an appropriate multiphase model and turbulence closure or numerical aspects such as the quality of the treatment of the near wall behavior. The accuracy of different closure models and the performance of using different near-wall treatments are thus studied in order to evaluate their effects on the pressure drop and the deposition efficiency of a particulate flow.

(2) Systematically study and discuss the feasibility of using a drift flux model based on the mixture theory (a Eulerian-Eulerian method) in estimating pressure drop and liquid film of two-way coupling dilute gas/liquid (mist) flows in the turbulent regime in curved pipes.

Design a curved pipe can promote film formation without causing a large pressure drop.

This work is motivated by the possibility of using computational fluid dynamics (CFD) as a design tool applied to curved pipes feeding a gas/liquid separator. The question is to identify the curvature of such pipes that can promote film formation upstream of the separator and thus pre-condition the flow without creating a large pressure drop. As regards to liquid film modeling, two-way coupling needs to be considered for a particulate-laden flow. The one-way coupling DPM is shown accurate in estimating

particle deposition in Chapter 2. However, this method is not efficient and only suitable to predict a very thin film with the thickness limited to 500 µm (ANSYS FLUENT 12.1, 2009). The mixture theory with a new drift flux model in FLUENT is considered to be an efficient version of the Eulerian-Eulerian method in dealing with two-way coupling particulate-laden flows. However, there is a lack of literature on the application of the drift flux model in estimating pressure drop and liquid film formation in curved pipes.

(3) Developed an algorithm to combine the immersed boundary methods with the explicit MacCormack solver for direct numerical simulation of particulate-laden flow. DNS data is used to validate the performance of the mixture model in FLUENT on estimating the particle behavior of suspension flows.

Particle migrating cross streamline in a unidirectional flow, i.e. Couette flow and Poiseuille flow, is caused due to the lateral force induced by fluid inertia (Ho and Leal 1973). This phenomenon is known to be responsible for non-uniform concentration distribution of particles in pipe flow. The mixture model in FLUENT has been broadly used in industrial applications, such as sedimentation, cyclone separators and, particle-laden flows. To accurately predict the particle concentration distribution, the model must possess the capability of capturing the phenomenon of inertia-induced cross-stream migration of small suspended particles. Nevertheless, study on the performance of the mixture model on estimating particle migration cannot be found in literature.

1.3 Outlines of this dissertation

The structure of this work is shown in the flow chart in Fig 1.1. Chapter 2 of this dissertation investigates the performance of various Reynolds-Averaged Navier-Stokes (RANS) models and near-wall treatments with the discrete phase model on modeling one-way coupling dilute particulate-laden flows particle deposition in curved pipes. The study focus on the flow patterns, secondary flow intensity, pressure drop, and particle deposition. An empirical model is developed to estimate the grade efficiency of particle depositing on the curved pipe wall according to the particle Stokes number, the bend angel and curvature ratio. In Chapter 3, twoway coupling dilute mist flows in curved pipes are simulated using a Eulerian-Eulerian technique referred to as a drift flux model based on the mixture theory. Bend design related the pressure drop and liquid film formation is conducted. Chapter 4 of this work introduces an immersed boundary method based on the elastic forcing method to tackle fluid-structure interaction. An algorithm is developed to combine the MacCormack scheme with the immersed boundary method for DNS of particulate-laden flow simulation. In Chapter 5, a direct forcing method proposed by Uhlmann (2005) is used to improve the stability and the accuracy of the immersed boundary method. The results are used to validate the performance of the mixture model in FLUENT on estimating particle migration in a Couette flow and a Poiseuille flow.

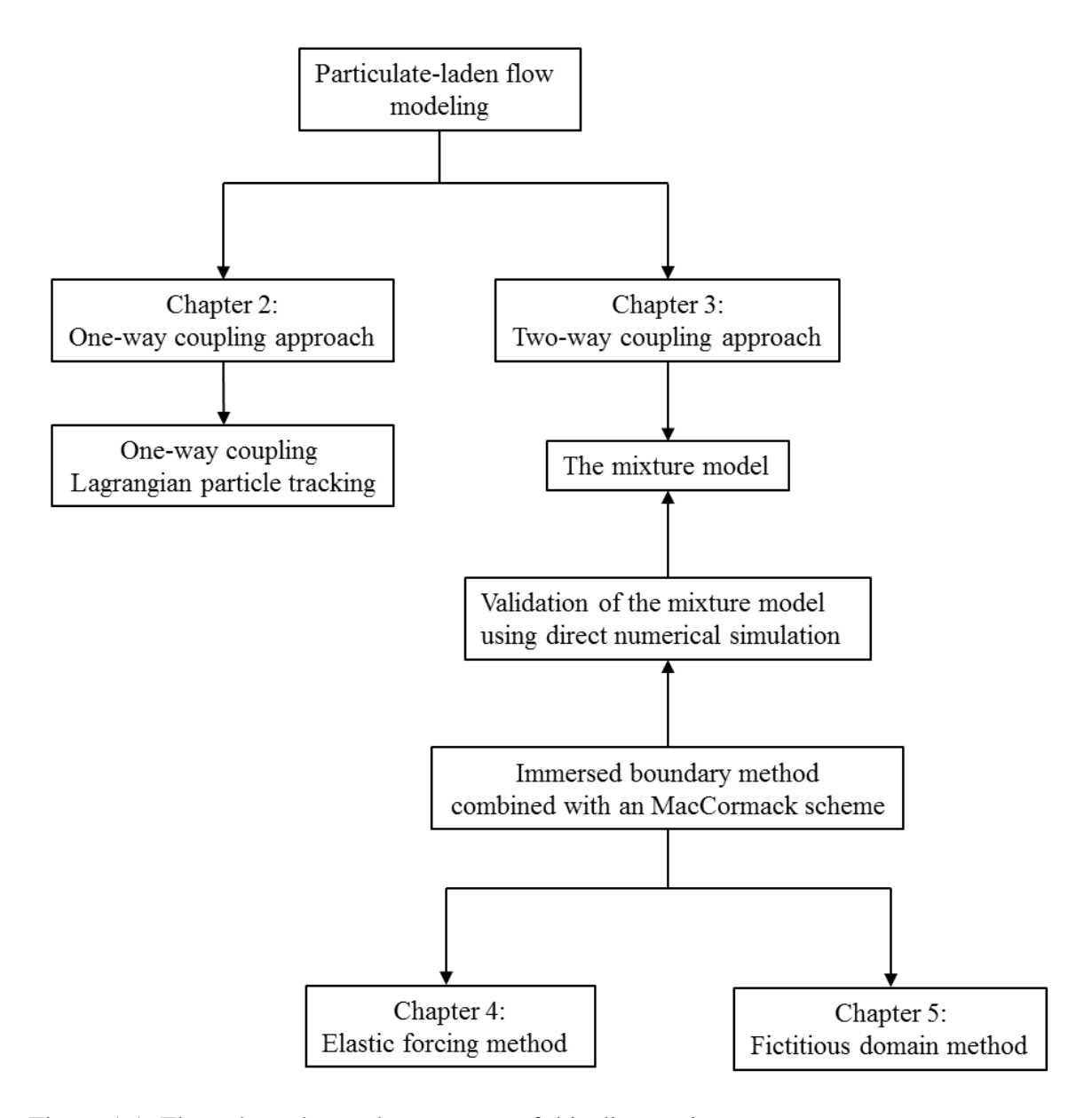


Figure 1.1: Flow chart shows the structure of this dissertation.

CHAPTER 2

SIMULATION OF DILUTE PARTICULATE-LADEN TURBULENT FLOWS IN CURVED PIPES USING A EULERIAN-LAGRANGIAN METHOD

2.1 Introduction

Curved pipes form essential components of piping systems of the oil and gas industry. The presence of bends is well-known to be associated with complex flow patterns as well as large pressure drops and to affect the performance of downstream equipment. This is especially important for multiphase flows as the significant pressure gradient and secondary flow around the bends would affect the phase distribution. A variety of phenomena associated with flows through curved pipes, such as the formation of secondary flow patterns, are thus studied in this work in order to evaluate their effects on the disperse phase.

Much work has been done on studying pressure drop, flow patterns, and particle deposition in curved pipes. Thomson (1876) first observed the curvature effects of bends on flows. Eustice (1910) also observed the existence of secondary flows by injecting ink into water passing through a coiled pipe. Wilson et al. (1922) observed that the pressure drop is dependent on the flow Reynolds number and Dean (1928) studied theoretically curved pipe flows and identified the condition for the onset of secondary vortices. Ito (1959) found that secondary flows can cause a rapid rise in friction and lead to a much increased pressure drop. Tunstall and Harvey (1968) observed the presence of a main (or primary) flow recirculation at the inner wall for tight bends ($\delta < 3$). The literature on flow through curved pipes is vast and Berger et al. (1983) provided a comprehensive review of this subject. The intensity of secondary flows in bends depends on the combination of the main flow Reynolds number (Re=Ud/v) and the curvature ratio (δ =R_b/R_t). It can be characterized by a dimensionless number called the Dean number

which is defined here as De=Re/ $\delta^{1/2}$. Ito (1987) demonstrated that the size of the secondary flow patterns matches the size of the duct radius.

Based on theoretical calculations, Cheng and Wang (1975) derived a formula to estimate particle deposition in bends but it does not account for secondary flow patterns. The empirical model is accurate for Reynolds numbers in the range of 1000<Re<5000. Pui et al. (1987) observed that complex flow patterns as well as turbulent fluctuations play a major role in particle deposition patterns. They proposed an empirical model for the particle deposition efficiency for turbulent flows in a 90 ° bend that is a function of only the Stokes number (St). Peters and Leith (2003) measured the deposition efficiency of high Re number flows in large industrial curved pipes with different bend angles. Brockman (1993) extended the empirical model of Pui et al. (1987) by accounting for the bend angle in addition to the Stokes number. McFarland et al. (1997), using numerical results, developed an empirical model that accounts for the bend angle, the Stokes number, and the bend curvature ratio to estimate the deposition efficiency. In spite of the vast amount of work performed, there is still a need to identify conditions under which computer simulations can provide relatively accurate results.

Computer simulations provide an efficient approach for studying flows through curved pipes under various conditions. Practical simulations can be performed by solving the filtered Navier-Stokes equation using a Large-Eddy Simulation (LES) for an instantaneous solution or by solving the Reynolds Average Navier-Stokes (RANS) equation for an ensemble averaged solution (with appropriate closure models for the Reynolds stress or the sub-grid stress tensors). For example, Breuer et al. (2006) and Berrouk et al. (2008) used LES to study particle deposition and their computed results are in good agreement with the work of Pui et al. (1987) except for small Stokes number St<0.2. A RANS approach was selected for this work because of the large

number of simulations expected. In addition, a Reynolds stress model was selected to complete the formulation of the RANS equation due to the anticipated presence of strong streamline curvatures.

In this Chapter, the performance of RANS models with different near wall treatments is evaluated on estimating pressure drop and deposition efficiency of a dilute turbulent suspension flow through curved pipes. The quality of the results is assessed in various ways. A comparison of the flow patterns at different pipe cross sections is made between the standard k-ε and Reynolds stress models. The intensity distribution of secondary flows is investigated at different cross sections of the U-bend with a fixed curvature ratio. Numerical calculations from different near-wall treatments based on the standard k-ε model and RSM of the pressure drop are compared to the experimental work of Sudo et al. (1998 and 2000). The performance of the k-ε model and RSM, in combination with different near-wall treatments in estimating particle deposition, is also examined, along with the effect of turbulent fluctuations on particle deposition. Grade efficiency curves are compared to the experimental work of Pui et al. (1987), Brockmann (1993) and McFarland et al. (1997). In addition, the effects of particle residence time, bend curvature ratio, and flow Reynolds number on the grade efficiency are investigated.

2.2 Modeling the Continuous Phase

A dilute particle-laden flow with a low mass loading is considered in this Chapter. For this kind of flows, the impact of the particles on the carrier fluid is ignorable (one-way coupling) and no particle-particle interaction is involved. Particles move with the local gas velocity, but no momentum and mass of the particles are transferred to their surrounding gas flow. Under this assumption, the single-phase gas flow and the particle trajectories can be solved independently.

The continuous phase is solved using a Eulerian approach. The Reynolds-Averaged Navier-Stokes (RANS) equation governs the transport of all mean-flow properties of turbulent flows with the range of all scales being modeled. This allows computing costs to be reduced provided that an accurate closure model is used. The commercial software ANSYS FLUENT 12.1 was used for the simulations presented below. The software provides several models for closing the RANS equation and these include models based on eddy-viscosity closure approaches such as the "standard" k-ε and k-ω models. Various formulations of the Reynolds Stress Model (RSM) are also available; these involve solving transport equations for approximating the Reynolds stress and an equation for the dissipation rate. To estimate the grade efficiency, Matida et al. (2004) used the Spalart-Allmaras model and the k-ω model in a mouth-throat geometry and found that the grade efficiency curves computed from those models are highly overestimated for the entire range of particle diameters. The discrepancy from the results of Pui et al. (1987) reaches the order of 15%-25%. Furthermore, the agreement to the experiment of the standard k-ε model is observed to be worse than that of the k-ω model. To avoid using the Boussinesq approximation (or eddy-viscosity models), McFarland et al. (1997) employed the RSM and calculated the turbulent fluctuations using one-step correction approach of Abuzeid et al. (1991). However, deviations from the results of Pui et al. (1987) were still as high as 17% at Stokes number St=0.2. Although much work has been done using different closure models, the effect of the near-wall treatments on pressure drop along curved pipes and particle deposition on the pipe wall is rarely discussed. An accurate representation of the flow in the near-wall region is needed to model particle deposition as turbulent fluctuations strongly affect particle trajectories at the near-wall region. ANSYS FLUENT 12.1 allows to use the standard wall function (SWF), the non-equilibrium wall function (NEWF) or the enhanced wall treatment (EWT) as the near-wall

treatments (ANSYS FLUENT 12.1, 2009). Zhang et al. (2012) used the RSM and the EWT for near-wall treatment. Results are compared to the work of Pui et al. (1987) and show that the EWT based on the RSM closure is promising in predicting particle deposition in a 90° bend. An error of only about 3% is observed at small Stokes number.

2.2.1 Governing Equations

Since the flow is one-way coupling, a transient solution to the continuous flow field is not necessary and the flow can be solved in a steady state. The governing equations for the continuous phase include the averaged continuity equation

$$\frac{\partial \mathbf{U_i}}{\partial \mathbf{x_i}} = 0 \tag{2.1}$$

and the RANS equation

$$u_{j} \frac{\partial U_{i}}{\partial x_{j}} = g_{i} - \frac{1}{\rho} \frac{\partial P}{\partial x_{i}} + \frac{\partial}{\partial x_{j}} \left(2\nu S_{ji} - \overline{u'_{j}u'_{i}} \right)$$
(2.2)

where S_{ji} is the mean rate-of-strain tensor, p is the mean pressure, **U** represents the average velocity (or mean velocity) profile, \mathbf{u}' is the fluctuating velocity, ρ is the continuous phase density, ν denotes kinematic viscosity, and g is the gravity. A model for $\overline{u_i'u_j'}$ is needed to close Eq. (2.2).

The standard k-ε model and the Reynolds stress model are used in this study and are not presented here for the sake of brevity. The standard k-ε model, based on an eddy-viscosity closure, is still commonly used and requires a transport equation for the kinetic energy k and for the dissipation rate ε (Launder and Sharma, 1972). The RSM is more complicated as it requires

the solution of six transport equations for individual Reynolds stresses plus one equation for the dissipation rate (Launder et al., 1975; Gibson and Launder, 1978).

2.2.2 Near-wall Treatment

In wall bounded flows, modeling the near-wall region is problematic as the closure models are valid only for the core flow. The quality of the approximated near-wall region significantly impacts the numerical solutions for the whole domain as it is a major source of vortices and turbulence. In dealing with wall-bounded flows, a common approach for modeling the near-wall region flow is to use semi-empirical wall functions. The standard wall function (SWF) and the non-equilibrium wall function (NEWF) are used in this work. The SWF is a semi-empirical formula proposed by Launder and Spalding (1974) based on the assumption that the production of kinetic energy and its dissipation rate in the wall-adjacent cell are equal. Kim and Choudhury (1995) provided a correction to the SWF which resulted in a two-layer-based NEWF. An alternative method of dealing with near-wall region is to capture the flow in that region by solving the one-equation model of Wolfshtein (1969); such an approach is called the enhanced wall treatment (EWT). The EWT is especially recommended for flow exhibiting strong streamline curvatures, boundary separation, or reattachment. However, extremely fine meshes near the wall are needed which leads to more demanding computations.

2.3 Modeling the Discrete Phase

The one-way coupling Discrete Phase Model (DPM), or Lagrangian particle tracking method, proposed by Maxey and Riley (1983) is used to track particles moving in the continuous phase through the curved pipes. In this method, fictitious particles are released in the continuous phase

and treated as a discrete phase. The concentration of particles is assumed to be dilute i.e. the particles do not interact and they have no effects on the continuous phase. The trajectory for a particle is obtained by integrating the force balance, i.e.

$$\frac{du_{p,i}}{dt} = F_D(u_i - u_{p,i}) + \frac{g_i(\rho_p - \rho)}{\rho_p} + F_s$$
 (2.3)

and

$$\frac{\mathrm{dx}_{\mathrm{p,i}}}{\mathrm{dt}} = \mathrm{u}_{\mathrm{p,i}} \tag{2.4}$$

and where

$$F_{\rm D} = \frac{1}{\tau_{\rm p}} \frac{C_{\rm D} \, \text{Re}_{\rm p}}{24} \tag{2.5}$$

In the above equations, u, u_p are the instantaneous gas and particle velocities; $x_{p,i}$ is the position vector of particle i; d_p is the particle diameter; ρ_p is the particle density; τ_p is the particle relaxation time obtained from $\tau_p = \rho_p d_p^2/18\,\mu$; Re $_p$ is the relative Reynolds number from $Re_p = \rho d_p |u_{p,i} - u_i|/\mu$; C_D is the particle drag coefficient (particles are assumed to be spherical and the spherical drag law is used to compute C_D (Morsi and Alexander, 1972)); F_s is an additional acceleration term that could be important under certain circumstance (e.g., severe pressure gradient, or great density difference).

Equation (2.3) and (2.4) are solved using a Runge-Kutta scheme. The maximum number of time step is set to 100,000 in all cases for this work, which is sufficient to ensure that all the particles either ended on the wall or at the pipe exit (there were no particles not accounted for in the simulations). The discretized time step Δt is obtained from $\Delta t = \Delta t^* / \lambda$ where λ is the step

length factor equal to the maximum number of time step divided by number of cross-sections along the main-flow direction; Δt^* is the transit time required for a particle to travel through the current mesh cell. This value is estimated according to the current particle velocity and the mesh size in the main flow direction following guidelines in ANSYS FLUENT 12.1 Documentation (2009).

2.3.1 Stochastic Turbulent Model

The effects of turbulent fluctuations on the particle deposition are modeled by using a discrete random walk model (DRWM), also called the stochastic turbulent model (Jang and Acharya, 1988). The instantaneous gas velocity u_i in Eq. (2.3) is a combination of the mean gas velocity u_i and fluctuating components u_i ? If turbulent fluctuations are not considered, trajectories are computed by substituting the instant gas velocity with the mean gas velocity obtained from the continuous phase calculation. To include the turbulent influence, the fluctuating components are approximated using an ad-hoc random distribution given by:

$$\mathbf{u}' = \zeta_1 \sqrt{\overline{\mathbf{u}'\mathbf{u}'}}; \ \mathbf{v}' = \zeta_2 \sqrt{\overline{\mathbf{v}'\mathbf{v}'}}; \ \mathbf{w}' = \zeta_3 \sqrt{\overline{\mathbf{w}'\mathbf{w}'}}$$
 (2.6)

where ζ_1 , ζ_2 and ζ_3 are normally distributed random numbers with zero mean and a unit standard deviation. The r.m.s. of fluctuation in Eq. (2.6) is not obtained from the transportation equations for the Reynolds stresses but is assumed isotropic and equal to $\sqrt{2k/3}$ so that the above approximation can be used.

The fluctuating components are discrete piecewise parameters that are function of time. Their random value is kept constant over an interval of time τ_e estimated by the lifetime of the eddy defined as

$$\tau_{\rm e} = -0.3 \frac{\rm k}{\rm \epsilon} \log(\rm r) \tag{2.7}$$

where r is a uniform random number between 0 and 1. When this time is reached, a new value of the instantaneous velocity is obtained by applying a new value of ζ . The performance of the stochastic model on particle deposition is studied later in this work.

2.3.2 Empirical Models for Grade Efficiency

Grade efficiency curves can be obtained from the results of particle tracking simulations in order to evaluate the performance of a device in separating particles. The grade efficiency is defined as

$$\eta(St) = \frac{M_c}{M} = \frac{N_c}{N}$$
 (2.8)

where M_c is the mass of particles separated from the total particle mass M released. Since monodisperse particles having the same density are tracked, M_c and M are replaced respectively by N_c which is the number of particles trapped in the bend plus the straight pipe after the bend and by the total number of particles tracked N. The grade efficiency, or deposition efficiency, is presented in this paper as a function of the Stokes number St. The Stokes number provides a measure of response time of the particles to the flow and is defined as the ratio of the particle relaxation time τ_p and the fluid characteristic time scale the system response time τ_f . It is defined

as

$$St = \frac{\tau_p}{\tau_f} = \frac{C\rho_p d_p^2 / 18\mu}{(d/2) / U_0} = \frac{C\rho_p d_p^2 U_0}{18\mu d/2}$$
(2.9)

where C is the Cunningham correction factor (Cunningham,1910) used to consider noncontinuum effects when computing the drag on small particles, U_0 is the mean flow velocity [m/s] and ρ_P denotes the particle density. For given values of U_0 , d, ρ_p and μ , the particle size is then proportional to $St^{1/2}$.

The computed grade efficiency curves are compared to empirical models. Pui et al. (1987) conducted experiments for particulate flows passing through a 90 ° bend with an 8.51mm diameter. Based on the experiments, they provided an empirical model used to estimate the grade efficiency in 90-degree bends, given as

$$\eta = (1 - 10^{-0.963St}) \times 100\% \tag{2.10}$$

Brockmann (1993) extended Pui et al.'s work to include the effect of bend angles. The expression of the model is

$$\eta = \left(1 - e^{-1.412St\theta}\right) \times 100\% \tag{2.11}$$

where θ is bend angle in radians. Both empirical models are stated with a 3% uncertainty. Later, McFarland et al. (1997) developed a model based on their numerical results to account for the effect of the St number, the bend angle and the bend curvature ratio. The model is given as

$$\eta = 100\% - \exp\left(\frac{4.61 + a\theta St}{1 + b\theta St + c\theta St^2 + d\theta^2 St}\right)$$
 (2.12)

where
$$a = -0.9526 - 0.05686\delta$$
, $b = \frac{-0.297 - 0.0174\delta}{1 - 0.07\delta + 0.0171\delta^2}$,

$$c = -0.306 + \frac{1.895}{\delta^{0.5}} - \frac{2}{\delta}, \quad d = \frac{0.131 - 0.0132\delta + 0.000383\delta^2}{1 - 0.129\delta + 0.0136\delta^2}$$

In this work, particles mimicking droplets are released at an upstream position of 3d prior to the entrance of the bend (z = 0). At this location, the flow can be treated as fully developed and the bend effect on particles can be neglected. 25,000 monodisperse spherical droplets are released at the mean flow velocity U_0 with the density 895 kg/m³. The density used here is consistent with that used in Pui et al.'s experiment. The particles are released at 3D upstream from the bend inlet and injected normal to the cross section in a square region (the sides of the square is 0.5d). This location keeps the particle away from the wall. Meanwhile, it avoids the influence of the bend and allows the particle to well mix with the continuous phase before the flow enters a bend.

2.4 Numerical Approaches

The governing equations for the continuous phase are solved assuming an adiabatic, steady flow in FLUENT using the pressure-based segregated algorithm, Semi-Implicit Method for Pressure-Linked Equations (SIMPLE) put forward by Patankar and Spalding (1972). The transport equations for k, ϵ and the Reynolds stress equations (for the RSM) are spatially discretized using a second-order upwind scheme. This is combined with a correction equation derived from the continuity equation and the momentum equation for pressure is discretized using the PRESTO! scheme (PRESsure STaggering Option) (ANSYS FLUENT 12.1, 2009) which is well-suited for flows with strong streamline curvatures. The stability of the numerical computations is improved by reducing the under-relaxation factor to 0.2 for the pressure and 0.5 for the momentum. The residual criterion for convergence (the "monitor") is set to 10^{-5} for all variables. Two monitors for the difference of the mass flow rate between the inlet and the outlet of a pipe and the area-average weighted pressure at the bend exit are used to ensure a converged

solution. Finally, to solve Eq. (2.3) for the discrete phase, a 5th order Runge-Kutta scheme is used (Cash and Karp, 1990).

2.5 Test Cases

The parameters used in three test studies are summarized in Table 2.1. The geometric configuration and the Reynolds number are selected based on the experimental setups available for comparison. A tight bend with a curvature ratio δ =1.5 and a larger bend with δ =5.6 are used to study the curvature effect on the flow patterns. In addition, the effect of the flow Re number on the flow patterns is investigated by changing the flow velocities. The local pressure is estimated numerically from different near-wall treatments based on the standard k- ϵ model and RSM in a 90 °bend and a 180 °bend and compared to the experimental work of Sudo et al. (1998 & 2000). The performance of the near-wall treatments in estimating particle deposition is evaluated by comparing the grade efficiency to the empirical work from the literature. Varying the bend curvature ratio and flow residence time is achieved by changing the bend radius and bend angles. Finally, the effect of the pipe dimension on the particle deposition is studied by increasing the pipe diameter from d=8.51mm to d=100mm while maintaining the Re number, the curvature ratio and the bend angle.

Table 2.1: Summary of the parameters used in the test case studies

	Qualitative Study	Study on Pressure	Study on Particle
	on Flow Patterns	Drop	Deposition
Diameter, d [mm]	8.51	104	8.51
Curvature Ratio, δ	1.5,5.6	4.0	1.5~20
Bend Angle, θ [°]	180	90,180	60~180
Re Number Range	10,000~ 50,000	60,000	10,000~100,000
Near-Wall Treatments	EWT	SWF,NEWF,EWT	SWF,NEWF,EWT
Closure Models	k-ε model, RSM	k-ε model, RSM	k-ε model, RSM

Table 2.2: Boundary conditions used in all simulations

Lulat	velocity inlet [m/s]	Calculated from the known Re and d
Inlet	turbulent intensity [%]	0.05
	turbulent viscosity ratio	1.0
Outlet	pressure outlet [Pa]	P _{static} =0
Wall	no-slip boundary [m/s]	u _{wall} =0

In Fig. 2.1, the geometry of a curved pipe is shown with an unspecified bend angle θ . The outer and inner bends of the pipes are labeled as "O" and "I", respectively. The boundary conditions in all simulations are specified to be uniform velocity at the pipe entrance. To ensure that the turbulent flow is fully developed before it enters the bend, a long entrance length 1 is roughly estimated using Eq. (2.13) (Spurk, 1997).

$$l=4.4Re^{1/6}$$
 (2.13)

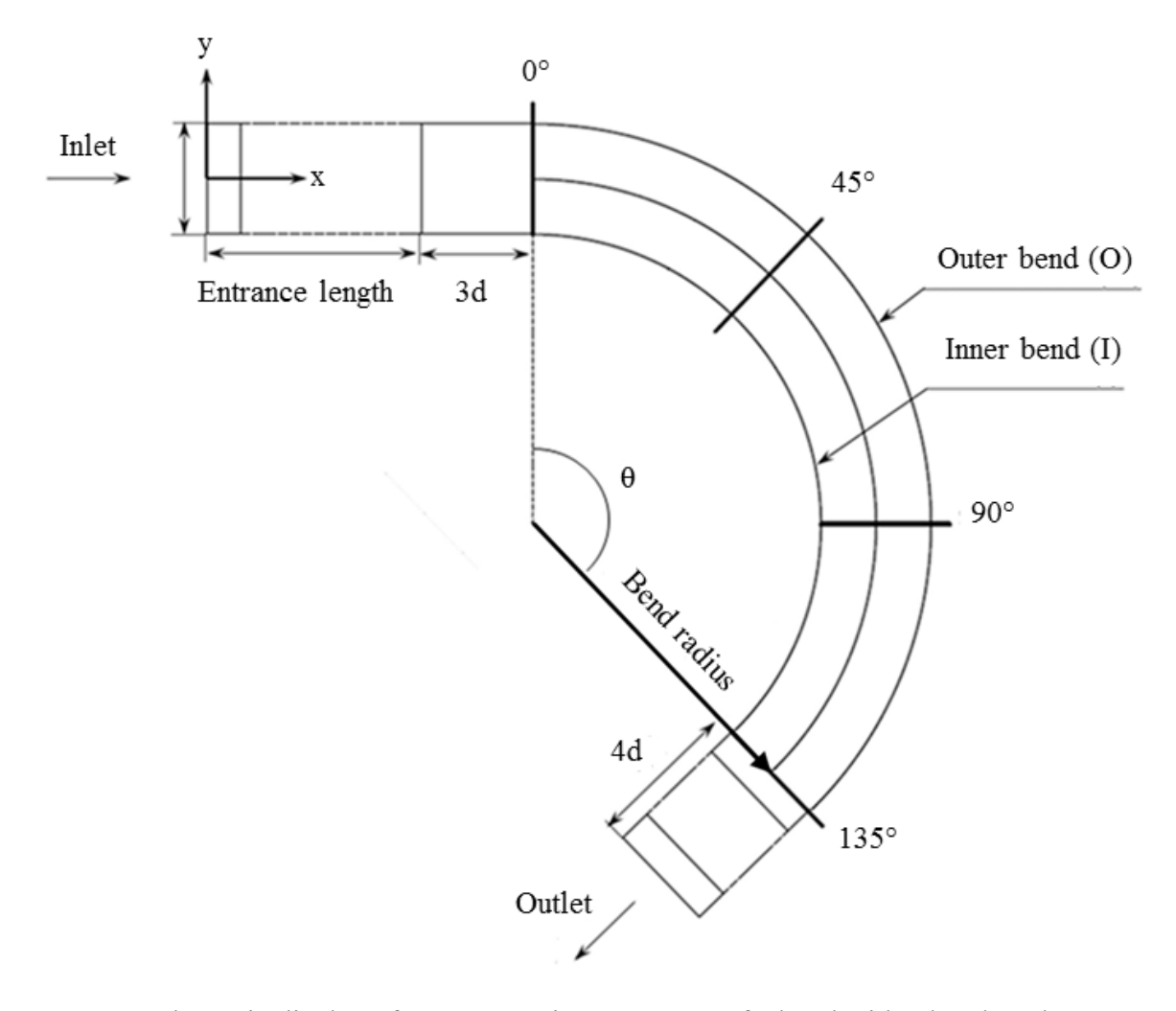


Figure 2.1: Schematic display of 3D geometric parameters of a bend with a bend angle θ .

At the pipe wall, a no-slip boundary condition is applied. The wall is "sticky" so that particles adhere to it on contact, which represent the conditions used in Pui et al.'s experiments (1987). Numerically, the trajectory calculations are terminated when particles enter the cell adjacent to the boundary. The boundary condition for the outflow is a pressure outlet with the static pressure equal to zero. The applied boundary conditions are summarized in Table 2.2. No heat transfer is considered in the process. Since the direction of the inlet flow is normal to the inlet cross section and its velocity is uniform, the turbulent intensity and turbulent viscosity ratio at the inlet are set to be small as recommended in ANSYS FLUENT 12.1 Documentation (2009).

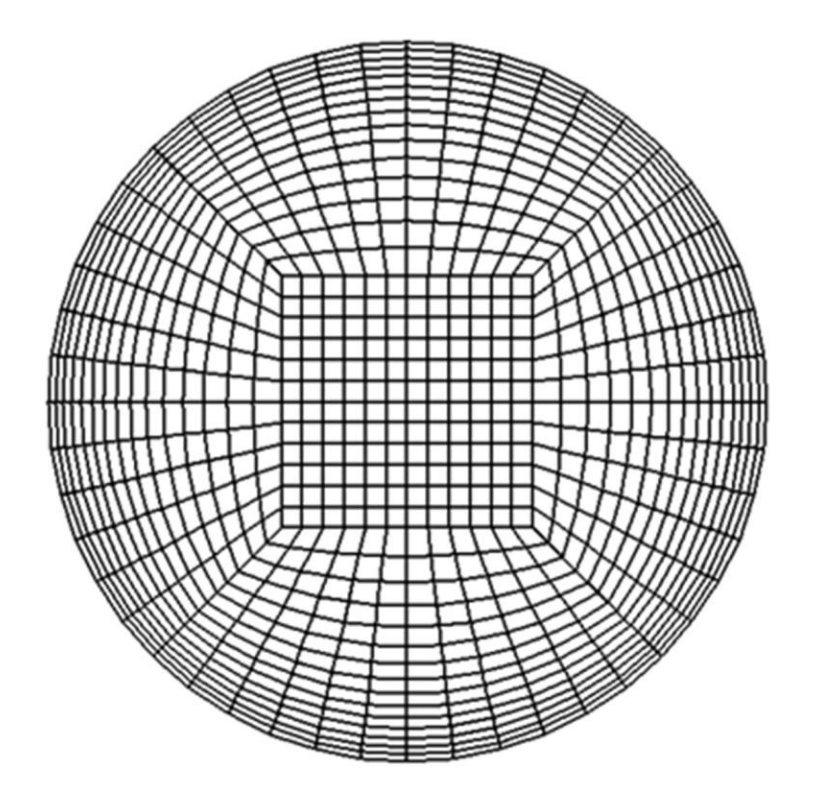


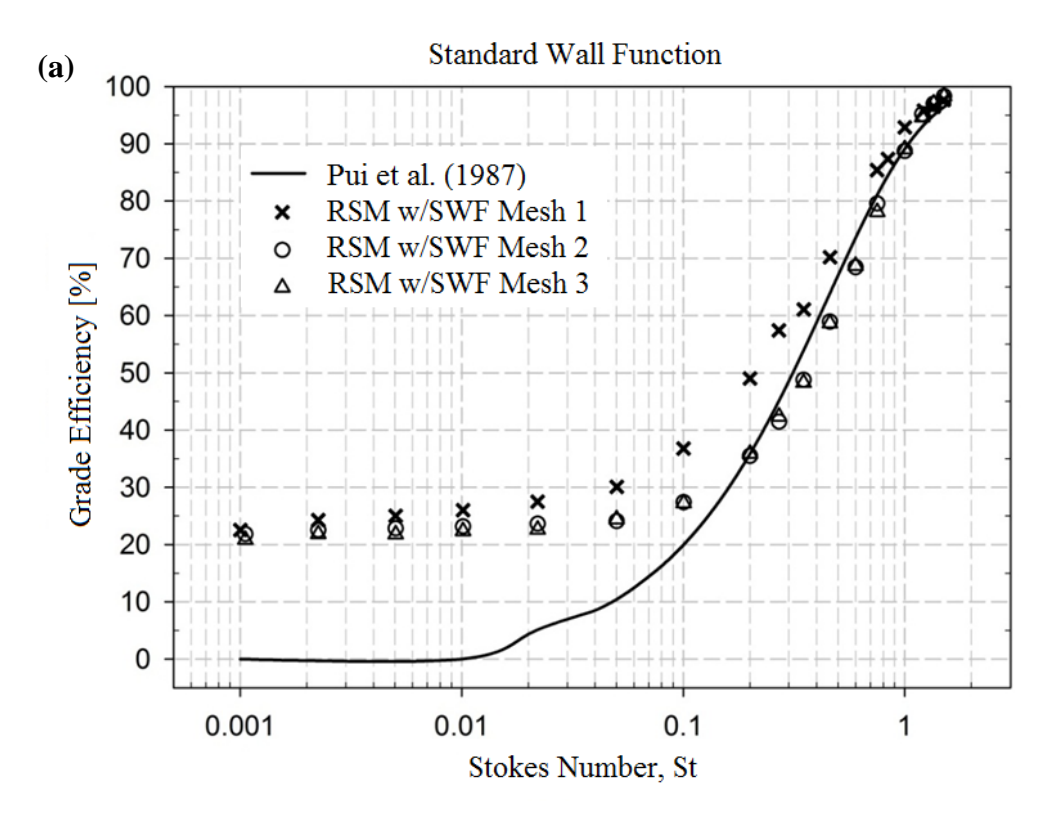
Figure 2.2: O-type structured mesh used for a cross section; this mesh allow easy refinement close to the wall and prevents a singularity at the center of the pipe.

The mesh construction for each cross section along the curved pipe is shown in Fig. 2.2. The density of the mesh is a function of the near-wall treatment used. The dimensionless distance y^+ = yu_{τ}/v is used to describe the distance from the wall, where y is the real distance of a location in the calculation domain from the wall; u_{τ} denotes the friction velocity and v is the kinematic viscosity of air. For SWF and NEWF, simulations using the distance of the first cell centroid from a wall has to be laid above the buffer layer at y^+ between 30 and 300 so that those semi-empirical equations are relatively accurate. For EWT, simulations using the centroid of wall-

adjacent cells is made at $y^+ \approx 1$ and at least 3 grid nodes are put inside the viscous sublayer ($y^+ < 5$) to ensure the accuracy of the numerical solution. A higher Re could cause a larger friction velocity and hence increase the y⁺ value at the wall-adjacent cells. Therefore, a refinement to the wall-adjacent mesh size is needed to meet the $y^+ \approx 1$ requirement according to the flow Re used. Along the mainflow direction of the pipe, the number of cross sections is changed according to the length of the pipes. To study the simulation convergence of the near-wall treatments in estimating particle deposition, different mesh density for pipe cross-sections and for the mainflow direction is used for SWF and EWT based on RSM. To reduce the computational effort, solution from the entrance length is used as the inlet boundary condition and only the segment after the entrance length (shown in Fig. 2.1) is refined for investigation. The mesh used for the grid independence study is summarized in Table 2.3. The mesh size is doubled at the crosssections as well as the main-flow direction. For example, SWF-Mesh1 uses 896 grid nodes for one pipe cross-section and 156 in the main-flow direction. For SWF-Mesh2, it possesses 1716 and 325 for one pipe cross-section and the main-flow direction, respectively. Meanwhile, the refinement has to maintain a mesh that meets the y⁺ requirement of the utilization of SWF and EWT.

Table 2.3: Mesh grid nodes used for the solution independent study

	Number of nodes for one cross-section	Number of cross-sections along the main-flow direction	Total mesh grid nodes
SWF-Mesh1	896	156	139,776
SWF-Mesh2	1716	325	557,700
SWF-Mesh3	3441	650	2,236,650
EWT-Mesh1	1044	156	162,864
EWT-Mesh2	2093	325	678,132
EWT-Mesh3	4096	650	2,662,400



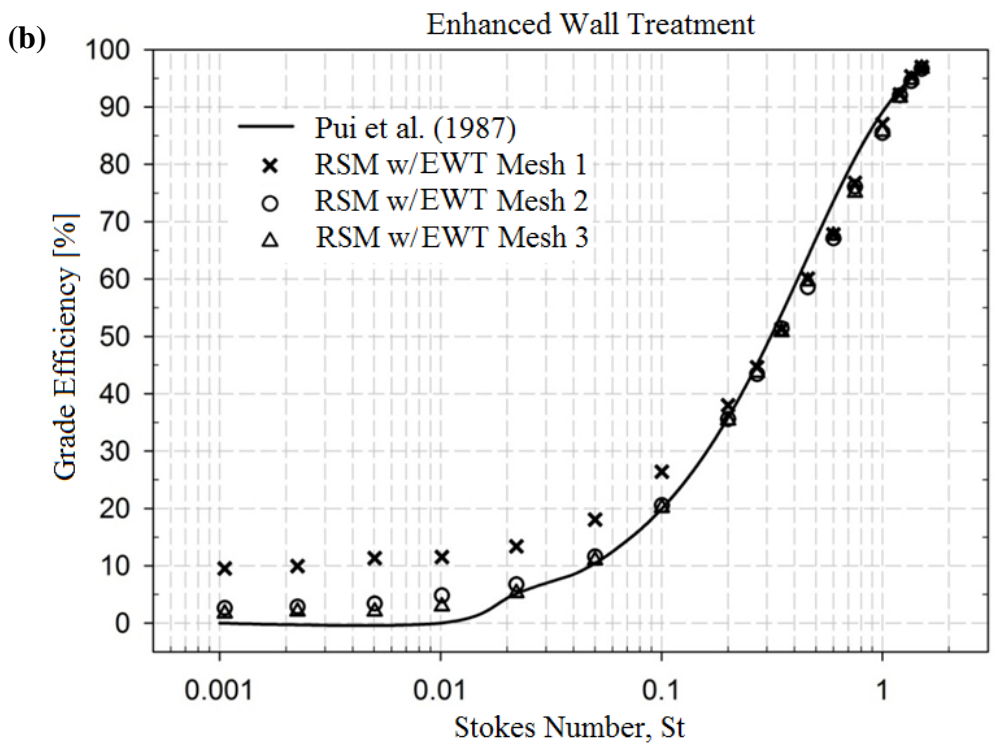


Figure 2.3: Independent study of particle deposition using RSM with (a) SWF and (b) EWT.

Before performing computations on pressure drop, flow patterns and particle deposition, a mesh independence study was performed. The impact of the mesh on the particle deposition, which appears to most sensitive to the mesh, are reported below. The meshes shown in Table 2.3 are used to construct a 90° bend with δ =5.6 and d=8.51mm. The RSM with SWF and EWT is employed to compute the flow field. The resulting grade efficiency curves are compared to the empirical model of Pui et al. (1987) in Fig. 2.3. It can be seen that the SWF-Mesh2 and EWT-Mesh2 are appropriate i.e the solution does not change with a refined mesh. A comparison of the empirical model of Pui et al (1987) with the results obtained from SWF-Mesh2 and EWT-Mesh2 show a 22% and 3% discrepancies respectively at St=0.001. In the following, Mesh2 is used in the computations.

2.6 Results and Discussions

The complexity of the flow patterns observed in curved pipes and secondary flow intensity are first discussed below, followed by a comparison between the computation and the measurement of pressure drops and grade efficiency.

2.6.1 Flow Patterns and Secondary Flow Intensity

The flow patterns observed from the numerical simulations are presented in Fig 2.4-2.6. The streamlines are used to represent the flow pattern only. No information of flow intensity is indicated by the streamline density. The streamlines at the middle plane of a tight bend with δ =1.5 are shown in Fig. 2.4, in which a strong recirculation of the primary flow can be observed on the inner bend as the fluid is passing through the tight bend. Secondary flow patterns can be seen at various cross sections of the bend (at 0 $^{\circ}$, 45 $^{\circ}$, 90 $^{\circ}$, 135 $^{\circ}$, 180 $^{\circ}$ of deflection and after the recirculation, respectively). No secondary flows are observed at the 0 $^{\circ}$ deflection cross-section.

A pair of counter-rotating vortices is found at the 45 ° deflection and becomes distorted at 90 °. The pair then evolves or split into two pairs of vortex cells at the 135 ° deflection and becomes more distorted at the 180 ° deflection. The additional pair of vortices at the inner bend is caused by the recirculation which generates a low velocity zone at the inner bend. The recirculation leads to a high pressure drop at the bend. Moreover, the recirculation affects the downstream flow patterns and partially formed Dean vortices are observed.

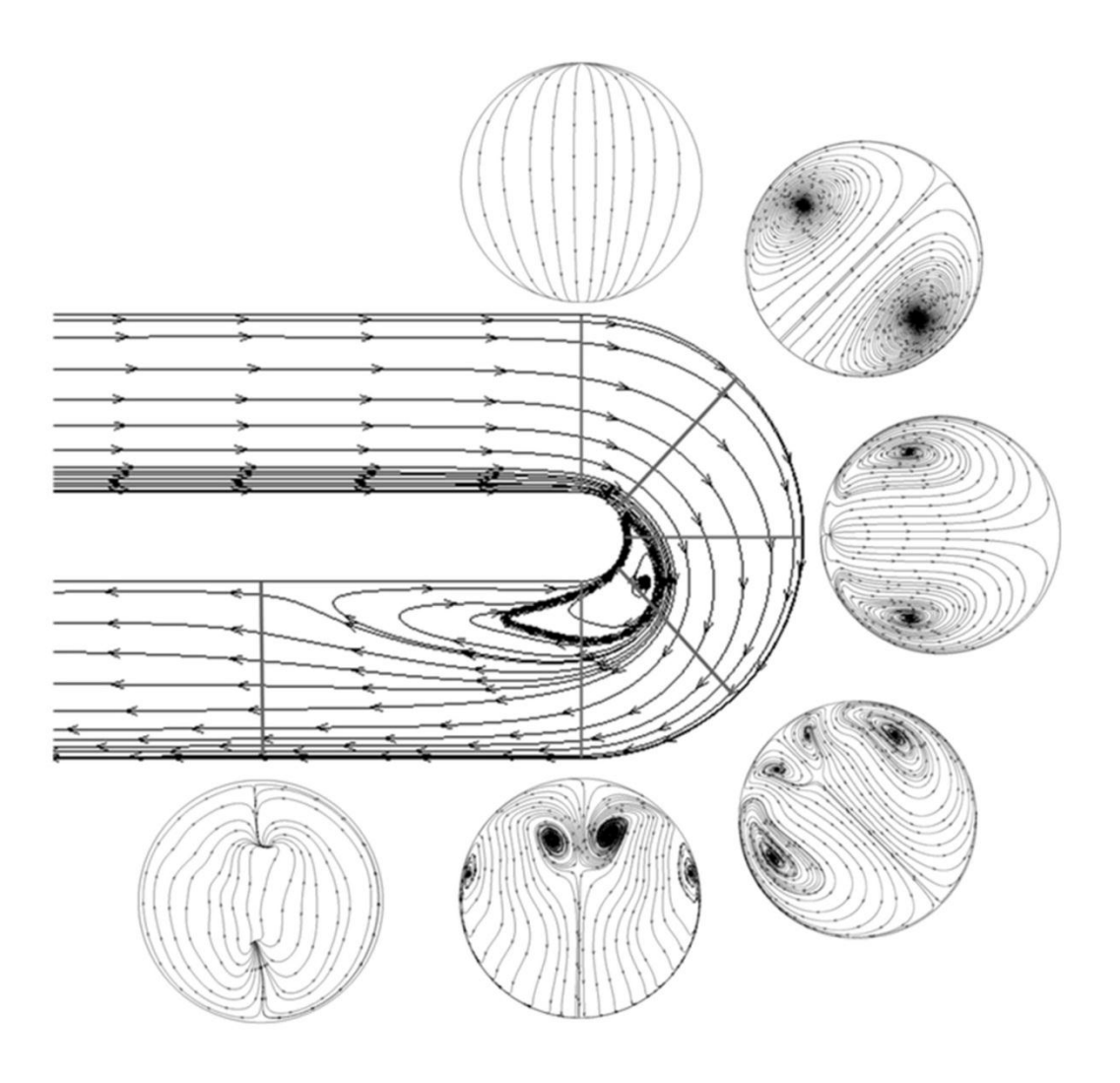


Figure 2.4: The streamlines show the development of flow patterns in a tight bend (δ =1.5); the secondary flows are also shown at different cross-sections.

No primary recirculation (along the main flow direction) is observed in a bend with δ=5.6 from the simulations performed with the standard k-ε model and RSM. Numerical results of flow patterns as well as secondary flow intensity are presented in Fig. 2.5. Flow patterns situated at a 45 °, 90 ° and 135 ° deflection angles estimated by the standard k-ε model combined with EWT are shown in Fig 2.5a, 2.5b and 2.5c and compared with those simulated by the RSM with the same near-wall treatment at the corresponding locations (shown in Fig 2.5d, 2.5e and 2.5f). The flow is turbulent with a Re=10,000. The streamlines at all cross sections show pronounced secondary flows with faster flowing central part of the flow. These results are consistent with the observations of Berger et al. (1983), who found that the pressure gradient caused by the centrifugal force around bends drives the flow near the wall to move inward, while the faster-moving fluid in the core is swept outward.

The graphs at the 45 ° deflection show that very different patterns are observed for RSM and the standard k-ε model. The RSM estimates two pairs of counter-rotating vortices induced by the Coriolis and centrifugal forces, but the standard k-ε model only estimates one pair. At the 90° deflection, the standard k-ε model estimates an extra pair of vortices at the inner bend, which is very weak. In addition, vortices simulated by the RSM are more distorted than those estimated by the other model. At the 135 ° deflection, the vortices by RSM are located very close to the wall and highly distorted, which is not the case for the secondary flow estimated by the standard k-ε model. Experimental measurements performed in a 180° bend show that curvature effects are responsible for producing anisotropic turbulence in the core of the turbulent flow (Chang et al., 1983). Ito (1987) observed that anisotropic turbulence cannot be reproduced by calculations performed with a k-ε model using a standard Boussinesq model for closing the Reynolds stress.

The selection of the closure model is probably the reason for the differences in the flow patterns estimated by the two closure models.

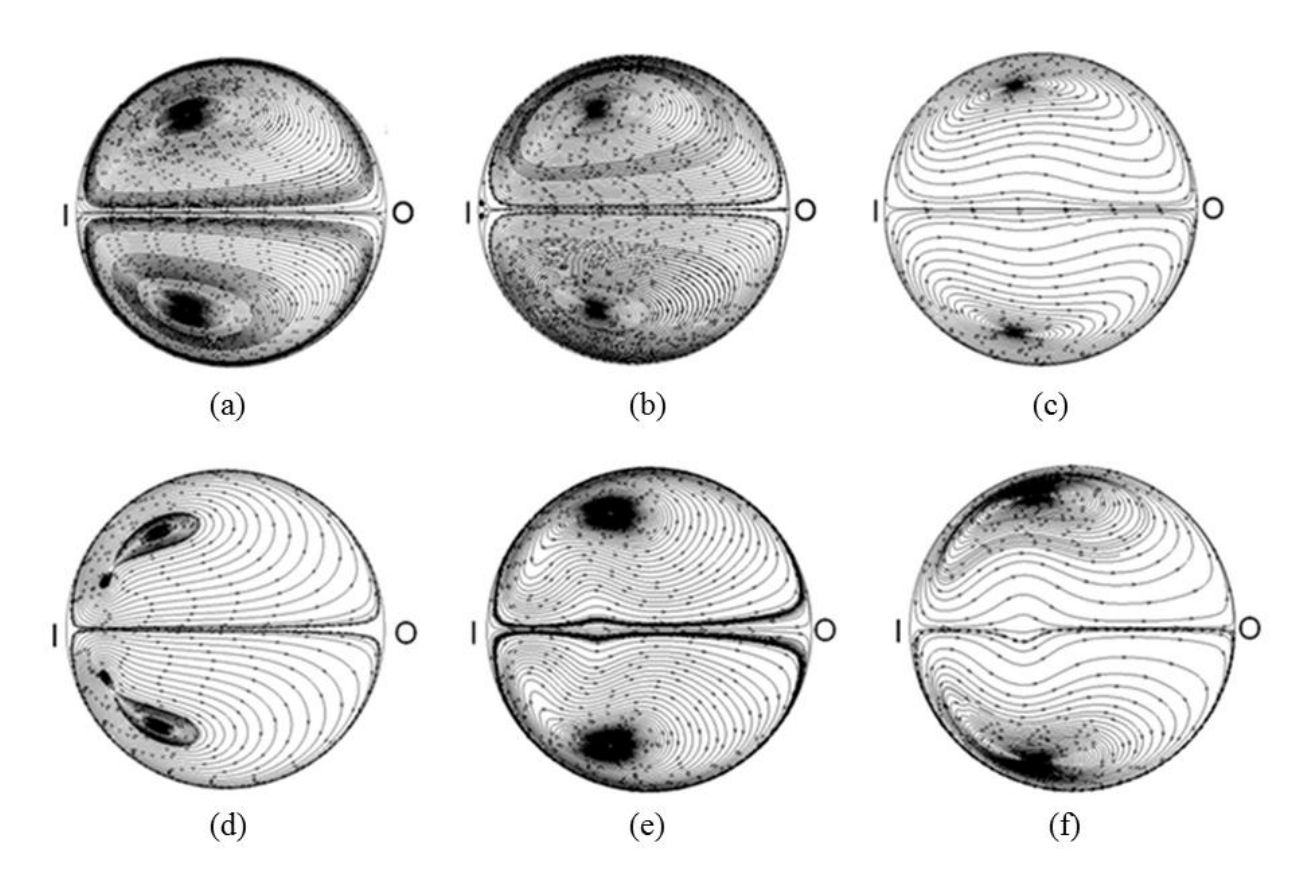


Figure 2.5: The streamlines associated with secondary flow patterns are studied at a 45 $^{\circ}$, 90 $^{\circ}$ and 135 $^{\circ}$ deflection and shown in (a), (b) and (c) by the stand k- ϵ model and in (d), (e) and (f) by the RSM.

In Fig. 2.6, flows with a Reynolds number equal to 10,000, 30,000 and 50,000 are used and the flow patterns at a 135 ° deflection of the same bend are compared. Instead of two cells of vortices for flow with Re=10,000, four and six cells are observed at the higher Reynolds number.

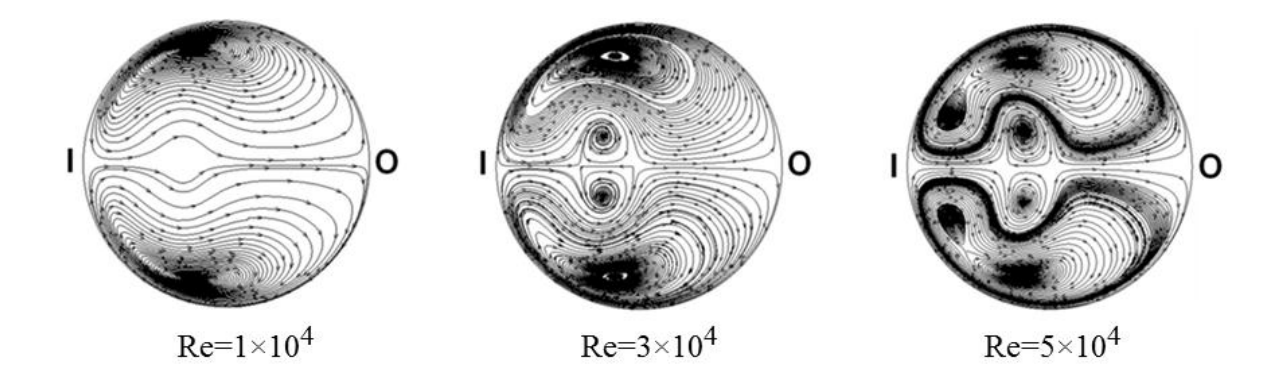


Figure 2.6: Plots of the streamlines associated with the in–plane flow patterns at 135 $^{\circ}$ in a U-bend with δ =5.6 to demonstrate the effect of an increasing flow Re number.

2.6.2 Pressure Drop along Curved Pipes

Calculations of the pressure coefficient (Cp) along the 90° bend and the 180° bend are compared to the experiments of Sudo et al. (1998 and 2000) in which the pressure coefficient is computed with

$$Cp = (P - P_{ref}) / (\frac{1}{2} \rho U_0^2)$$
 (2.14)

where P denotes the local static pressure, P_{ref} represents a reference pressure and ρ is air density (1.225 kg/m³). The flow has a mean velocity of 8.7 m/s and is passing through a bend with a radius ratio of δ =4. The flow is turbulent with Re=60,000. The local static pressure is estimated by using the standard k- ϵ model and RSM with different near-wall treatments.

Comparison between the numerical results and the experimental pressure along the outer bend, inner bend, and at the center are shown in Fig 2.7 and 2.8. The numerical static pressure is extracted from the locations slightly inside the outer bend wall (1 µm away from the wall), the inner bend wall and right at the center, respectively. The variables z' and z are the pipe longitudinal coordinates used to locate a cross section along the pipe direction and d is the pipe

diameter. The cross sections at the beginning and the end of the bend are located at z'=0 and z=0, respectively. The reference pressure is the pressure located at the outer bend at the cross section z' =-17.6d from the beginning of the bend. Comparison of the local static pressure estimated by the standard k-ε model and RSM combined with EWT in the 90-degree bend and the 180-degree bend is provided in Fig. 2.7. In Fig. 2.7a, the local pressure through the bend estimated from the standard k-ε model and the RSM is plotted. The lines obtained from the standard k-ε model and the RSM are hardly distinguishable. For the 90° bend, the maximum discrepancy between the experimental Cp and the numerical Cp estimated by both models is located at the 45 ° deflection of the inner bend wall, the numerical error is 7%. In the 180° bend, the performance of both models in estimating the local pressure worsens. On the outer bend wall, the maximum error occurs at 60 ° deflection with discrepancies of 21% and 26% for the standard k-ε model and the RSM respectively. On the inner bend wall, the maximum discrepancy is observed at the 75° deflection for both models with the same 26% error. Simulations results from both models with EWT match the empirical model curve well in the 90-degree bend, but underestimate the local pressure at the inner wall and the outer wall of the bend portion in the 180-degree bend, as shown in Fig. 2.7b. This seems to indicate that both models are performing well in short bends (small residence time), but for flows with a longer residence time the local pressure is not estimated accurately.

In Fig. 2.8a, all three near-wall treatments are observed to be capable of modeling the local pressure along the outer wall and the side wall of the 90° bend. At the inner bend, however, results computed from the SWF and NEWF overestimate the local pressure at the inner wall of the straight pipe after the bend. A large discrepancy of 34.5% is observed at the inner pipe wall located at the downstream 0.5d. The plot shows that results from EWT have a better agreement

at those locations. For the $180\,^{\circ}$ bend in Fig. 2.8b, SWF and NEWF seem to improve the results along the inner wall and the outer wall of the U-bend portion. The maximum errors at the $60\,^{\circ}$ deflection of the outer bend and at the $75\,^{\circ}$ deflection of the inner bend are reduced to 18% and 5%, respectively. Nevertheless, all methods estimate an accurate pressure drop when compared to the experiment measurement. Hence, they all appear suitable for bend design in estimating pressure drop.

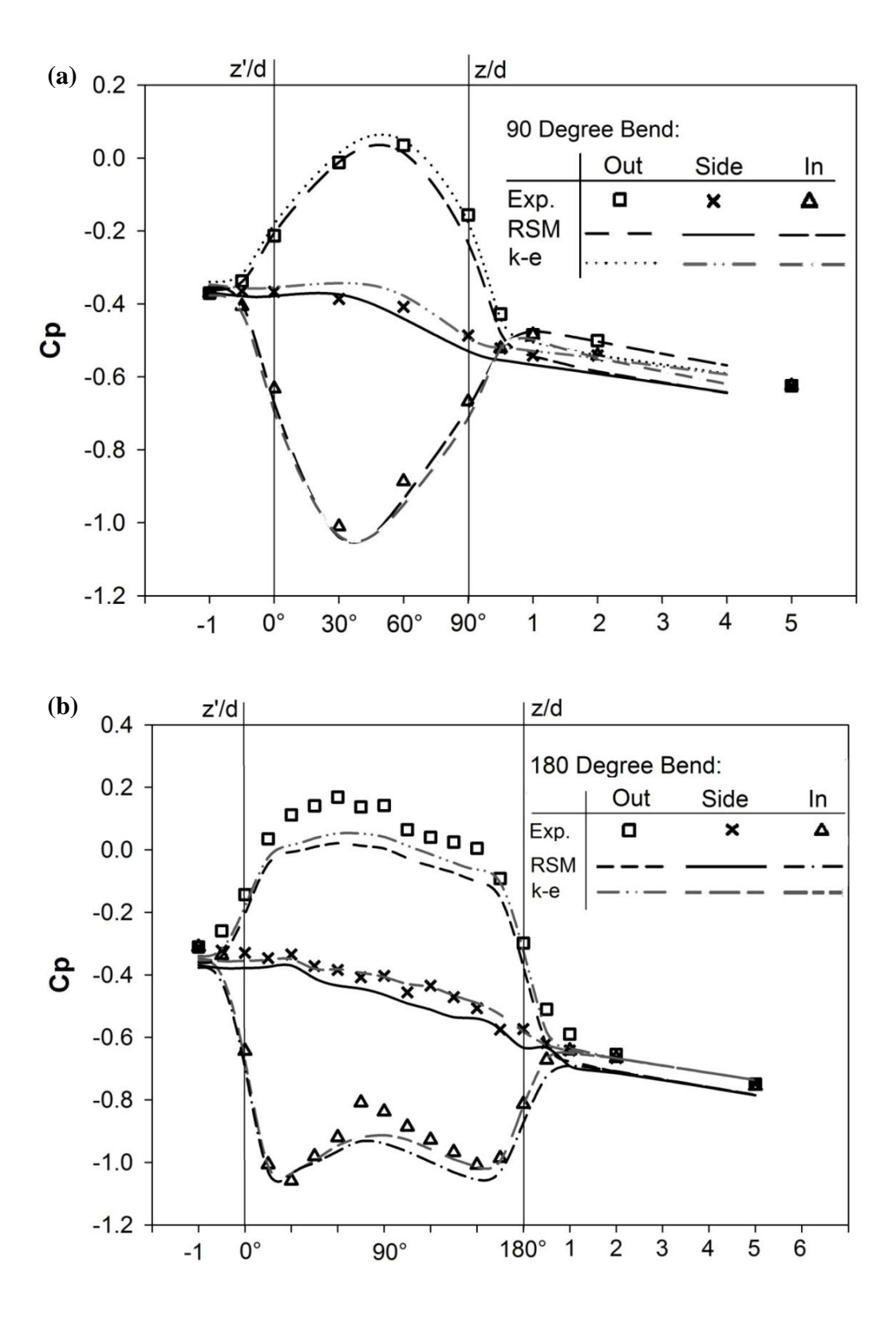


Figure 2.7: A comparison between the computed (markers) and estimated (lines) pressure drop values by using different closure models combined with EWT.

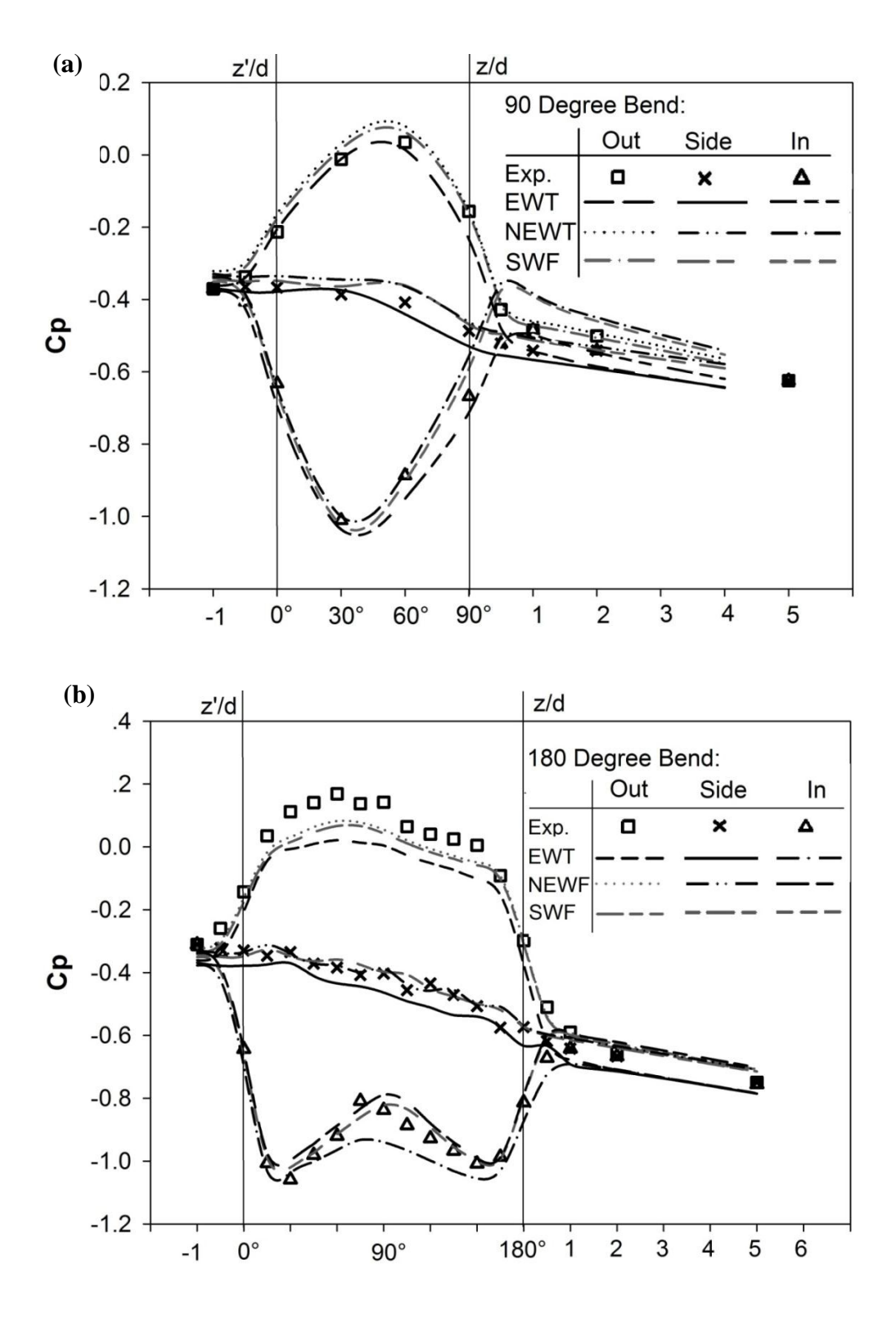
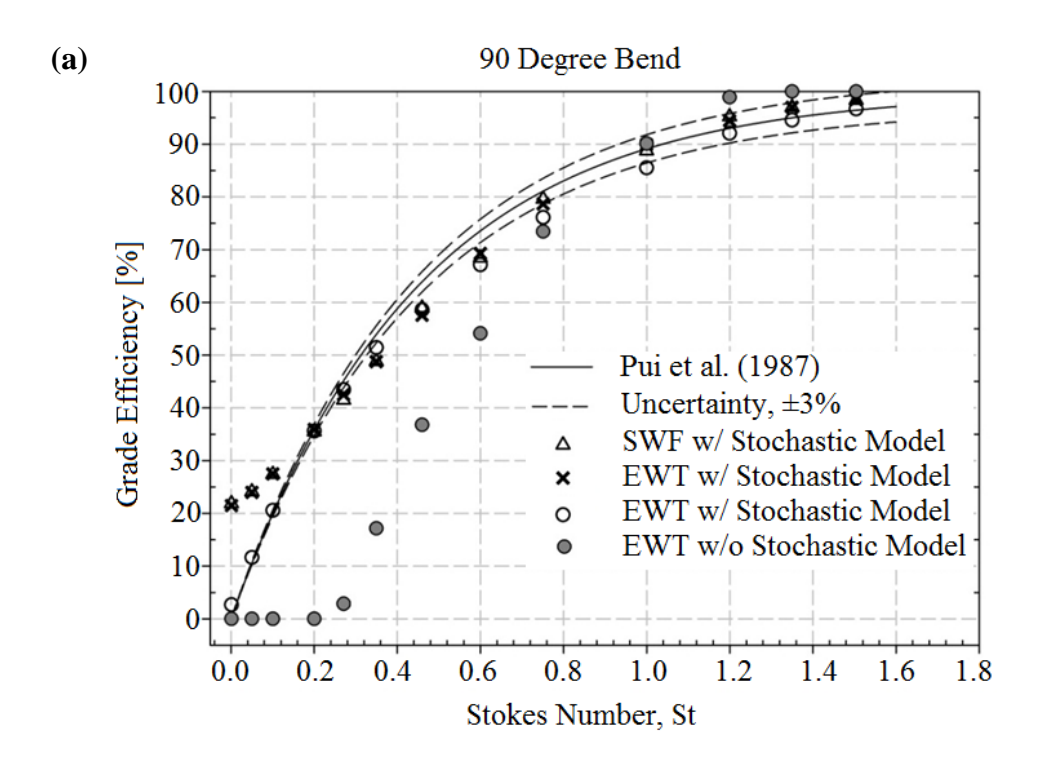


Figure 2.8: A comparison between the computed (markers) and estimated (lines) pressure coefficient (Cp) from near-wall treatments is made at the outer bend, inner bend, and the sides.

2.6.3 Modeling Particle Deposition

Grade efficiency curves for the 90° and the 180° bends computed from the RSM, combined with different wall functions and the stochastic turbulent model, are plotted against St and shown in Fig. 2.9 along with the results computed from the empirical models. The results from SWF and NEWF are in relatively good agreement for large St. However, when the value of St becomes small, a large discrepancy from the experiments can be observed. Fig. 2.9a shows that the maximal discrepancy (of 22%) occurs for a very small value of St (St=0.001) for both SWF and NEWF in the 90° bend. In the 180° bend, Fig. 2.9b shows a 40% discrepancy for SWF and 43% for NEWF. Numerical error of SWF and NEWF increases when a flow is under a high streamline curvature for a longer travelling time of the particles in bends. Small particles are very sensitive to turbulent fluctuation because of their fast response to the system. The failure of the SWF and NEWF to adequately capture the turbulent fluctuations near the wall may explain this deviation. On the other hand, results computed using an EWT agree very well with the experimental data and the maximum deviation of the comparison is only 3% at St=0.001. Comparison in Fig. 2.9b of the grade efficiency between numerical simulation and the models in the U-bend shows a higher deviation (of 10%) than that in the 90° bend at St=0.001. But a great improvement by using EWT can be observed in the Figures. The EWT appears to capture more accurately the actual velocity profile in the boundary layer especially if separation and strong streamline curvatures occur. The SWF and the NEWF were formulated from empirical data obtained from a straight bend and are probably not appropriate for particle deposition in flows with strong streamline curvatures. In addition, since SWF and NEWF use thicker wall-adjacent cells, the odds increase for small particles to hit the wall-adjacent cells and be counted as



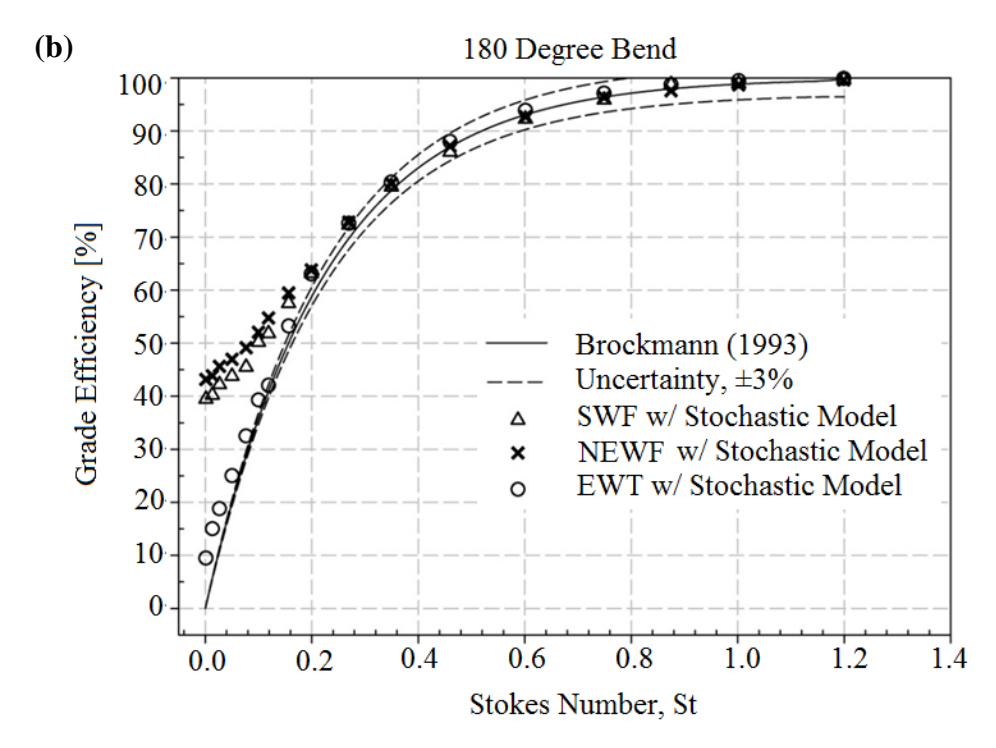
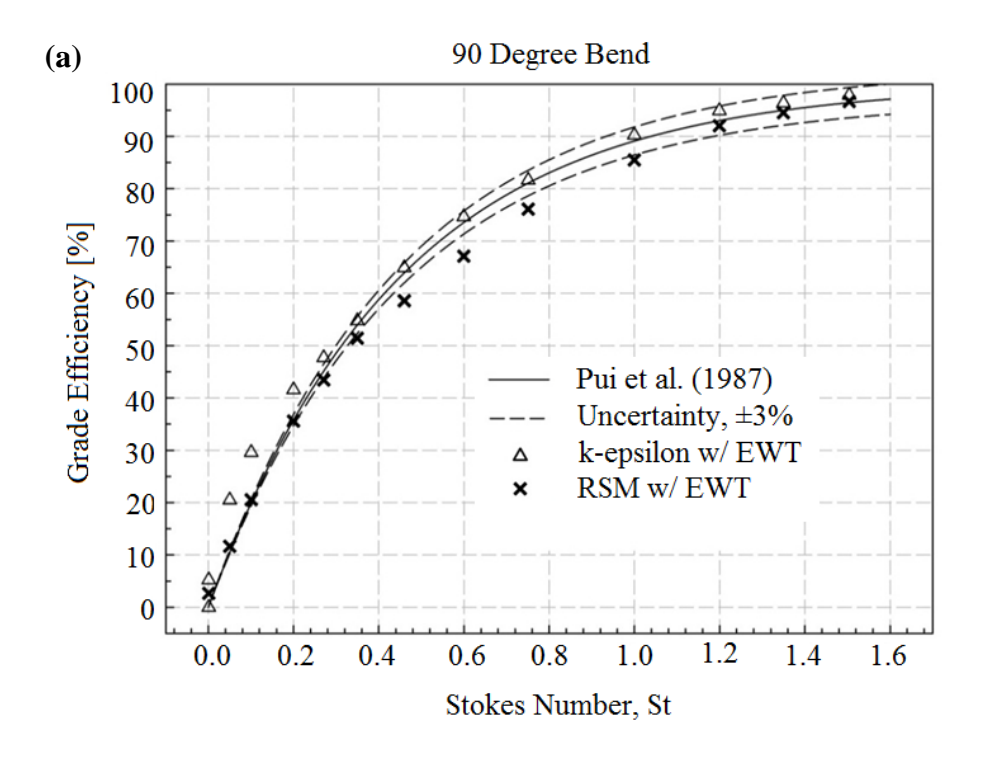


Figure 2.9: A comparison between computed and experimental data for the grade efficiency shows a discrepancy occurs at small value of St for SWF and NEWF and great improvement by using EWT in: (a) the 90-degree bend, (b) the 180-degree bend.

"deposited". Therefore, a more accurate estimation of small particle deposition is expected when compared to SWF and NEWF. All the near-wall treatments perform well on estimating the grade efficiency for large particles. With the particles become larger, the influence of the continuous flow becomes minor due to their large inertia.

To see whether using the stochastic model is necessary, particle tracking is also run without considering the effect of turbulent fluctuation by turning off the stochastic model. Comparison in Fig. 2.9a shows a very poor agreement in the 90 ° bend without using the stochastic model. Small particles are especially sensitive to the fluctuating velocity because of their low inertia, which account for the great discrepancy of the model when not considering particle dispersion.

In Fig. 2.10, a comparison is presented between the grade efficiency curves obtained from the numerical results and the models. The standard k- ϵ model and RSM are used in the computations in combination with EWT and the stochastic model. In Fig. 2.10a, both grade efficiency curves obtained from the models agree with the experiment well in the 90° bend. It is difficult to identify which model is more accurate in estimating the grade efficiency. However, the k- ϵ model estimates a maximum deviation of 10% at St=0.05 while the RSM obtains 3% at St=0.001. Moreover, the error averaged over the range of St is 4.5% for the RSM, which is slightly lower than that for the k- ϵ model. Apparently, one can see from the Fig. 10.b that the performance of the standard k- ϵ model worsens in estimating the particle deposition in the 180° bend. In this case, the standard k- ϵ model and the RSM estimate the maximum discrepancy of 13% at St=0.1 and 8% at St=0.001, respectively. The error averaged over the range of St is 9.5% and 6% for the standard k- ϵ model and the RSM, respectively.



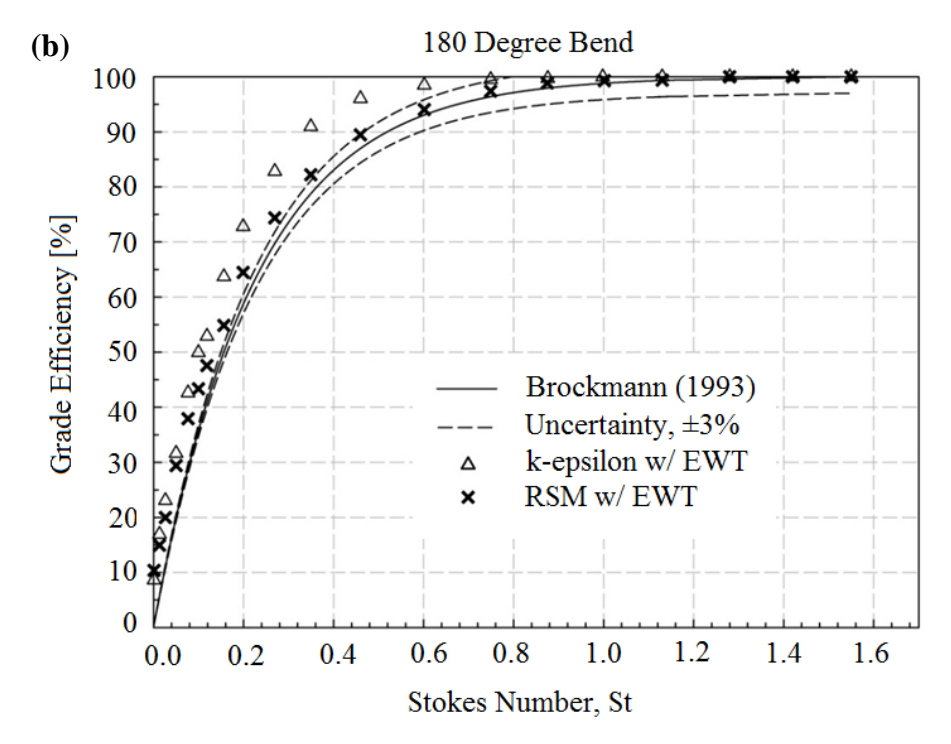


Figure 2.10: Comparison of the models (makers) and the empirical models (lines) shows that the k- ϵ model over-estimates particle deposition when particles experience a longer residence time in (b) the 180° bend (τ =4.4ms) than in (a) the 90° bend (τ =2.2ms)

The results from the RSM closure appear promising and more accurate than models with the Boussinesq eddy-viscosity approximation in simulating flow encountering strong streamline curvatures. This is attributed to the ability to capture the anisotropy of the turbulence fluctuating motion and thus lead to improved results of particle deposition. The results discussed below are thus all from simulations performed using an RSM with EWT due to the accuracy of this combination.

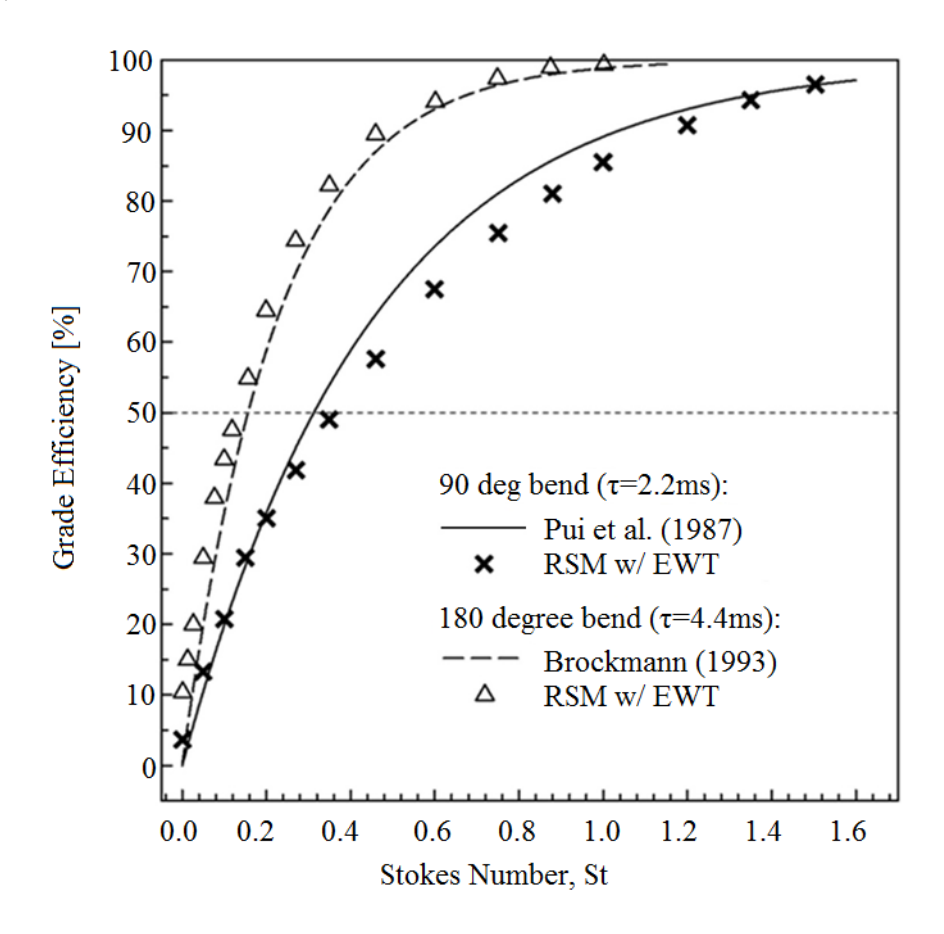


Figure 2.11: Comparison of grade efficiency shows that the particle cutsize is 30% smaller in the 180 °bend due to the longer particle residence time.

In Fig. 2.11 computed grade efficiency curves are shown for curved pipes for a changing particle residence time. The flow Re number is 10,000 in the 90° bend and the 180° bend with

the curvature ratio equal to 5.6. The time needed for the flow to the 90° bend is 2.2 ms and it is twice for the 180° bend. The grade efficiency for the U-bend is obviously larger than that for the 90° bend for the whole range of St, which indicates that particles experiencing a longer time inside a bend have larger chance to deposit on a pipe wall and thus higher grade efficiency can be obtained. The cutsize of a separation equipment is the size associated with a 50% probability that it will leave the equipment (the bend) with the fluid. The particle cutsize for the 180°-bend is 3/5 of that for the 90° bend.

The grade efficiency curves for 90-degree bends with different curvature ratios are calculated and plotted against the Stokes number in Fig. 2.12. The bend curvature ratio is increased from 1.5 to 20. The pipe diameter and the flow Reynolds number are maintained the same as 8.51mm and 30,000, respectively. Results show that the grade efficiency increases with an increase of the bend curvature ratio. The empirical model of Pui et al. (1987) appears to be appropriate to a bend with certain curvature ratio and should account for, or be modified to include, the bend curvature ratio. For a 90-degree bend, an increase of the bend curvature ratio actually increases the particle residence time in a bend, particles thus experience a centrifugal force for a longer duration.

The trend in Fig. 2.12 is likely due to the combined effects of the curvature ratio and the particle residence time. In order to investigate the effect of the bend curvature ratio, the particle residence time was fixed by using the same bend length in the simulations. The bend angles are thus different due to different curvature ratios used. Bends with curvature ratios of 3, 5 and 9 corresponding to different bend angles of 180°, 108° and 60° are studied to match the total travel time. A comparison of the computed grade efficiency with Brockmann's model (Eq. (2.11)) is shown in Fig. 2.13. The plot shows that the increasing curvature ratio reduces the grade efficiency of a curved pipe given the same total travel time. The centrifugal force is inversely

proportional to the bend radius, thus the increasing grade efficiency is due to a larger centrifugal force. This trend is consistent with the observation of the experiment done by McFarland et al. (1997). In Fig. 2.13, Brockmann's model appears to provide accurate results except for cases where the bend with curvature ratio equal to 9, which probably indicates that the model should also account for the effect of a bend curvature ratio.

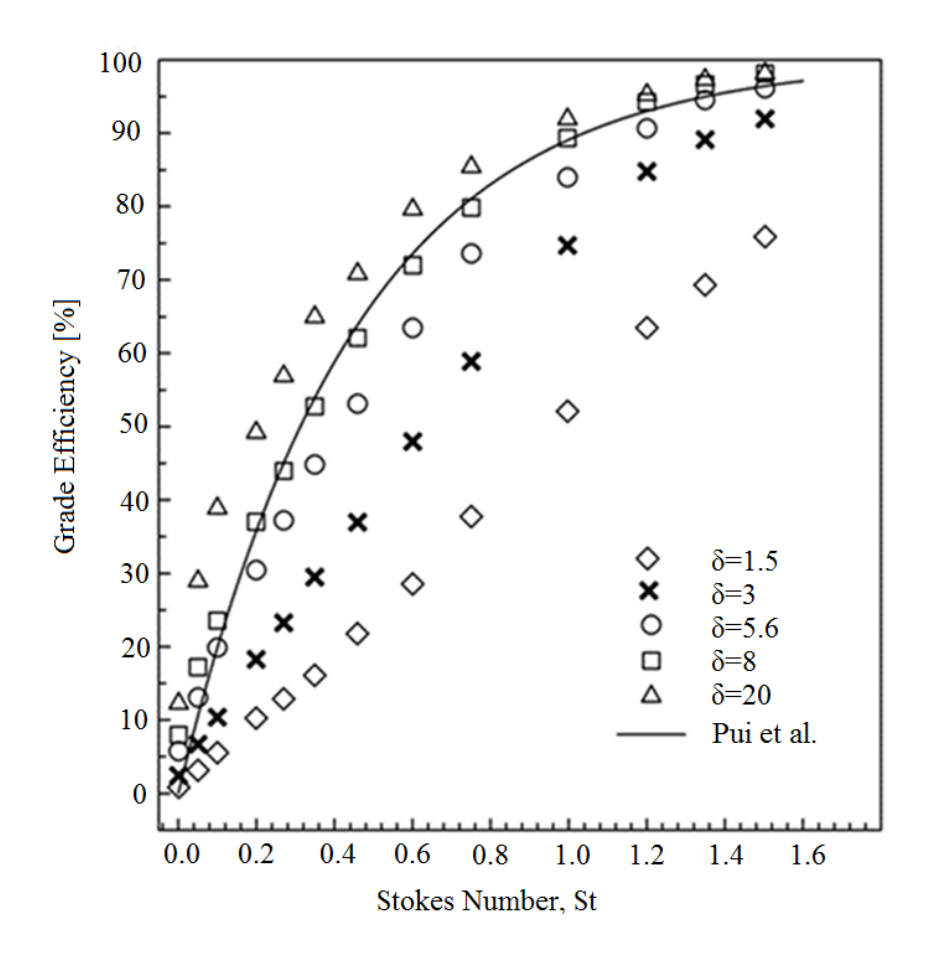


Figure 2.12: Comparison of bends with a varying curvature ratio for a fixed flow Reynolds number in a 90° bend shows the grade efficiency is increased with the increase of the curvature ratio.

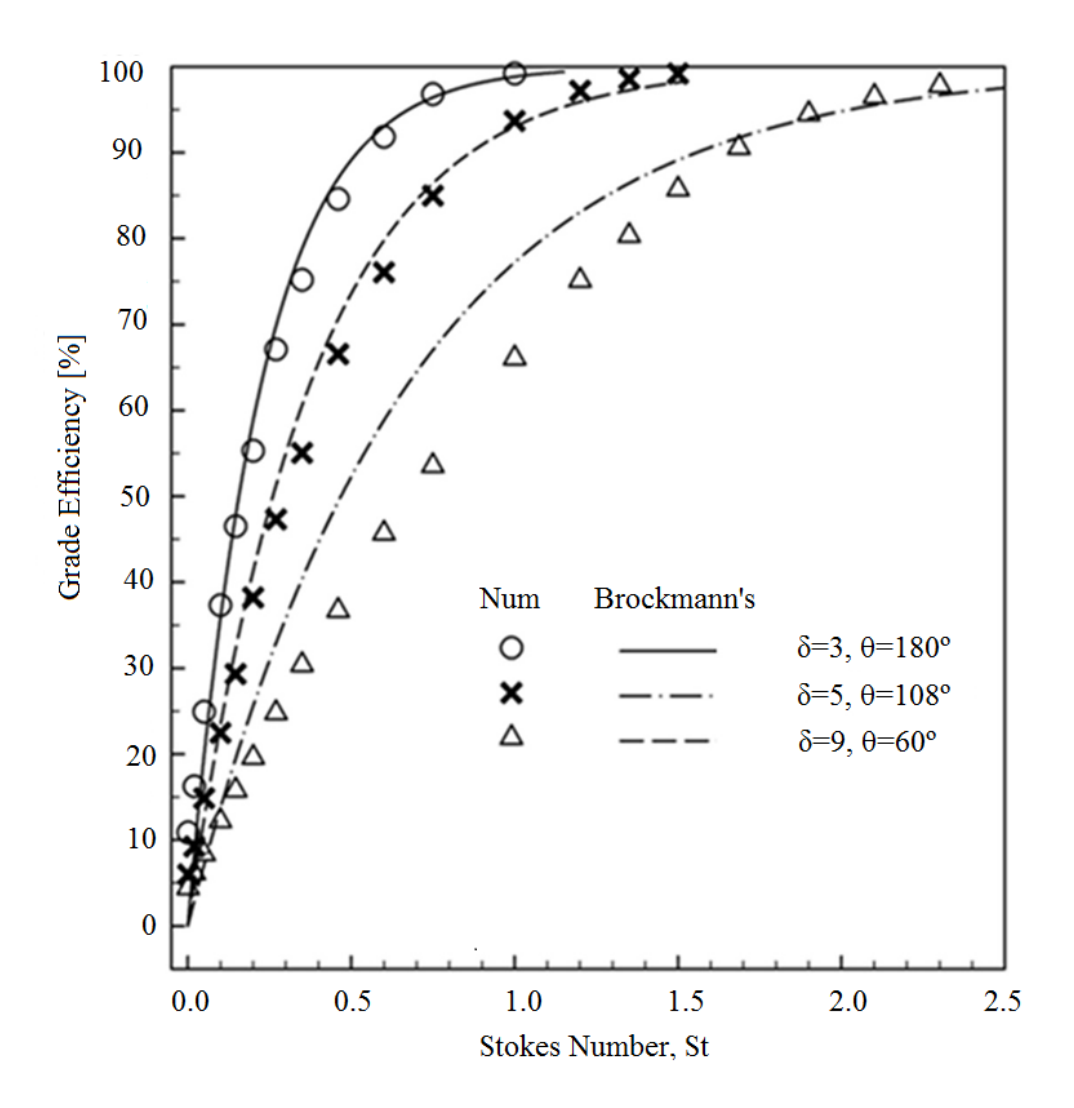


Figure 2.13: Comparison of results for curved pipes with different curvature ratio and fixed particle residence time shows the grade efficiency is increase with the decrease of bend curvature ratio.

Fig. 2.14a shows the comparison between the different numerical results and the empirical models from literature. Since the effect of δ is not included in the models of Pui et al. and Brockman, the models are not accurate in estimating η in a bend with a changing δ . Although MarFarland et al.'s model includes the effect of δ , a comparison with the grade efficiency curves

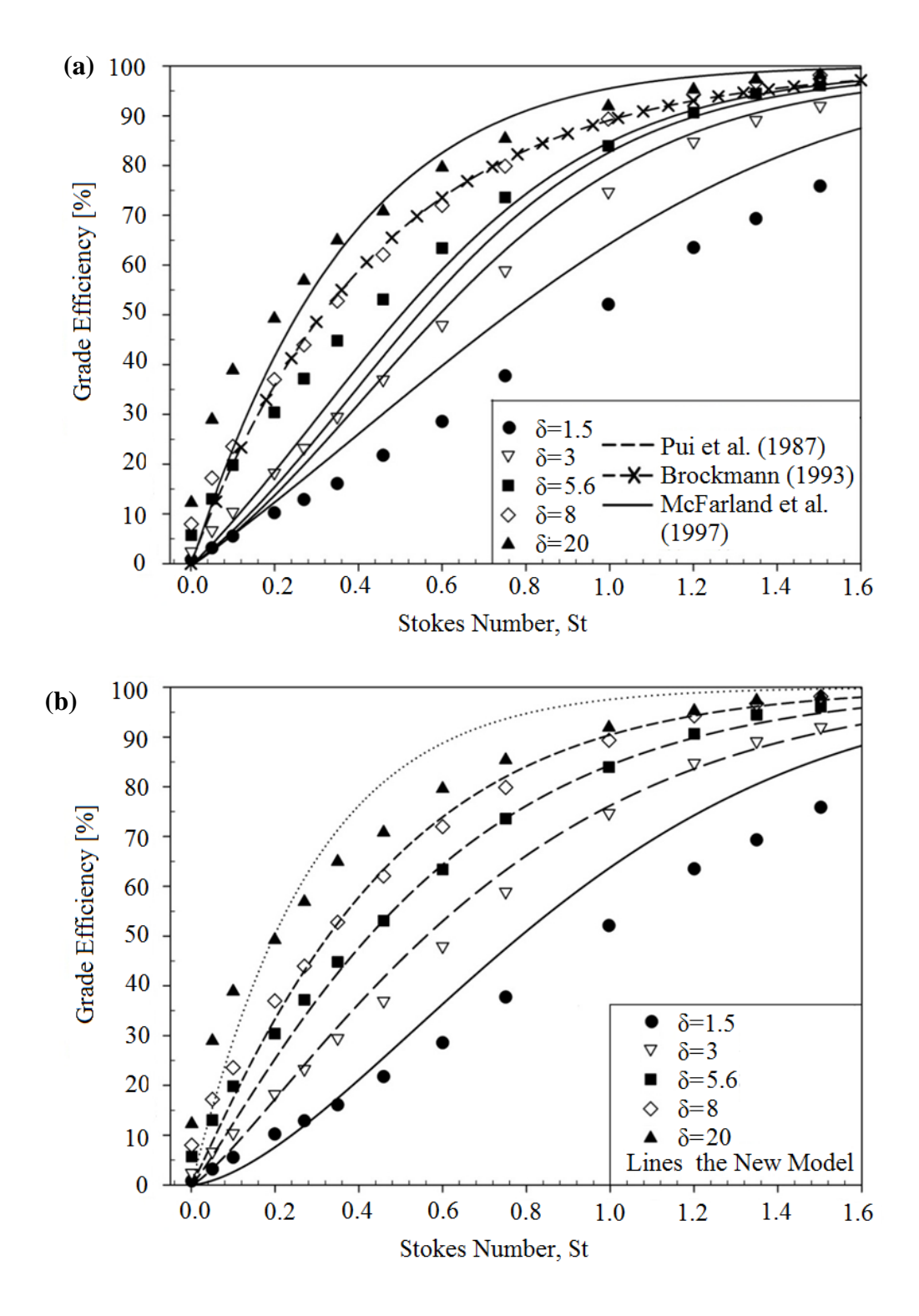


Figure 2.14: (a) Comparison shows that the models are not appropriate for varying δ in a 90 ° bend (b) Comparison shows the new model match the results relatively well for δ between 3 and 8 but has reduced accuracy at extreme curvature ratios.

estimated from the models of Pui et al. and Brockmann are very different and it does not match the numerical results for the cases studied. Based on the numerical results, a new model is proposed to account for the effect of the St number, the bend angle, and the bend curvature ratio on the grade efficiency. To fit the numerical results, the model is given as

$$\eta = \left[1 - \exp\left(-0.528\theta \operatorname{St}^{21/\delta} \delta^{0.5}\right)\right] \times 100\% \tag{2.15}$$

This model is derived by curve fitting, without accounting for the numerous physical processes encountered over the range of parameters considered. The comparison is shown in Fig. 2.14b. The curves show that the new model fits the numerical results well for the cases when the curvature ratio is from 3 to 8. For δ =3, the curve obtains a maximum discrepancy of 5% at St=0.5. The maximum discrepancies for δ =5.6 and δ =8 are 7% and 7.5% at small Stokes number St=0.1 and St=0.05, respectively. According to the previous study in this work, some errors are caused by the overestimation of the grade efficiency of the numerical model at a small St number. This indicates that the maximum deviation at small St is lower than the plot shows. Therefore, the new model is actually very accurate for the cases discussed above. Extraordinary cases like δ =1.5 and δ =20 are not fitted by this model. For δ =1.5, a recirculation flow is generated in the tight bend. For δ =20, an extremely long bend may need to consider other factors for particle deposition such as entrainment. Therefore, those cases should be excluded when using this model.

Fig. 2.15 shows the grade efficiency of the 90-degree bend under different flow Re numbers. The pipe diameter and the bend curvature ratio are fixed at 8.51mm and 5.6, respectively. The Re number is increased from 10,000 to 100,000 and the results are plotted against St. The comparison shows that the grade efficiency has a deviation of 9% when the Re number increases by a factor of 10, which indicates that the effect of flow Re number is insignificant. This

conclusion is consistent with the statement of Pui et al. (1987). The effect of changing Re number is actually accounted by using the St number. Since the particle size d_p is inversely proportional to the mean axial flow velocity U_0 , higher Re number will give a smaller particle cutsize.

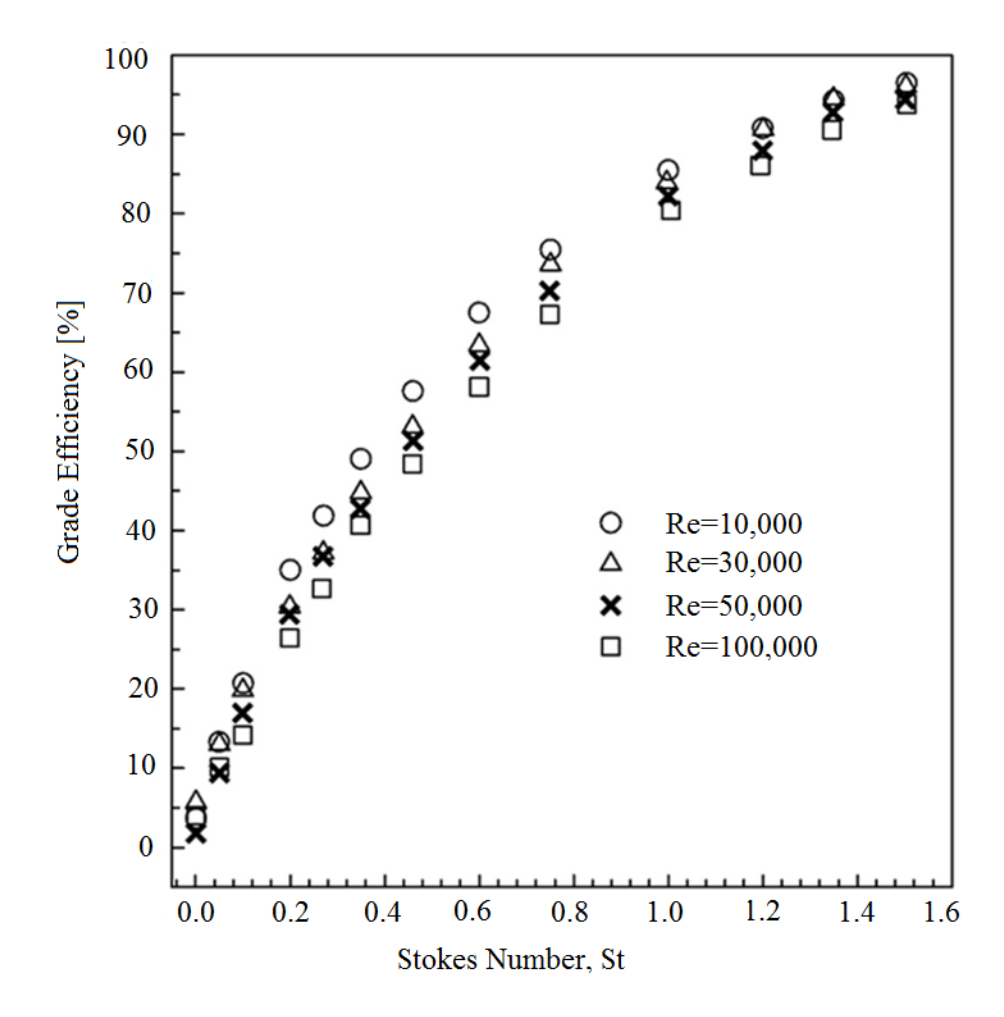


Figure 2.15: Comparison of grade efficiency shows a deviation of 9% when the Re number increases by a factor of 10.

Since one is often interested in studying particle deposition in bends of various dimensions, the effect of changing the diameter is shown in Fig. 2.16. The Reynolds number is 30,000 for all the simulated cases and the bend curvature ratio is held at 5.6 in a 90 °bend. The plot shows that the particle cutsize is significantly affected by the pipe dimension. The results indicate that the grade efficiency of the particles is decreased with the increase of the pipe size.

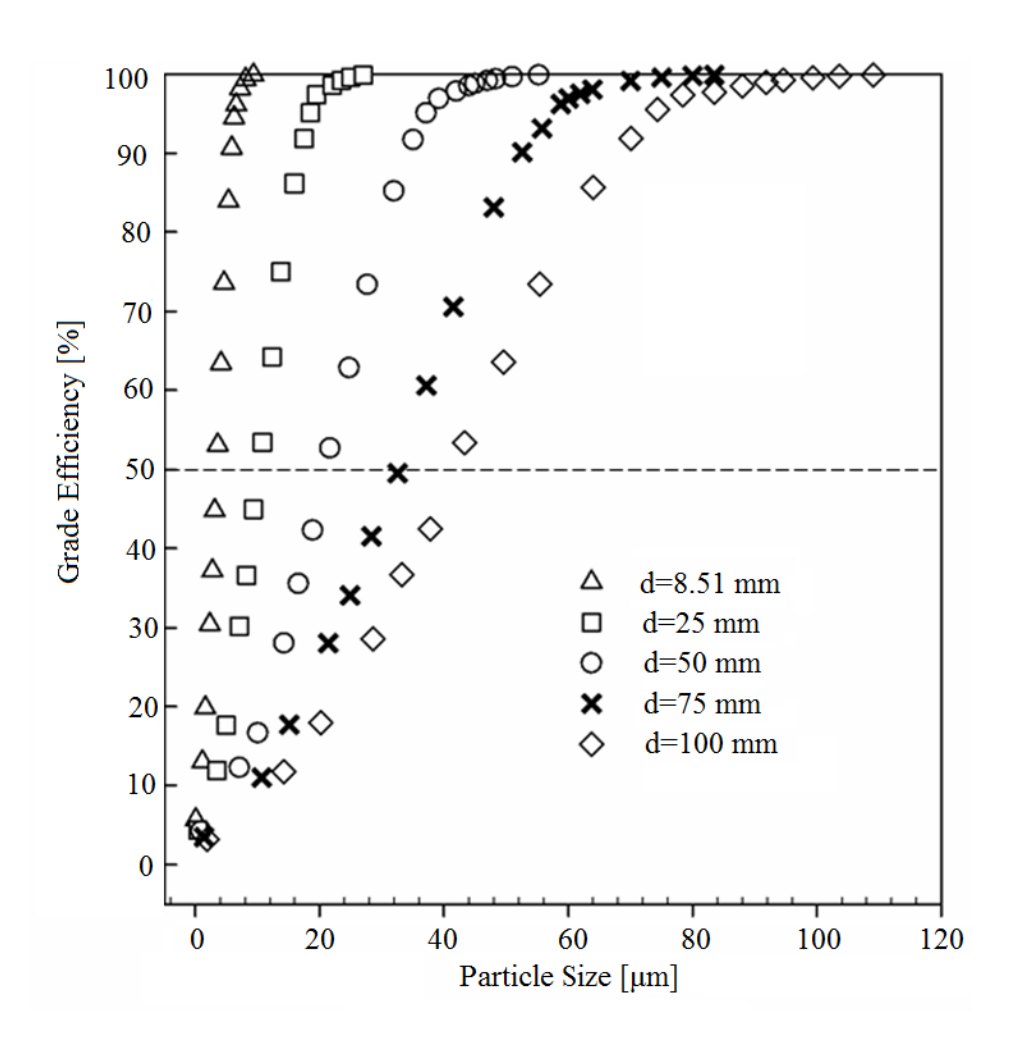


Figure 2.16: Comparison results show the particle cutsize is increased as the increase of the pipe dimension.

Particle deposition patterns in the 90 ° bend with d=8.51mm and δ =5.6 are plotted with an increasing value of the St number in Fig. 2.17. The flow Reynolds number for this case is 10,000. All results are computed using EWT with a mesh that satisfies the required conditions. When values of the St number are very small and equal to 0.001, approximately 3% of particles were captured by the pipe wall. Deposition of small-size droplet due to turbulent fluctuations can account for this small amount of deposition. From the definition of Stokes number (see Eq. (2.9)), it can be seen that low values of the St number indicate a fast particle response time, and thus correspond to particles that will follow closely the continuous flow. In this case, most particles pass through the bend and only a small number of particles are trapped on the pipe wall because of the flow fluctuating velocity. When the particle size increases (higher St number), particles with high inertia tend to cross streamlines and deposit on the outer part of the bends because of the centrifugal force (see Fig. 2.17e-g). Similar deposition patterns can be observed in a 180-degree bend.

To decrease the cutsize and increase the pressure drop, either decrease the curvature ratio, increase the residence time, or decrease the duct diameter, holding the other two parameters constant. If pressure drop is not a concern, high particle deposition efficiency can be expected for situations where a small pipe diameter d, a small bend curvature ratio τ , as well as a long residence time τ are adopted. To accurately estimate the particle deposition, a turbulence closure appropriate for flows with streamline curvatures should be used. In this work, the RSM is employed with the linear pressure-strain correlation. The selection of an EWT as the near-wall treatment is crucial in correctly estimating particle deposition along with constructing a high-quality mesh.

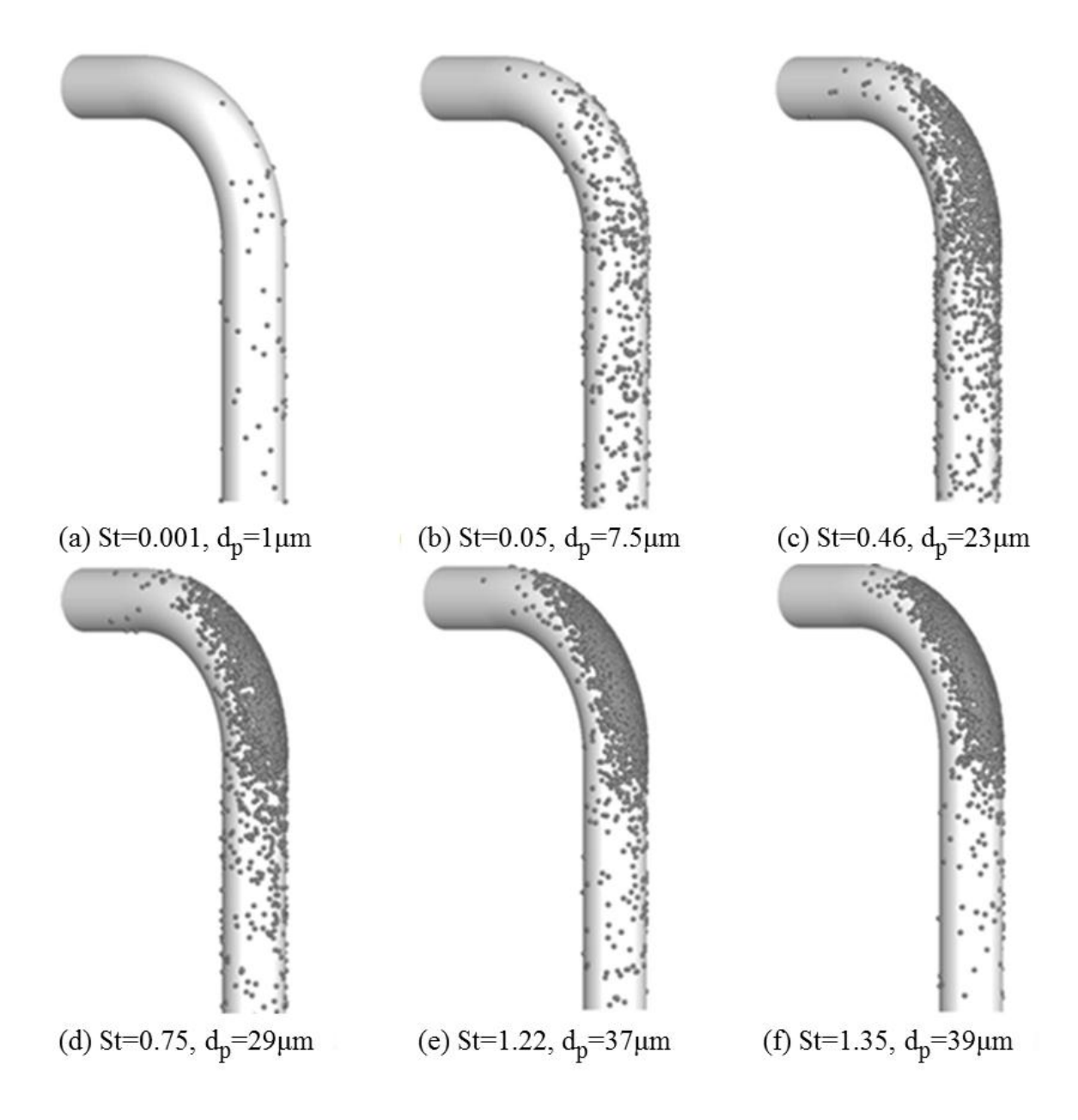


Figure 2.17: Estimation of deposition patterns of particles changes with Stokes number.

2.7 Summary

A dilute turbulent flow passing through circular curved pipes and particle deposition are studied in this work using computational fluid dynamic simulations. The simulations are

performed by solving the RANS equation and a force balance equation on the particles. Since the accuracy of such numerical simulations is often in question when compared with experiments, numerous case studies were performed to identify the potential source of the discrepancies. Empirical models were used to validate the computational results.

Results of these computations show that turbulent bend flows possess, as expected, complicated patterns influenced by the flow Re number and the bend configuration. Computed results for the pressure drop through a bend are obtained from different near-wall treatments based on the k- ϵ model and the RSM; all are close to experimental measurements provided that the mesh meets the y^+ requirement for the wall treatment selected except the local pressure at the outer and inner pipe of the U-bend.

The grade efficiency for particle deposition in curved pipes is influenced by the bend diameter d, the curvature ratio δ and the particle residence time inside the bend τ for a fixed flow rate. To decrease the cutsize and increase the pressure drop, either decrease the curvature ratio, increase the residence time, or decrease the duct diameter, holding the other two parameters constant. The selection of the turbulence model and the wall treatment were found to be crucial in these studies. Using RSM with EWT provides a much improved accuracy over the standard k- ϵ model in estimating particle deposition patterns. The inaccuracy of SWF and NEWF for particle deposition, when compared to EWT, indicates that these near-wall treatments are not appropriate for modeling particle deposition on curved surfaces; this is likely due to the importance of modeling the near wall fluctuations. In addition, a new model is developed to estimate the grade efficiency of particulate flow in bends which include the effect of the curvature ratio. The given model is an improvement in the empirical models of Pui et al. (1987) and Brockmann (1993).

The study of this work also provides the range of application of the empirical models discussed.

Broad guidelines for designing a bend with a high deposition efficiency are finally provided.

CHAPTER 3

SIMULATION OF DILUTE TURBULENT MIST FLOW IN CURVED PIPES USING AN EULERIAN-EULERIAN METHOD

3.1 Introduction

In parts of the study presented in in Chapter 2, it is found that bends are associated with a large pressure drop for single-phase flows. Particle trajectories obtained from the Lagrangian particle tracking method also indicate that phase separation may occur when particulate-laden flows pass through curved pipes. For gas/liquid mist flows with a large mass loading, Hoang and Davis (1984) observed that the pressure drop associated with particle-laden flows is significantly greater than that of a single-phase flow. Crane (1957) summarized that the total pressure drop for an incompressible, adiabatic flow should include the contribution of wall friction, flow detachment, momentum exchange between phases and downstream flow velocity profile recovery. When mist flows pass through curved pipes, droplets may impinge on the pipe wall where they accumulate and form a wall film. In general, the structure of this film is stratified along the outer bend wall (Hoang and Davis 1984). However, Banerjee et al. (1967) observed that within certain ranges of liquid flow rate and gas flow rate this film can travel inversely from the outer band wall to the inner bend wall. This phenomenon is referred to as "film inversion". The consideration of bends is important in designing multiphase flows equipment and pipes. The liquid film may be mitigated by varying the pipe geometry to prevent pipe erosion and reduce pressure drop or, alternatively, promoted to improve the performance of a downstream separator.

The liquid film formation for gas/liquid flows passing through curved pipes has been vastly studied in the literature, mostly from an experimental standpoint [5, 27, 34, 36, 38, 66, 90]. Computational fluid dynamics (CFD) provides a means to study such complex flows. In Chapter

2, the one-way coupling DPM has been proven accurate and efficient for flows under the assumption of one-way coupling. To study the impact of the disperse phase and liquid film formation, the flow has to be considered two-way coupling. Two-way coupling mist flows can be modeled using the two-way coupling DPM where particle impact is treated as a momentum source in the transient momentum equation. However, using the two-way coupling DPM is very limited in film thickness for liquid film modeling (ANSYS FLUENT 12.1, 2009). Another drawback is that the method is computationally expensive in tracking a large amount since particles for fully coupled converged solutions are difficult to achieve. An alternative approach of modeling a two-way coupling flow is to use the drift flux model based on the mixture theory proposed by Manninen et al. (1996). The drift flux model has been broadly used in simulating aerosol deposition in human airways and fine particles (typically smaller than 1 µm) in laminar flows were usually studied in this field [62, 88, 110]. Hossain and Naser (2004) studied a turbulent bend flow with larger particles (2 µm - 20 µm) and showed that the method is promising in predicting the concentration of a gas-solid granular flow in a pipe loop with four 90° bends. However, the application of the drift flux model in predicting pressure drop and liquid film formation in bends cannot be found in literature.

In this Chapter, a study is performed for evaluating the performance of the drift flux model in predicting pressure drop and film formation of a turbulent mist flow when passing through a curved pipe. In addition, the numerical method is used as a tool for bend design related to pressure drop and deposition efficiency. The Realizable k-ε model was used to close the RANS equation. It would have been preferable to close the RANS equation with the Reynolds Stress Model but converged solutions for most multiphase flow problems studied here could not be obtained. The flow at the near-wall region is resolved by the enhanced wall treatment (EWT).

Numerical results allow verifying if the model is able to capture phenomena such as secondary flows and film inversion. Furthermore, the accuracy of the model was validated by comparing the numerical results of pressure drop with the empirical models from literature. Subsequently, the influence of parameters such droplet size d_p and the volume fraction of the water phase α_p on the flow patterns is studied, as well as on pressure drop, secondary flow intensity and the liquid film thickness. Finally, a bend allows for a low pressure drop and high droplet deposition efficiency is identified for a given flow condition.

3.2 Multiphase flow modeling

Multiphase flows can be categorized as gas-liquid, gas-solid, solid-liquid and liquid-liquid flows. Widely different processes are encountered in each flow and this makes it nearly impossible to find a universal model appropriate for simulating all possible situations. The selection of appropriate closures for a given theory will thus vary according to the nature of the flow studied. Eulerian-Eulerian methods found in the literature include the Volume of Fluid (VOF) model, the drift flux model, and the two-fluid model. The application of a VOF model requires significant computer resources to track in detail the movement of a liquid/gas interface. The two-fluid model can tackle a wide variety of flows but also requires significant computing effort due to the number of differential equations to solve. The drift flux model in the mixture theory appears to be efficient and can be accurate, it requires a smaller set of governing equation and provide the mixture properties of the multiphase flow studied [Manninen et al., 1996]; it is a statistical approach that does not provide the same information as a two-equation model. The mixture theory with a drift flux model of [Manninen et al., 1996] was selected in this work since it involves design and numerous simulations.

3.2.1 Multiphase turbulent flow modeling

The mixture theory is a set of governing equations that includes a balance of mass and a balance of momentum. A second continuity equation is needed to compute the volume fraction of the secondary phase. These equations result from phase averaging, followed by ensemble averaging. Equations similar to the Reynolds-Averaged Navier Stokes (RANS) equation for single phase flows are obtained. The equivalent of the Reynolds stress found in the momentum equation is closed using the realizable k-ɛ turbulent model; the coefficients used in the closure are those found for single phase flows. The averaged continuity equation for the air-water mixture is given as

$$\nabla \cdot (\rho_{\text{mix}} \mathbf{u}_{\text{mix}}) = 0 \tag{3.1}$$

with the mean mixture density

$$\rho_{\text{mix}} = \alpha_f \rho_f + \alpha_p \rho_p \tag{3.2}$$

and the mean mixture velocity

$$\mathbf{u}_{\text{mix}} = (\rho_f \alpha_f \mathbf{u}_f + \rho_p \alpha_p \mathbf{u}_p) / \rho_{\text{mix}}$$
(3.3)

where ρ is the density; α is the volume fraction; u is the instant velocity; the subscript "f" and "p" denote the carrier phase and the disperse phase. In this work, the carrier phase is air and the disperse phase is water droplets.

The drift flux model allows different phases to be interpenetrable with a volume fraction characterizing each phase. The summation of the volume fraction of all phases satisfies

$$\sum_{k=1}^{n} \alpha_k = 1 \tag{3.4}$$

For a gas/liquid two-phase mist flow, the liquid is treated as the disperse phase. The distribution of the liquid phase is determined by the value of the liquid volume fraction α_p in the flow domain.

The media is liquid for $\alpha_p=1$ and gas for $\alpha_p=0$. It is a mixture for the liquid volume fraction between 0 and 1. The liquid volume fraction is obtained from a transport equation derived from mass balance and is given as

$$\nabla \cdot (\alpha_{p} \mathbf{u}_{mix}) = -\nabla \cdot (\alpha_{p} \mathbf{u}_{dr,p}) \tag{3.5}$$

where $\mathbf{u}_{dr,p}$ is called the drift velocity for the liquid phase which needs to be closed through models. It defined as the velocity difference between the droplet velocity and the mixture velocity, given as

$$\mathbf{u}_{\mathrm{dr,p}} = \mathbf{u}_{\mathrm{p}} - \mathbf{u}_{\mathrm{mix}} \tag{3.6}$$

To model the above drift velocity, one relates it by convention to the phase slip velocity, obtained

$$\mathbf{u}_{\mathrm{dr},p} = \mathbf{u}_{\mathrm{f},p}(1 - \mathrm{G}_{\mathrm{p}}) \tag{3.7}$$

The slip velocity $\mathbf{u}_{\mathrm{f,p}}$ is a difference between the gas phase and the liquid phase defined as

$$\mathbf{u}_{f,p} = \mathbf{u}_p - \mathbf{u}_f \tag{3.8}$$

G_p is the mass fraction of the water phase defined as

$$G_{p} = \alpha_{p} \rho_{p} / \rho_{mix} \tag{3.9}$$

The momentum equation as presented in Manninen et al. (1996) for the mixture is given as

$$\nabla \cdot (\rho_{\text{mix}} \mathbf{u}_{\text{mix}} \mathbf{u}_{\text{mix}}) = -\nabla P + \rho_{\text{mix}} \mathbf{g} + \nabla \cdot (\mathbf{\tau}_{\text{m}} + \mathbf{\tau}_{\text{Tm}})$$

$$-\nabla \cdot [\rho_{\text{mix}} G_{p} (1 - G_{p}) \mathbf{u}_{f,p} \mathbf{u}_{f,p}]$$
(3.10)

where τ_m and τ_{Tm} are the viscous shear stress and the turbulent shear stress which are closed by using the following constitutive equations according to Johansen et al. (1990):

$$\boldsymbol{\tau}_{\mathrm{m}} = \boldsymbol{\mu}_{\mathrm{mix}} (\nabla \mathbf{u}_{\mathrm{mix}} + \nabla \mathbf{u}_{\mathrm{mix}}^{\mathrm{T}}) \tag{3.11}$$

$$\boldsymbol{\tau}_{Tm} = \rho_{mix} \boldsymbol{\nu}_{T} (\nabla \mathbf{u}_{f} + \nabla \mathbf{u}_{f}^{T}) + \rho_{p} D_{p} (\mathbf{u}_{f} \nabla \alpha_{p} + \mathbf{u}_{f,p} \nabla \alpha_{p})$$
(3.12)

where the mixture dynamic viscosity is defined as

$$\mu_{\text{mix}} = \alpha_f \mu_f + \alpha_p \mu_p \tag{3.13}$$

According to Picart et al (1986), the diffusion coefficient for the liquid phase D_p is given as:

$$D_{p} = v_{T} \left(1 + 0.85 \frac{\mathbf{u}_{f,p}^{2}}{2k/3} \right)^{-1/2}$$
(3.14)

where v_T is the turbulent viscosity for the gas phase, defined as

$$v_{\rm T} = C_{\mu} \frac{k^2}{\varepsilon} \tag{3.15}$$

An essential prerequisite of using the drift flux model is to close the slip velocity in Eq. (3.7), (3.10), (3.12), and (3.14). Ishii (1975) developed the algebraic slip model based on an assumption of a local equilibrium. The constitutive equation for the slip velocity is given as

$$\mathbf{u}_{f,p} = \frac{\tau_p}{f_{drag}} \frac{(\rho_p - \rho_{mix})}{\rho_p} (\mathbf{g} - \mathbf{u}_{mix} \cdot \nabla \mathbf{u}_{mix})$$
(3.16)

The droplet relaxation time τ_p is given in Eq. (2.5). The disperse liquid phase is treated as solid spherical droplets with a single diameter d_p . Drop breakup, drop coalescence, and droplet interaction are ignored. Under this assumption, the drag function f_{drag} is proportional to the Reynolds number of the mixture Re_{mix} obtained from the empirical measurement of Schiller and Naumann (1935) for a turbulent flow passing a spherical particle, given as

$$f_{drag} = 0.0183 Re_{mix}$$

$$(3.17)$$

A simplified version of the mixture model can be achieved for a homogenous flow which assumes that the velocity difference between the phases $\mathbf{u}_{f,p}$ equals to zero. This kind of flow is out of the scope in this work since the slip velocity is significant due to the gravity and the centrifugal force induced by a bend.

3.2.2 Turbulence closure

To complete the formulation of the turbulent mixture momentum equations, transport equations need to be solved each for the turbulent kinetic energy k and the dissipation rate ε, respectively. The realizable k-ε two-equation model [Shih et al., 1995] is used in this work based on the Boussinesq viscosity assumption [Boussinesq, 1877]. Any model based on an eddy-viscosity approach has shortcomings for flows with strong streamline curvatures but this option the only available choice that could converge easily with EWT. Using the approach of Pourahmadi (1982), the transport equations are extended to a two-phase flow. The equations are presented in Appendix A for the sake of brevity.

3.2.3 Near-wall treatment

From Chapter 2, the EWT was proven to be the most accurate near-wall treatment method in dealing with particle deposition in curved pipes. Since studies will be focused on droplet deposition and liquid film formation on pipe wall of a mist air-water flow, the EWT is used in this work for the near-wall treatment.

3.3 Numerical methodologies

The governing equations are solved in a steady and adiabatic state in the commercial code ANSYS FLUENT 12 using a SIMPLE algorithm (Patankar and Spalding 1972). The transport equations for k and ε are spatially discretized using a second-order upwind scheme. A correction equation derived from the continuity equation and the momentum equation for pressure is discretized using the same PRESTO! scheme as we did in the previous chapter. The Quick Scheme (quadratic upstream interpolation convective kinetics), a higher-order unwinding method proposed by Perng and Street (1989), is employed for computing the volume fraction of the droplet phase α_p . The stability of the numerical computations is improved by reducing the underrelaxation factor to 0.2 for the pressure, 0.5 for the momentum and 0.001 for the slip velocity. The residual criterion for convergence (the "monitors") is set to 10^{-4} for all variables. Meanwhile, three monitors including the difference of the mass flow rates at the inlet and the outlet of a bend, the area-average weighted pressure and the flow rate of the secondary phase at the bend exit are used to ensure a converged solution.

3.4 Geometry and meshing

The geometric configuration and the mesh construction can be referred to Fig. 2.1 and Fig. 2.2 in Chapter 2. Compared to the one-way DPM, the drift flux model is more computationally expensive for more equations need to be solved. To reduce the computational effort, a fully developed velocity profile as well as the turbulent intensity profile based on the flow Reynolds number is applied to the entrance of the pipe as the boundary conditions in all simulations. At the pipe wall, the no-slip boundary condition is applied. The boundary condition for the outflow is

set as pressure outlet with the static pressure equal to zero. The applied boundary conditions are summarized in Table 3.1. No heat transfer is considered in the process.

3.5 Results and discussion

The work consists of two parts. Part one is to assess the performance of the numerical approach. In part two, a parametric study is conducted to investigate the impacts of the droplet size and the volume fraction. The model is used for a bend geometry design based on the numerical results of droplet deposition and pressure drop by changing the curvature ratios of a bend.

Table 3.1: Boundary conditions used in all simulations

	velocity inlet [m/s]	Fully developed profiles		
Inlet	turbulent intensity [%]	Fully developed profiles		
	turbulent viscosity ratio	Fully developed profiles		
Outlet	pressure outlet [Pa]	P _{static} =0		
Wall	no-slip boundary [m/s]	u _{wall} =0		

3.5.1 Model assessment

Empirical studies show that air-water flows passing a bend not only create complex flow patterns, such as secondary flow and film inversion but also cause a large pressure drop. The mixture model was checked qualitatively to see whether or not the model is capable of capturing the complex flow patterns and film formation. Moreover, to investigate its accuracy, the model was tested quantitatively by comparing the numerical results of the pressure loss with the empirical models from literature.

(a) Flow patterns and liquid film modeling

Fig. 3.1 shows the numerical results of an air-water flow passing through a vertical 180° bend (U-bend) with the diameter equal to 0.0508m and the curvature ratio δ equal to δ . The flow is in the turbulent region with Re= 1.25×10^{5} and with the volume fraction for the water phase α =0.06. The droplet size for this case is $30\mu m$. The liquid distribution (expressed by the volume fraction for the water phase) and the streamline of the continuous phase are shown at the middle plane. Furthermore, the liquid distribution and the streamlines for the gas and the liquid phase ("G" and "L" for short) are shown along the bend at the cross sections of 0° , 45° , 90° , 135° , 180° deflections and the location at downstream 2d from the bend exit.

The plots show that the streamlines for both phases exhibit very similar patterns at the cross section of 0° deflection and the location at downstream 2d which is reasonable since at those locations flows are only under the gravity field. Around the bend, the results show that the air phase and the water phase have different behavior. Due to the centrifugal force, the air streamline and the water streamline present a secondary flow pattern at the cross section of 45° deflection. Meanwhile, the streamlines ended at the wall illustrate that the disperse phase tends to deposit and start to accumulate to form a liquid film on the outer bend wall. Further downstream in the bend, while simple streamlines of the water phase show that the droplets are traveling from the inner bend to the outer bend due to the centrifugal force, the streamline for the air phase exhibit more complex patterns due to the interaction between the phases. With respect to the liquid film, it can be seen from the diagram that the structure presents a stratified feature along the outer bend. This statement is consistent with the observation of Hoang and Davis (1984).

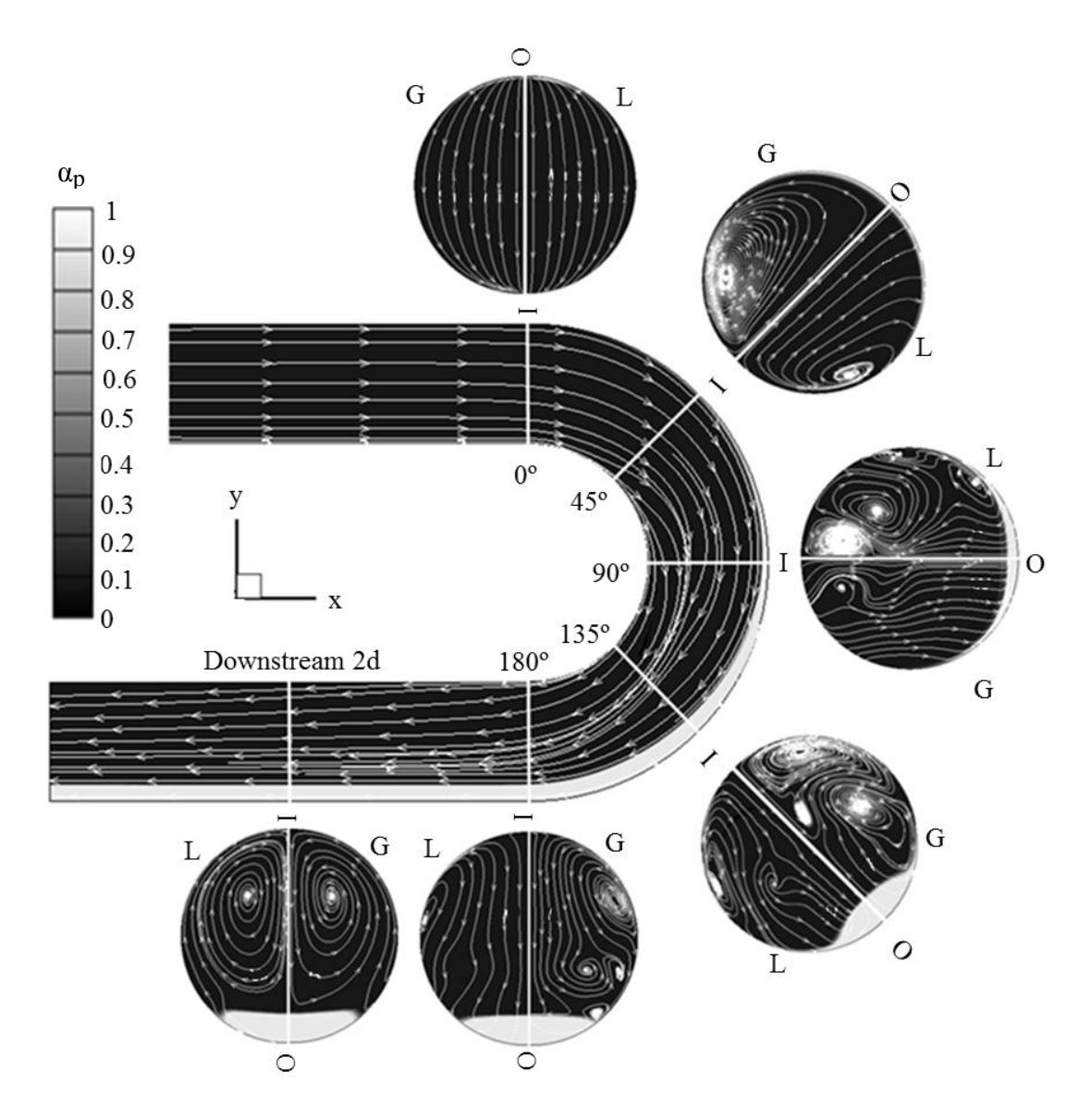


Figure 3.1: The air and water streamlines show the development of the flow patterns and the interaction between two phases. The contour of α_p shows the liquid film formation along the 180° bend. "G" and "L" denotes gas and liquid, respective.

(b) Film inversion

In most situations of a horizontal bend, a liquid film forms on the pipe wall and travels along the outer bends due to the centrifugal force. Under certain flow condition, however, liquid film can travel along the inner bends regardless of existence of the centrifugal force. This extraordinary phenomenon is referred as "film inversion" and was observed in a helical pipe by Banerjee et al. in 1967. They stated that film inversion only occurs at low liquid but high gas flow rates in a horizontal bend. Hart et al. (1988) derived a criterion for this phenomenon based on the static equilibrium of moment, given as

$$\dot{m}_{f} / \dot{m}_{p} > 195(\rho_{f} / \rho_{p})^{1/2} (\mu_{f} / \mu_{p})^{3/4}$$
 (3.19)

where \dot{m}_f , \dot{m}_p are the air and the liquid mass flow rate; ρ_f , ρ_p denote the gas and liquid density; μ_f , μ_p indicate the air and the liquid dynamic viscosity. The ratio of the air mass flow rate and the liquid mass flow rate is the function of their density and the volume fraction, obtained

$$\frac{\dot{\mathbf{m}}_{\mathbf{f}}}{\dot{\mathbf{m}}_{\mathbf{p}}} = \frac{\rho_{\mathbf{f}} (1 - \alpha_{\mathbf{p}})}{\rho_{\mathbf{f}} \alpha_{\mathbf{p}}} \tag{3.20}$$

Eq. (3.19) and Eq. (3.20) are solved to obtain the following criterion for an air-water flow $\alpha_{_{D}} < 0.0037 \tag{3.21}$

To verify the models, the case is run for a mist flow with α_p =0.003 passing through a horizontal U-bend with d=0.0508m and δ =30. The gravity is in a negative z direction. The flow is in the turbulent region with Re=16800. The droplet size uses the Sauter mean diameter d_{32} =149 μ m. This is solved by Eq. (3.22) (Azzopardi 1985)

$$\frac{d_{32}}{\lambda} = \frac{15.4}{We^{0.58}} + 3.5 \frac{G_{LE}}{\rho_p U_f}$$
 (3.22)

where $\lambda = \sqrt{\sigma/\rho_p g}$ is a length scale; We = $\rho_p U_f^2 \lambda/\sigma$ is a Weber number; $G_{LE} = \rho_p U_p$ is the entrained liquid mass flux; the surface tension σ for air and water is equal to 0.072; the inlet air velocity U_f and the inlet water velocity U_p are 25m/s and 0.075m/s.

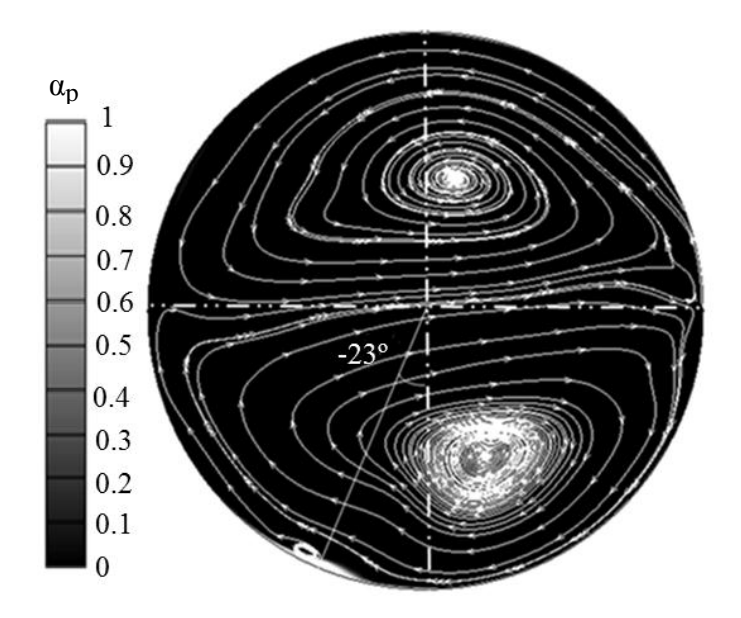


Figure 3.2: Water film forms at the inner bend wall affected by the secondary flow pattern.

Fig. 3.2 shows the numerical result of the film location at the outlet cross-section of the U-bend. The gravity is in a minus z direction. It can be seen that the film locates at -23° from the vertical centerline which indicates film inversion occurs and the model is able to capture the phenomenon. The liquid film is thin due to the low water flow rate. The secondary flow patterns are not symmetric to the horizontal axis due to the gravity. The film inversion is enhanced by this secondary flow which transfers the liquid film from the outer wall to the inner wall. In addition, a small vortex is generated due to the liquid film. From Fig. 3.3, more detail is covered for the volume fraction distribution of the water phase at the pipe wall for the same cross section. The

volume fractions are almost the same around the outer bend except -270° where it is as low as 0.05. This may be caused by the secondary flow of the air phase due to the centrifugal force. In addition, liquid film is observed at the inner bend between 0° and -30° where the volume fraction is equal to unit which indicates that film inversion occurs.

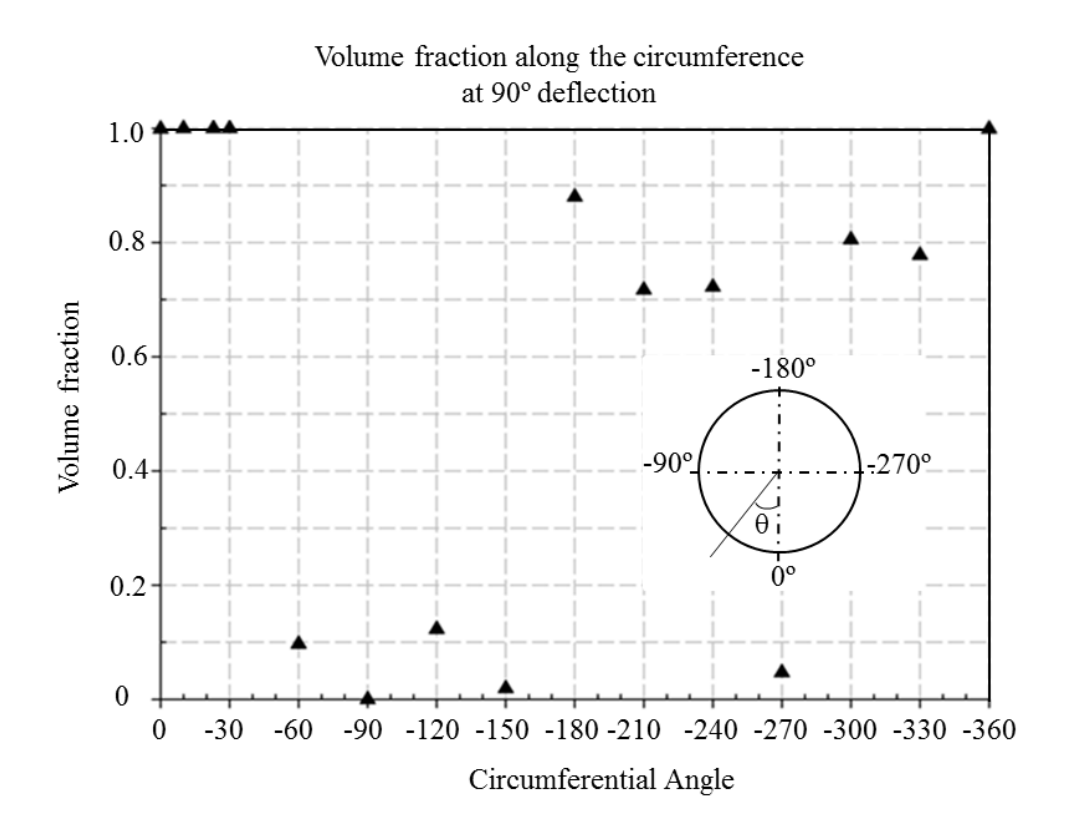


Figure 3.3: Volume fraction distribution of the water phase shows the location of liquid film at the pipe wall of the outlet cross section.

(c) Pressure drop prediction

Much work has been done on measuring the pressure loss of turbulent gas/liquid flow in horizontal 90° bends since 1960s (Fitzsimmons 1964, Sookprasong 1980, Norstebo 1986, Mandal and Das 2001, etc.). Based on the experimental data, different empirical models were

developed to predict the pressure drop of two-phase flows. Lockhart and Martinelli (1949) computed the pressure loss of a gas/liquid flow by using a multiplier concept. This method has been wildly used in developing empirical models by many authors (Chisholm 1971, Sookprasoog 1980 and Paliwoda 1991). An alternative proposed by Mandal and Das (2001) is the friction factor method based on the Fanning friction factor equation. A detail review on empirical models of pressure drop was given by Azzi et al. (2000).

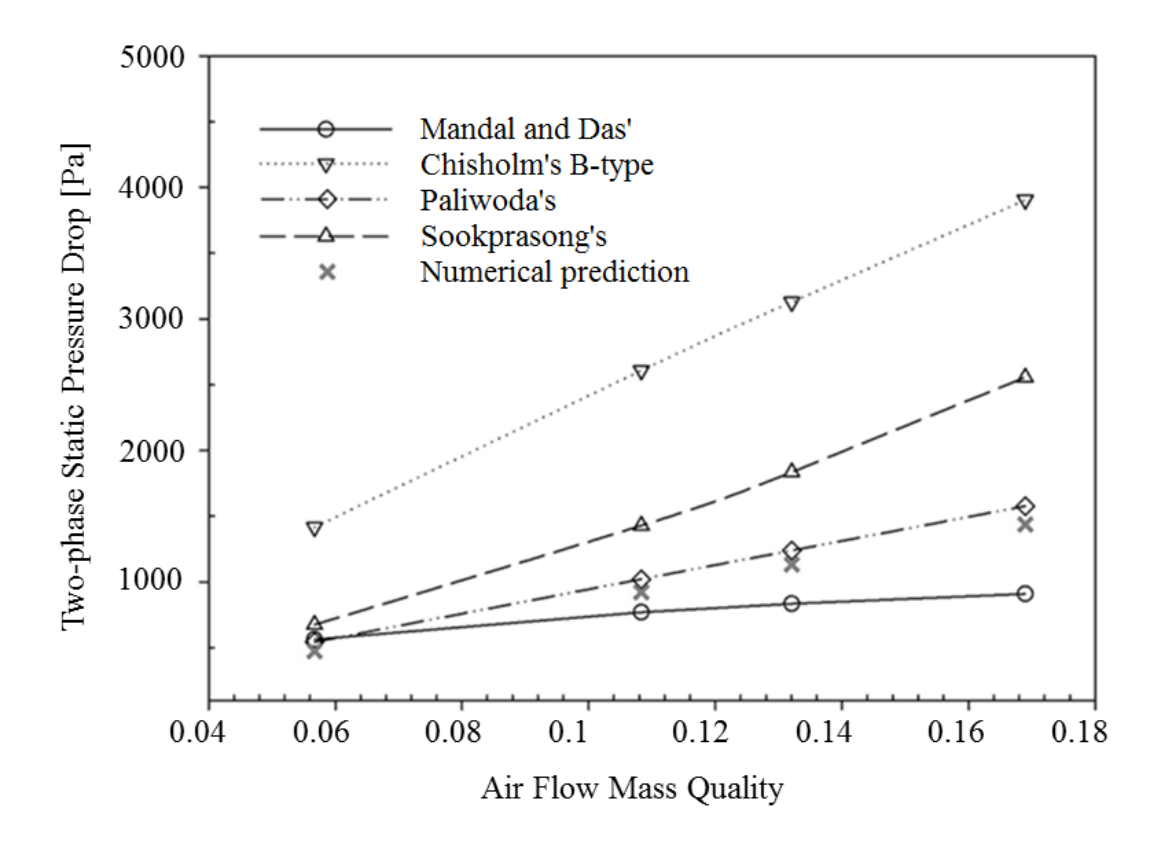


Figure 3.4: Comparison shows good agreement of the numerical results with the Paliwoda's empirical model

Simulations are run for a mist flow passing through a horizontal 90 ° bend with d=0.0508 and δ =5. The air mass quality is from 0.056 to 0.16. Numerical results of the pressure drop between

the entrance and the exit of the bend are compared to different empirical models from literature and shown in Fig. 3.4. The plot shows that the numerical results agree with Paliwoda's empirical model very well. It can be also seen that Chisholm's B-type predicts a very high pressure drop compared to other empirical models. This deviation is consistent with Norstebo's observation. He obtained a 110%+ discrepancy when he compared his experimental data with the Chisholm's method which indicates that Chisholm's empirical model may overpredict the pressure drop. Another observation of the plot is that the deviation of the pressure drop predicted by other empirical models is getting greater when the air flow mass quality is increased. Since deviation of the pressure drop predicted by different empirical models is large, it is uncertain whether the mixture model is accurate. But it can be concluded that the model predicts results in a reasonable range.

3.5.2 Applications

The test cases for parametric studies are summarized in Table 3.2. Case 1 and case 2 are to investigate the effect of the droplet sizes and the volume fraction of the water phase on the flow patterns, droplet deposition and pressure drop. A 90 ° bend with the pipe diameter d=0.0508m and with the curvature ratio δ =5 is used. In addition, a single-phase air flow with the same Re

Table 3.2: Summary of the parameters used in the test cases

Test cases	Case 1	Case 2	Case 3	Case 4
Droplet size, d _p [μm]	1~50	30	30	30
Volume fraction, $\alpha_p[\%]$	6	3~15	6	6
$Re(\times 10^5)$	1.25	1.1~2.3	1.25	1.25
Bend angle, θ []	90	90	180	90,180
Incline angle, β [°]	90	90	0~90	0
Curvature ratio, δ	5	5	5	1.5~9.0

number is modeled in the same bend geometry. The results are compared those from air-water flows. In Case 3, the effect of the incline angle on the pressure as well as the deposition efficiency is investigated. In case 4, the mixture model is used for optimizing the bend geometry for low pressure drop as well as high droplet deposition efficiency in a horizontal bend by changing the curvature ratio.

(a) Parametric studies

Fig. 3.5 shows the comparison between the air flow and the air-water flows for the streamlines of the continuous phase at the exit of a vertical 90 ° bend. The droplet sizes are changed from 1μm to 50μm. The volume fraction equal to 6% is used for all droplet sizes. For droplets as small as 1μm (Fig. 3.5c), the secondary flow streamline looks similar to the single-phase flow (Fig. 3.5b), which indicates that droplets with a small size like this have a marginally effect on the continuous flow. However, with the increase of the droplet size, the effect of the water phase becomes significant. Fig. 3.5e shows that the secondary flow of the continuous phase is reversed by the disperse phase and rotates clockwise. With a larger droplet size, more complex patterns like multi-pair secondary flows occur (Fig. 3.5f).

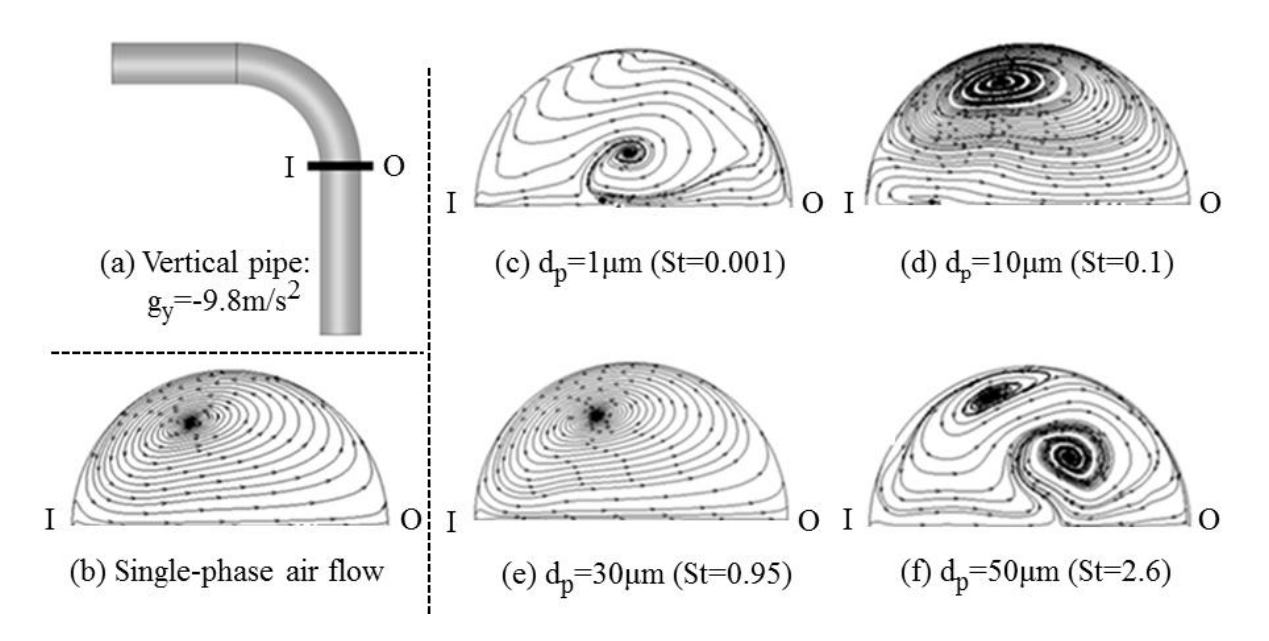


Figure 3.5: Comparison between the single-phase air flow (b) and the air-water flows (c-f) on the secondary flow patterns at the cross section of 90 ° deflection (a) changing with different droplet size

The different effects of the droplet size are attributed to the droplet behavior and can be studied using the St number. The definition of this dimensionless number and how it affects the particle behavior have been discussed in Chapter 2. Fig. 3.6 shows the volume fraction distribution of the water phase at the bend exit. Here we assume that a liquid film is formed when $\alpha_p \ge 0.8$. It can be seen from Fig. 3.6a that for a small St number the droplets follow the air flow closely and no separation between the phases occurs. A small St number means the disperse phase responds to the continuous phase quickly which results in a homogenous type of flow. For St=0.027, droplets start moving from the inner bend to the outer bend which indicates separation between two phases occurs (Fig. 3.6b). With a larger St number, droplets deposit on the wall and accumulate to form a liquid film. This film becomes thicker with more droplets deposited on the wall (Fig. 3.6c-f). Finally, droplets with large enough St number will all deposit on the wall to

thicken the liquid film (Fig. 3.6e). From the above discussion, it is found that the conclusion made for a dilute flow on the effect of the St number on the particle behavior is still valid for dilute flows with a large mass loading.

Plots from Fig. 3.7 show that the continuous secondary flow patterns vary with the increase of α_p at the bend exit. A single size equal to 30 μ m is used for the droplets. It can be seen that the streamlines of the secondary flow patterns at the cross section are resemblant, which indicates that the volume fraction of water phase has marginally effect on the flow patterns and the flow intensity.

As regards the pressure drop, Fig. 3.8 shows the comparison of the pressure drop caused by the bend component between the air flow and the air/liquid flow. The pressure drop in the air flow is labeled with a circle. One can observe that the pressure drop in the air-water flow is much greater than that in the air flow. This observation is consistent with Hoang and Davis' statement (1984). From Fig. 3.8a, it is shown that the pressure drop is increased with the increase of the droplet size. It then decreases for droplets larger than 12µm because more droplets escape from the core flow and deposit on the bend wall. For droplets greater than 40µm, the pressure drop tends to be stable since those cases have the same situation where almost all the droplets deposit on the pipe wall. In Fig. 3.8b, nevertheless, it can be seen that the pressure drop is simply proportional to the volume fraction of the water phase.

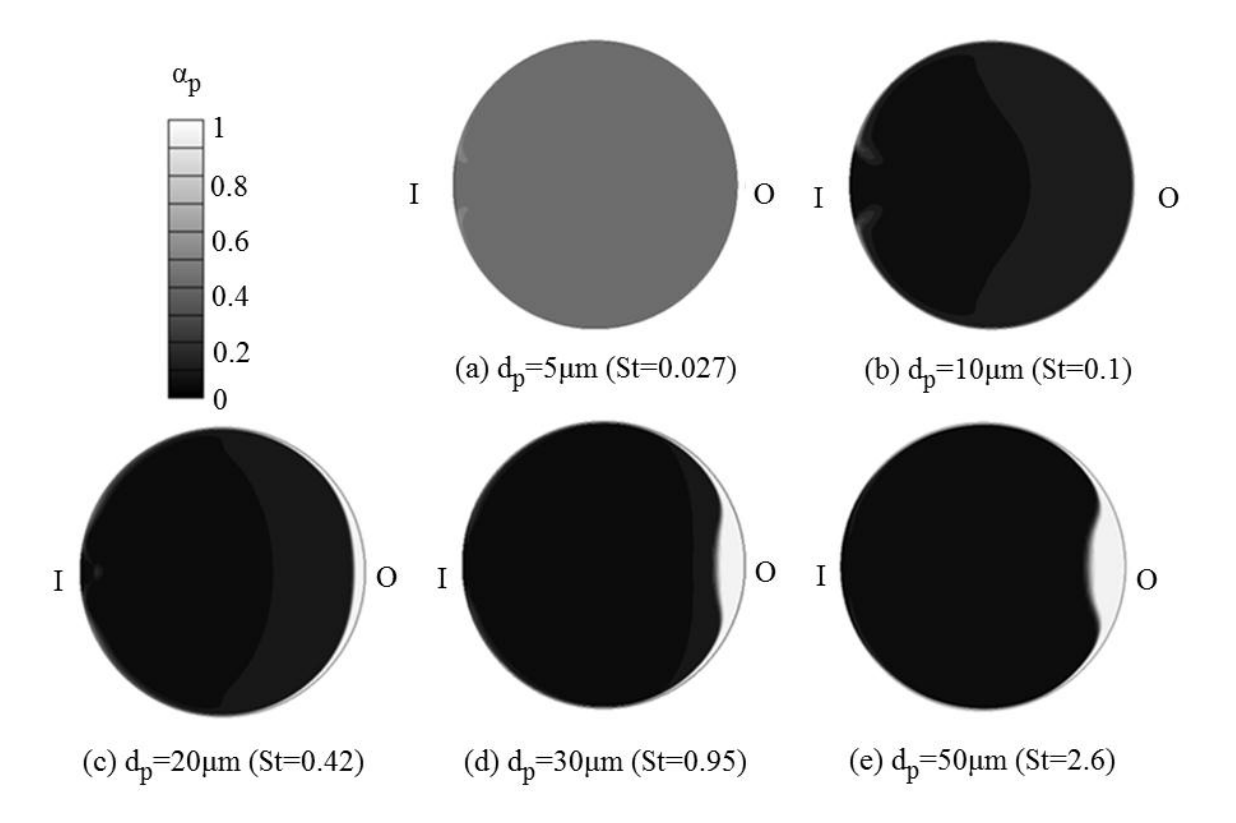


Figure 3.6: Volume fraction distribution shows the liquid film location at the cross section of 90 $^{\circ}$ deflection changing with different droplet size

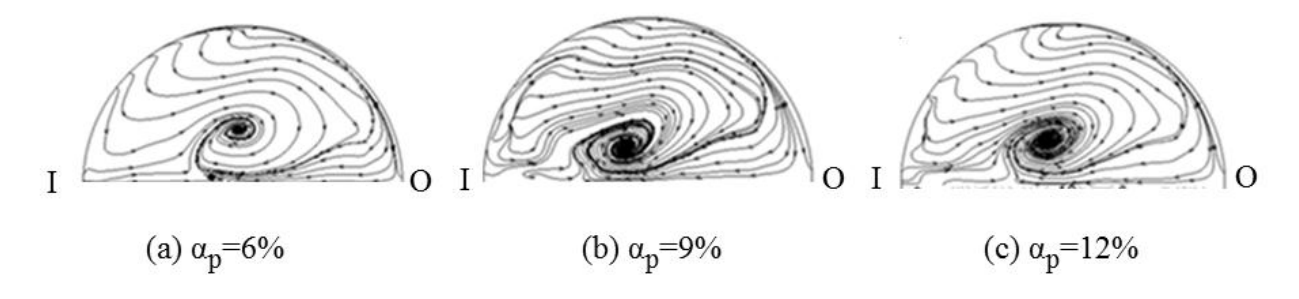


Figure 3.7: Secondary flow patterns and flow intensity at the cross section of 90 $^{\circ}$ deflection for flow with a different α_p

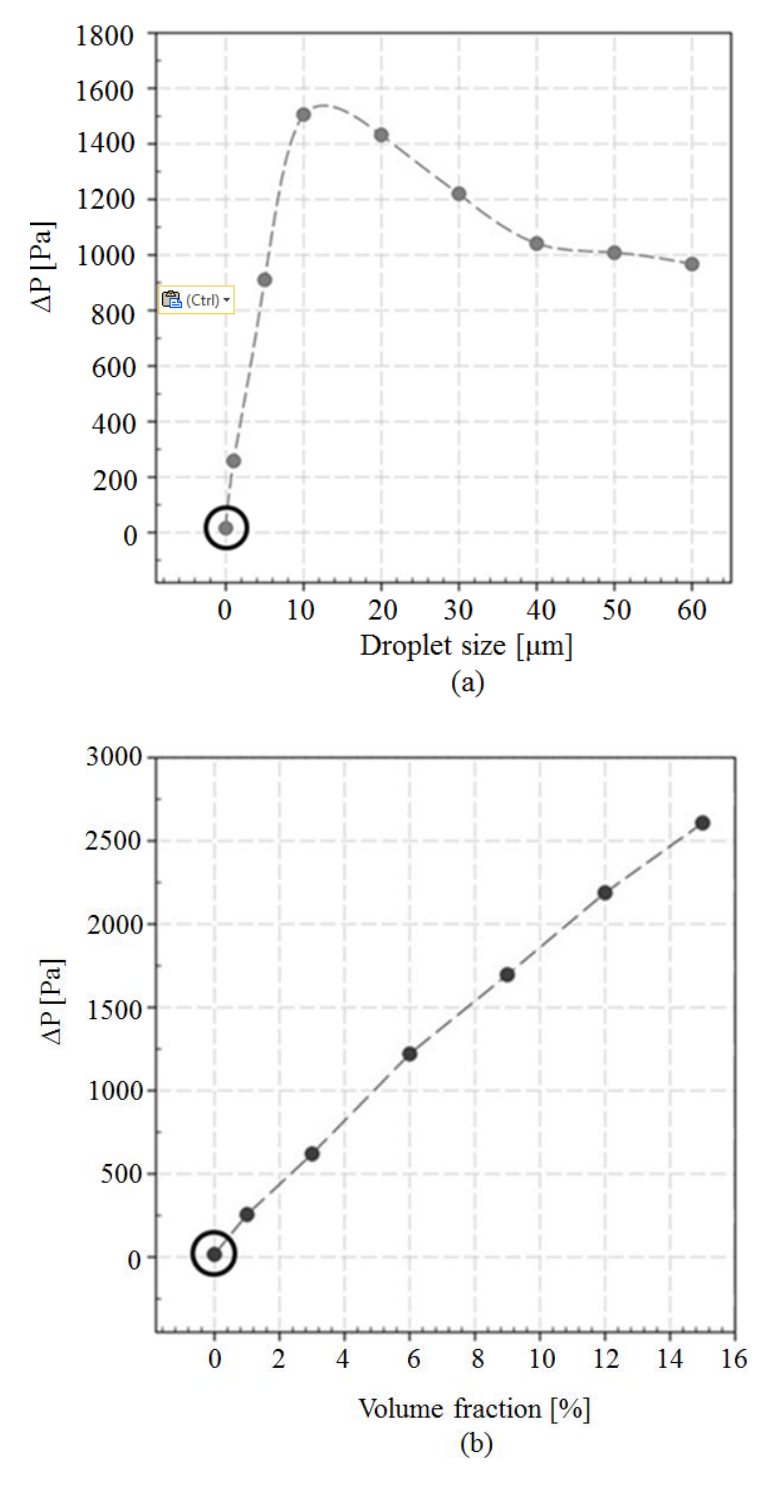


Figure 3.8: Pressure drop of the bend section changing with (a) the droplet size, (b) volume fraction of the water phase

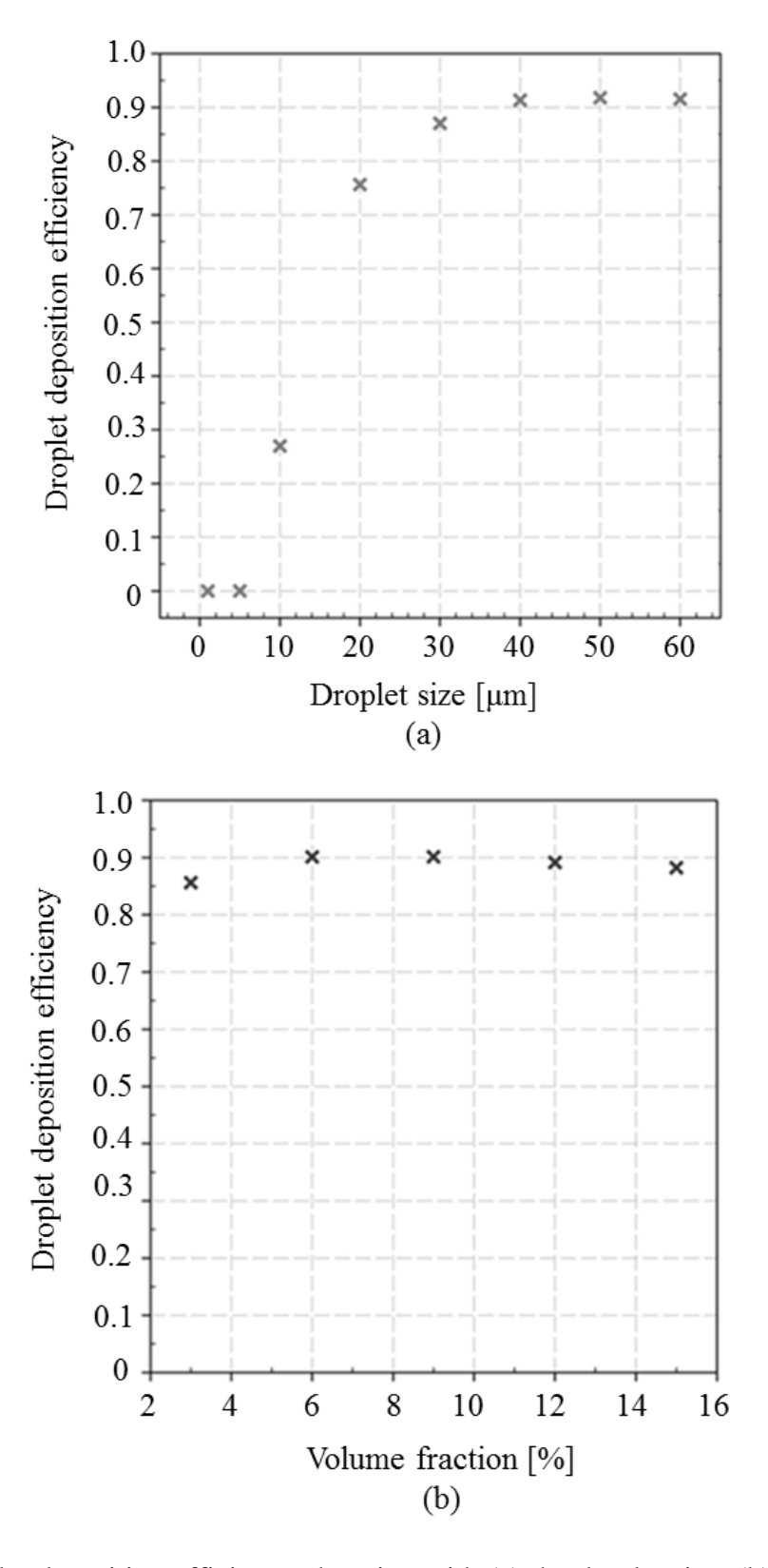


Figure 3.9: Droplet deposition efficiency changing with (a) the droplet size, (b) volume fraction of the water phase

The droplet deposition efficiency is defined as the ratio of the mass flow rate for the liquid film to the total mass flow rate for the liquid at the bend exit. Fig. 3.9 shows the tendency of the droplet deposition efficiency changes with the increase of the droplet size and the volume fraction of the water phase, respectively. It can be seen from Fig. 3.9a that no deposition efficiency is obtained for the droplet size less than 5 μ m due to a small St number. For droplets larger than 5 μ m, the droplet deposition efficiency is proportional to the droplet size. The deposition efficiency reaches 0.92 and becomes stable when droplets are larger than 40 μ m. This can be treated as the maximal deposition efficiency that this bend geometry can obtain. With regards to the influence of α_p , Fig. 3.9b shows that α_p only has a marginal effect on deposition efficiency.

(b) Incline angles

The effect of the incline angle on the pressure drop and the deposition efficiency is investigated. Fig. 3.10 demonstrates a U-bend changing its incline angle β from 0° (horizontal) to 90° (vertical) with an increment 15°. Comparison of the pressure drop and droplet deposition efficiency is shown in Table 3.3. Result shows that the bend incline angle does not affect the pressure drop and the droplet deposition efficiency.

Table 3.3: Pressure drop and deposition efficiency in a U-bend with different incline angles

Angle β[°]	0	15	30	45	60	75	90
η [%]	89.6	89.8	90.0	90.1	90.2	90.1	90.2
ΔP [Pa]	1196	1194	1194	1196	1200	1205	1200

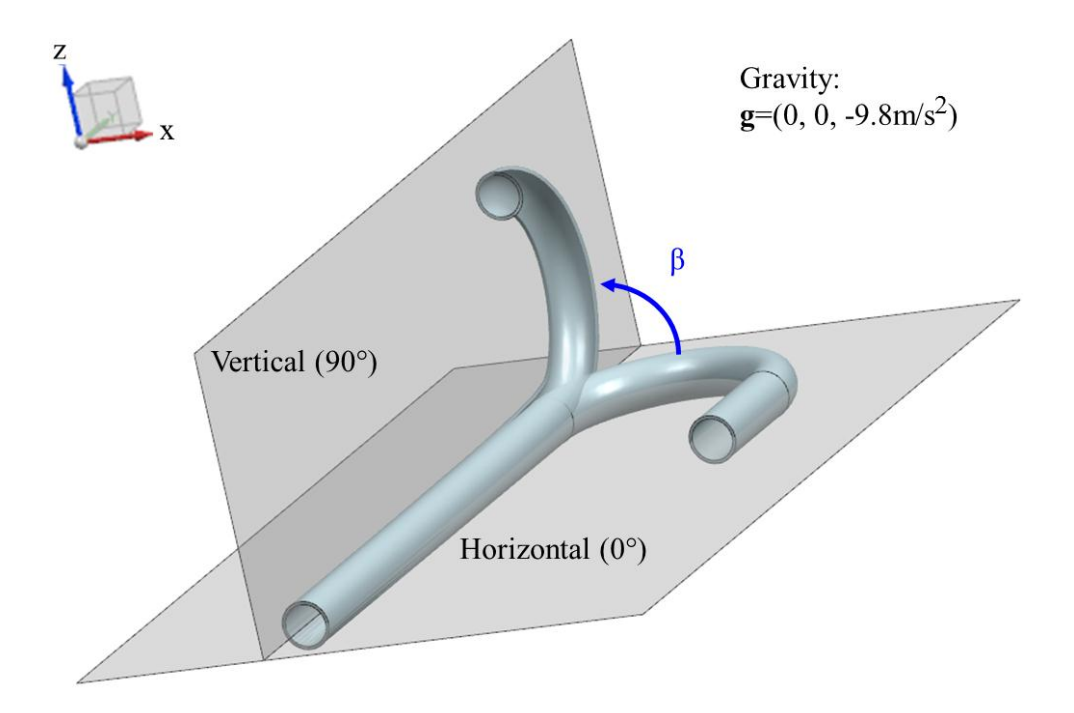


Figure 3.10: Schematic of a U-bend changing from horizontal position to vertical position with an increment of 15°. For interpretation of the references to color in this and all other figures, the reader is referred to the electronic version of this dissertation.

(c) Bend optimization

Since the pressure drop is simply proportional to α_p and the droplet deposition efficiency is not affected by α_p . A moderate droplet size with a single volume fraction can be chosen for a bend geometry optimization based on the pressure drop and the deposition efficiency. The word "moderate" here means the droplets have to be large enough to allow the occurrence of separation between the phases but not too large so that not all the droplets deposit on the bend wall regardless of the geometry of bends. In industrial transportation, a large range of droplet sizes would exist in gas/liquid mist flow. The idea is that if we can obtain a geometric configuration to improve the deposition efficiency by using a moderate size, the configuration

could be employed to improve the deposition efficiency for practical applications. In this work, 30µm is chosen as the droplet size with the volume fraction equal to 6%.

Fig. 3.11 shows the bend pressure drop and the droplet deposition efficiency changed due to the varying curvature ratio of a 90° bend and a 180° bend with the same pipe diameter equal to 0.0508m at the horizontal plane. Results show that the tendency looks similar for both bends. It can be seen from the plots that a tight bend causes extremely high pressure drop and low droplet deposition efficiency. This extraordinarily high pressure drop is caused partially due to flow detachment. Secondly, it is because the flow is "chocked" by a recirculation flow formed after the tight bend due to the extremely sharp curvature streamline. On the other hand, the low deposition efficiency is due to the short experience of centrifugal force and film entrainment. At the same curvature ratio, pressure drop and deposition efficiency in a 180° bend is higher than those in a 90 °bend. The pressure drop is decreased with the increase of the curvature ratio at the beginning as a sharp curvature streamline can cause flow detachment and lead to a high pressure drop. With a higher curvature ratio (e.g. $\delta \geq 7$), however, the pressure drop smoothly increases with the increase of the curvature ratio. The effect of the residence time at this curvature ratio becomes more important than that of the curvature streamline as more wall friction can be expected due to a longer residence time for the flow to stay in a bend. On the other hand, the droplet deposition efficiency is proportional to the curvature ratio at the beginning and becomes flat or increases slowly after the curvature ratio is larger than 5 and 7 for the 90 $^{\circ}$ bend and 180 $^{\circ}$

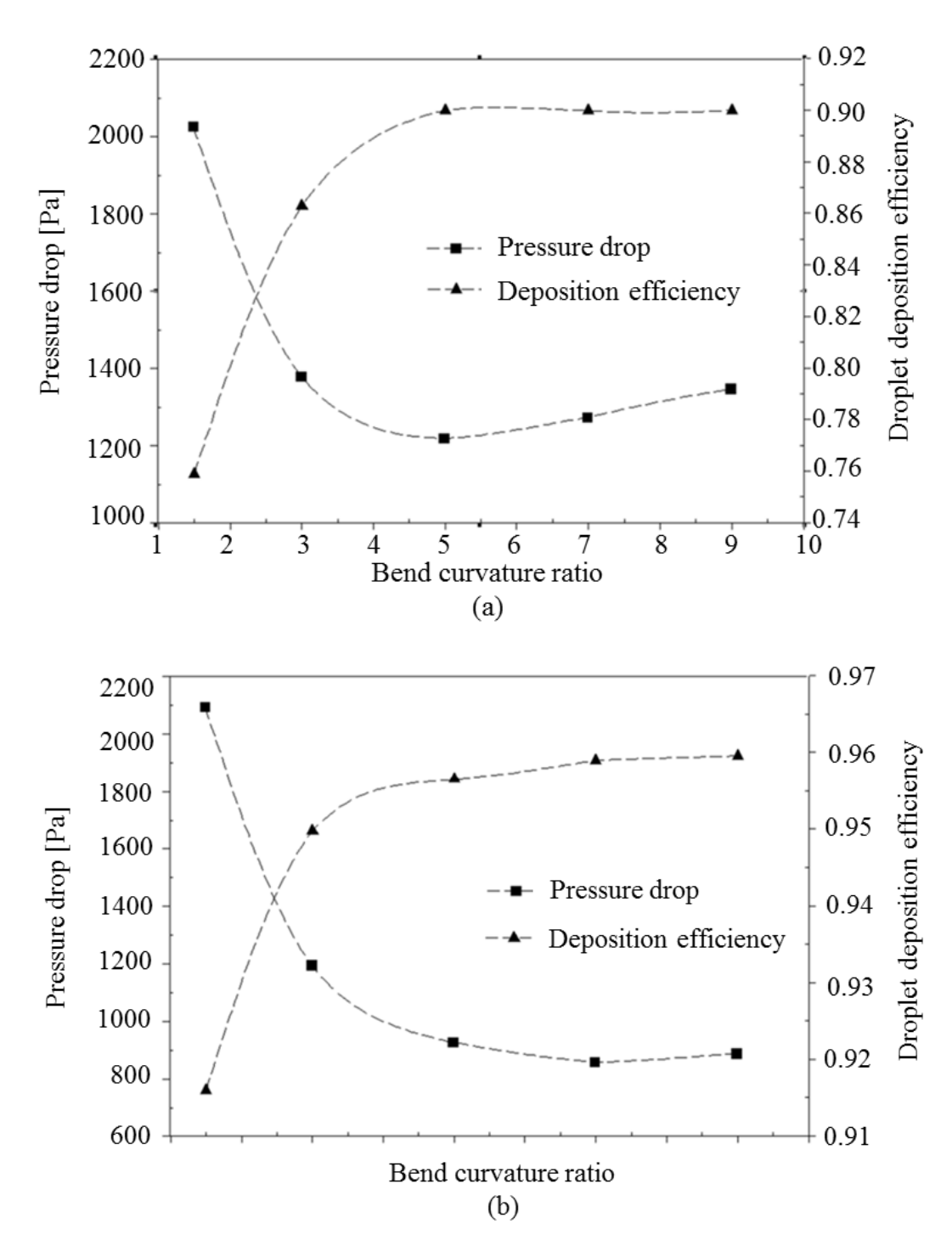


Figure 3.10: Tendency of bend pressure drop and droplet deposition efficiency in a horizontal 90 $^{\circ}$ bend and a 180 $^{\circ}$ bend shows the bend geometry is optimal at curvature ratio equal to 5 and 7, respectively.

bend, respectively. Therefore, it can be concluded that a bend with the curvature ratio equal to 5 and 7 is the optimal geometry respectively for the 90° bend and 180° bend to minimize the pressure drop as well as obtain relatively high droplet deposition efficiency.

3.6 Summary

Numerical simulations are performed using the commercial code ANSYS FLUENT to model turbulent mist air-water flows passing through circular 90° and 180° bends. The flow patterns, pressure drop and droplet deposition efficiency of the bend component are studied in this work. The simulations are performed using the mixture model closed by the modified Realizable k- ϵ model and using the enhanced wall treatment to solve the flow at the near-wall region.

It is observed that a two-way coupling mist flow is much more complicated than a one-way coupling flow. The drift flux model studied in this Chapter is proven to be capable of capturing the complex flow patterns observed experimentally. For example, secondary flows of the continuous phase are induced by the centrifugal force and impacted by the disperse phase. The liquid film formed by droplet deposition is usually stratified along the outer bend but the film can be inversed to the inner bend under certain conditions. In addition, the comparison between the numerical results and the empirical models shows the pressure drop estimated by the model agree well with Paliwoda's work. Results also show that the pressure drop and the droplet deposition efficiency are significantly affected by a bend. Based on these computations, bend geometry design was performed. It is found that 90° and 180° bends with the curvature ratios equal to 5 and 7 respectively can be used to achieve a minimal pressure drop as well as relatively high deposition efficiency regardless of the bend angles.

CHAPTER 4

SIMULATION OF FLUID-STRUCTURE INTERACTION USING AN ELASTIC FORCING METHOD BASED ON AN IMMERSED BOUNDARY METHOD

In this Chapter, a numerical technique called the immersed boundary (IB) method is discussed and modified for the simulation of a solid structure immersed in a fluid flow. The purpose of this technique is to tackle the fluid-structure interaction and use a simple Cartesian rectangular mesh to solve the fluid flow.

4.1 Introduction

Fluid-structure interactions are commonplace in biological systems and industrial applications. Examples include blood flow in hearts, red blood cells in arteries, aquatic animal locomotion, and vehicles or aircrafts in turbulent air flows. The numerical simulation of a fluid interacting with a structure is a very challenging problem. Consider a structure immersed in a fluid flow shown as in Fig. 4.1a. Conventional approaches of Direct Numerical Simulation (DNS) of fluid-structure interaction use a body-fitted mesh. The grid is first constructed on the object surface ∂S and extended to the fluid flow Ω_f . There is no grid located inside the structure. This method allows to easily imposing the no-slip boundary condition on the surface of the immersed structures. However, if the structure is complex in geometry, deformable, and movable in the flow, an adaptive mesh is inevitable. This requires an intense computational effort and frequent human input as the flow is matching with time.

To avoid using an adaptive mesh, an alternative approach called immersed boundary (IB) method can be used. The method considers the impact of the immersed structure in a force density term of the fluid equation and solves the equation for the entire domain using a Cartesian

rectangular mesh. In general, the structure surface does not coincide with the Cartesian mesh (Fig. 4.1b). Nevertheless, communication of variables, such as velocity and force density between the Cartesian mesh and the structure surface could be achieved by using an interpolation or an extrapolation process. The focus at this moment is on how the force density term is obtained. Numerical approaches used for rigid structure simulation in literature can be classified into two categories: virtual boundary methods (Peskin 1972, Goldstein et al. 1993) and fictitious domain methods (Mohd-Yusof 1997, Fadlun et al. 2000, Kim et al. 2001, and Uhlmann 2005). A virtual boundary method uses a set of discrete points to mark the structure surface and evaluate the force at those points. The points are treated as virtual points existing in the flow domain. The points representing the structure surface can be tracked and moved. The virtual boundary method was first proposed by Peskin in 1972 to study a blood flow interacting with heart valves. By assuming that the structure surface is an elastic boundary, the Lagrangian points are linked with springs. The springs are dampened or stretched by the Lagragian points moving with the surrounding flow. The force exerted on the points is then a function of the spring deformation and its stiffness coefficient. This method is also referred to as the elastic forcing method. Goldstein et al. (1993) used the similar idea for a stationary rigid structure by applying large stiffness coefficients. However, Lee (2003) stated that a large stiffness coefficient may cause numerical instability if the time step used is larger than the characteristic time scales of the spring oscillation. Instead of evaluating the force on the Lagrangian points with an elastic boundary assumption, Mohd-Yusof (1997) obtained the force density term from the momentum equations by imposing a desired velocity at the points wherever the surface is intersected with the Eulerian mesh via a B-Spine function. This approach was referred to as a fictitious domain method. Fadlun et al. (2000) applied the method to flow interaction with complex geometries.

The desired velocity on the boundary was obtained via volume fraction weighing or a linear interpolation. The method was proved to be able to overcome the drawback of an elastic forcing method on time step restriction. Kim et al. (2001) improved the approximation scheme for stability and accuracy by using a second-order-accurate interpolation scheme. However, force oscillations occur at the boundary when the above methods were used to move the structure boundaries. Uhlmann (2003) stated that force oscillations are not appropriate for particulate flow simulation. Later, Uhlmann (2005) improved the stability of the direct forcing method by combining the Dirac delta function of Peskin (1972) to smooth the force on the boundary of a rigid body.

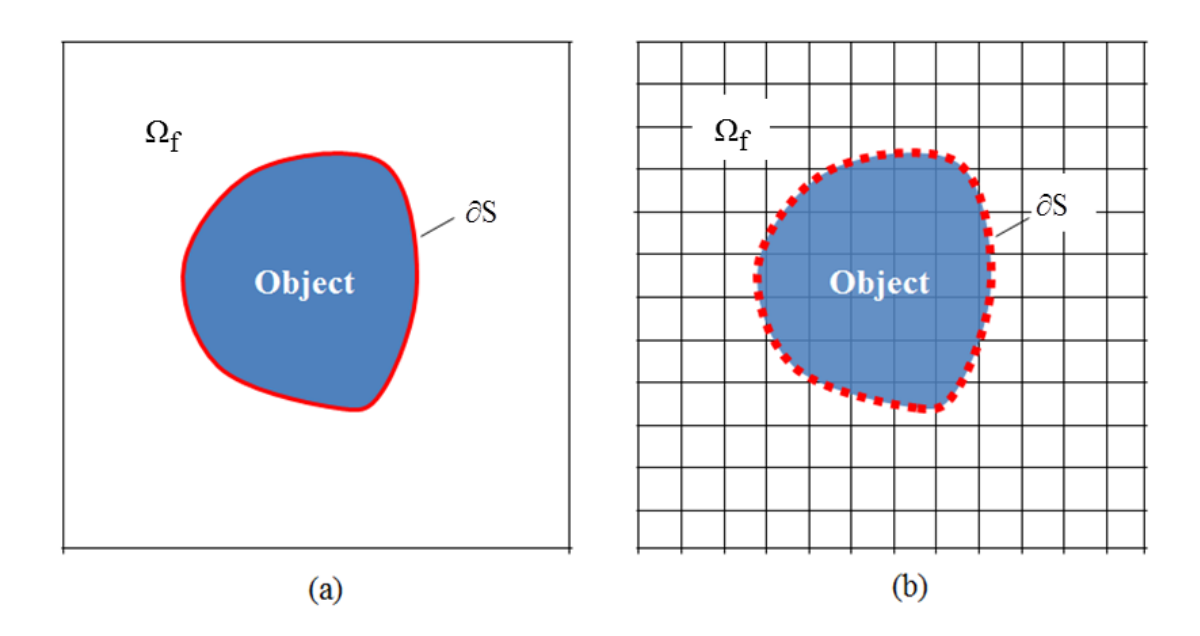


Figure 4.1: Schematic configuration shows a Eulerian mesh for the fluid domain Ω_f and a Lagrangian mesh around the fluid-object interface ∂S .

By treating the impact of the immersed boundary in a force density term of the fluid equations, the IB method possesses great flexibility and is compatible with most of the numerical schemes. Recently, it becomes popular to combine the technique with the lattice Boltzmann method. The lattice Boltzmann method is proved to be simple, algebraic, and intrinsically parallelized (Wu and Shu 2010). Fogelson and Peskin (1988) implemented the IB method based on a spectral method for rigid particle simulation in a Stokes flow. Glowinski et al. (1999) combined the IB method with a Finite Element Method for particle sedimentation. The IB method based on a finite volume method was used by Sharma and Patankar (2000) for rigid particulate flows. In this work, a finite different method is used. It is very common that the incompressible N-S equation is used with the IB method in dealing with fluid-structure interaction (Lai and Peskin 2000, Höfler and Schwarzer 2000, Fadlun et al. 2000, Uhlmann 2005). However, solving the incompressible N-S equation usually ends up with finding a solution to a system of equations or the Poisson equation. The elliptic behavior of the Poisson equation needs the equations to be solved for the whole domain simultaneously through an iteration process. This requires a large computational effort each time step. Although the overall computational effort could be reduced by using a large time step, a large time step is not suitable for research on fluid-structure interaction. Structure moving with a large time step would lead to information missing and thus cause inaccuracy in predicting its trajectory. In this work, in order to improve the computational efficiency, compressible N-S equation is solved by using an explicit MacCormack scheme (MacCormack 1969). The MacCormack scheme with a second-order accuracy in space and time has been widely applied to compressible flows as well as incompressible flows due to the advantages of easy implementation and friendly parallelizing computation. However, literature

on using the IB method based on the MacCormack scheme for fluid-structure interaction simulation cannot be found.

In this chapter, an algorithm is developed for combining the MacCormack scheme with the IB method and used for fluid-structure interaction. The equations are discretized in time and space. The performance of the numerical approach on simulating fixed and movable rigid structure is investigated. The numerical approach is tested in the following 2-D cases (1) pressure driven flow, (2) uniform flow passing a stationary cylinder, and (3) settling rigid body impinging on a wall.

4.2 The MacCormack/IB method

To implement the IB method based on the MacCormack scheme, we consider the impact of the immersed structure to its surrounding flow in a force density term f of the compressible N-S equation. For a 2-D case, the equations for the MacCormack/IB method are given as

$$\frac{\partial \mathbf{U}}{\partial t} + \frac{\partial \mathbf{E}}{\partial x} + \frac{\partial \mathbf{F}}{\partial y} = \mathbf{f} \tag{4.1}$$

$$\mathbf{f}(\mathbf{x},t) = \int \mathbf{F}_{\mathbf{f}}(\mathbf{X},t) \delta_{\mathbf{h}}(\mathbf{x} - \mathbf{X}(\mathbf{s},t)) d\mathbf{s}$$
(4.2)

$$\frac{\partial \mathbf{X}(\mathbf{s}, t)}{\partial t} = \mathbf{U}(\mathbf{X}(\mathbf{s}, t), t)
= \int \mathbf{u}(\mathbf{x}, t) \delta_{h}(\mathbf{x} - \mathbf{X}(\mathbf{s}, t)) d\mathbf{x}$$
(4.3)

where U, E, and F are in a vector form, given as

$$\mathbf{G} = \begin{bmatrix} \rho \\ \rho \mathbf{u} \\ \rho \mathbf{v} \end{bmatrix} \tag{4.4}$$

$$\mathbf{E} = \begin{bmatrix} \rho \mathbf{u} \\ \rho \mathbf{u}^2 + \mathbf{p} - \tau_{xx} \\ \rho \mathbf{u} \mathbf{v} - \tau_{xy} \end{bmatrix}$$
 (4.5)

$$\mathbf{F} = \begin{bmatrix} \rho v \\ \rho u v - \tau_{xy} \\ \rho v^2 + p - \tau_{yy} \end{bmatrix}$$
(4.6)

$$\mathbf{f} = \begin{bmatrix} \mathbf{f}_{\mathbf{x}} \\ \mathbf{f}_{\mathbf{y}} \end{bmatrix} \tag{4.7}$$

The shear stress in the above vectors are given by

$$\tau_{xx} = \frac{2}{3}\mu \left(2\frac{\partial u}{\partial x} - \frac{\partial v}{\partial y} \right)
\tau_{yy} = \frac{2}{3}\mu \left(2\frac{\partial v}{\partial y} - \frac{\partial u}{\partial x} \right)
\tau_{xy} = \tau_{yx} = \mu \left(\frac{\partial u}{\partial y} + \frac{\partial v}{\partial x} \right)$$
(4.8)

The pressure p is related to the flow density through the equation of state

$$p = \rho c^2 \tag{4.9}$$

where c is the speed of sound in the media. For isothermal flow with a low Mach number $(Ma=||\mathbf{u}||/c)$: ratio of the flow speed and the sound speed), the flow can be approximated to be incompressible (Kundu and Cohen 2004). The explicit MacCormack scheme uses a predictor step and a corrector step to solve Eq. (4.1) (MacCormack 1969). The equation is discretized in time as follows

Predictor:

$$\mathbf{G}^* = \mathbf{G}^n - \Delta t \left(\frac{\partial \mathbf{E}^n}{\partial \mathbf{x}} + \frac{\partial \mathbf{F}^n}{\partial \mathbf{y}} \right) + \Delta t \mathbf{f}^n$$
(4.10)

Corrector:

$$\mathbf{G}^{n+1} = \frac{1}{2} \left[\mathbf{G}^{n} + \mathbf{G}^{*} - \Delta t \left(\frac{\partial \mathbf{E}^{*}}{\partial x} + \frac{\partial \mathbf{F}^{*}}{\partial y} \right) + \Delta t \mathbf{f}^{*} \right]$$
(4.11)

In the predictor step, the variables with * are preliminary results computed using the variables at the current time step n. In the corrector step, the variables at time step n+1 are obtained from the preliminary results. The detail of equation discretization is presented in Section 4.3.

One should notice that the force density term (f and f^*) in the above equations should be computed first before Eq. (4.10)-(4.11) can be solved. Eq. (4.2) converts the force density from the Lagrangian points $\mathbf{F_f}(\mathbf{X},t)$ to the Eulerian mesh $\mathbf{f}(\mathbf{x},t)$ through a Dirac delta distribution $\delta_h(\mathbf{x}-\mathbf{X}(\mathbf{s},t))$. When the velocity field is updated by solving the fluid equation (Eq. (4.1)), the second row of Eq. (4.3) is used to interpolate the velocity from the Eulerian mesh $\mathbf{u}(\mathbf{x},t)$ to the Lagrangian points $\mathbf{U}(\mathbf{X}(\mathbf{s},t))$ using the same Dirac delta function. The Lagrangian points representing the structure are then moved to a new location by using the first row of Eq. (4.3). The approach used to compute the force density on the Lagrangian points \mathbf{F}_f and the Dirac delta function δ_h used in this work are covered in the following sections.

4.2.1 Elastic forcing method

The elastic forcing method introduced by Peskin (1972) assumes that the structure surface marked by Lagrangian points is an elastic boundary. This can be accomplished by connecting the Lagrangian points with springs. Each spring possesses a stiffness coefficient and a length decided by the material property and the relative location of two Lagrangian points, respectively. The surrounding flow interacting with the structure could move the Lagrangian points, which

could lead to spring stretching or damping. Therefore, the force generated on the Lagrangian points is a function of the spring deformation and the material elasticity. The method has been proven to be well-suited in deformable structure applications. Examples are blood flows in a beating heart (Peskin 1972, Kovacs et al. 2001, McQueen and Peskin 2001, Vigmond et al 2003), blood cells transporting in arteries (Pacull 2006, Kim et al. 2009, Adib et al. 2010), and parachute dynamics (Kim and Peskin 2006, Kim and Peskin 2009, Miyoshi et al. 2009). In this work, the technique is employed to construct a rigid body based on a feed-back mechanism. Depending on whether a rigid structure is stationary or movable, the springs are constructed differently.

(a) Stationary rigid body

The elastic forcing method is quite handy in stationary rigid body modeling. According to Lai and Peskin (2000), each Lagrangian point on the structure surface is linked to its equilibrium location by a spring with a sufficiently large stiffness coefficient κ . All the springs obey the Hooks' law and the forcing on the k_{th} Lagrangian $F_k(t)$ is given as

$$\mathbf{F}_{k}(t) = -\kappa(\mathbf{X}_{k}(t) - \mathbf{X}_{k}^{e}) \tag{4.12}$$

Where $\mathbf{X}_k(t)$ is the location of the k_{th} Lagrangian point at time t; \mathbf{X}_k^e denotes the equilibrium location of the kth Lagrangian point. An equilibrium location is the initial location of a Lagrangian point ($\mathbf{X}_k^e = \mathbf{X}_k(t)\big|_{t=0}$). To enforce the boundary staying close to its equilibrium location, a large value for the stiffness coefficient κ of the springs is required. Since a Lagrangian point only links to its equilibrium point and the relative location to other Lagrangian point does not matter, this method can be applied to a stationary structure with a complicated boundary.

(b) Movable rigid body

Fogelson and Peskin (1988) applied the elastic forcing method to deal with rigid particle settling in a Stokes flow. Under the assumption that the structure surface is an elastic boundary, the rigid body is actually allowed to be slightly deformable. The springs are connected to resist deformation in the following manner: each Lagrangian point was linked to its adjacent points. An assistant point located at the center of the rigid body was linked to all Lagrangian points on the surface. A large stiffness coefficient is used so that the sprints can resist the deformation caused by the surrounding flow. In this work, instead of using the center point, we proposed a method to constructe a rigid body using a triangle structure. Triangle is a geometry known to be with a reliable support to a structure. Fig. 4.2 shows how the springs connect for a circle and an ellipse with k Lagrangian points. The blue circles are Lagrangian points used to represent the boundaries. Only a few Lagrangrian points are used in the diagrams for simplicity. To ensure using the Largrangian points only once for the triangle connection, the number of Lagrangian points is set to be divided exactly by 3. The red dash lines are springs for triangles. The blue dash lines are springs connecting the neighbor points. The stiffness coefficient for all the springs is sufficiently large to resist surface deformation.

Each spring linking to two Lagrangian points generates an opposite force with the same magnitude. For example, the force generated at point k due to the spring k-3 is computed from

$$\mathbf{F}_{k3}(t) = -\kappa(\Delta \mathbf{I}_{k-3}(t) - \mathbf{I}_{k-3}^{e})$$
(4.13)

where $\Delta l_{k-3}(t)$ is the length of spring k-3 in two perpendicular directions equal to $\|\mathbf{X}_k - \mathbf{X}_3\|$; \mathbf{l}_{k-3}^e is the reference length of spring k-3 in two perpendicular directions; κ is the spring stiffness which is sufficient large so that Δl_{k-3} will keep a length close to its reference length. The force

generated at point k is a combination of the forces contributed by spring k-1, k-3, k-6, and k-(k-1). This method can be extended to a 3-D case using triangular pyramids.

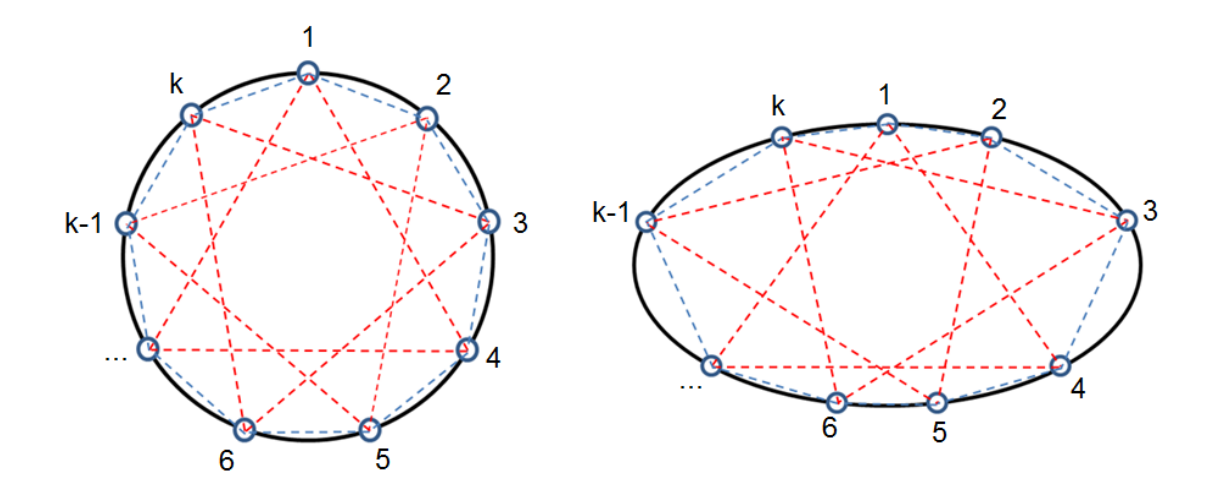


Figure 4.2: Schematic of spring construction for a movable rigid structure using a Lagrangian forcing method.

According to Forgelson and Peskin (1988), if a rigid body is under an external force, such as the gravitational, magnetic, and electrical force, the force acting on the rigid body can be forced directly on the Lagrangian points by using $\mathbf{F_f} = \mathbf{F_{int}} + \mathbf{F_{ext}}$, where $\mathbf{F_{int}}$ is the internal force due to the springs connecting to the Lagrangian points and $\mathbf{F_{ext}}$ is the external forces acting on the rigid body.

4.2.2 Construction of the Dirac delta function δ_h

The immersed boundary method involves two mesh systems, including a Eulerian mesh and a Lagrangian mesh. Shown in Fig. 4.3, the Lagrangian mesh is a set of discrete points used to track

the structure surface. Since the Lagrangian mesh does not concise with the Eulerian mesh, a distribution function is needed for information communication between two mesh systems.

Several distribution functions could be used in the past, such as a narrow Gaussian distribution (Goldstein et al. 1993), a discrete hat function (Saiki & Biringen 1996), and various versions of the Dirac direct function (Beyer & Leveque 1992, Lai & Peskin 2000, and Peskin 2002). In this work, a discrete Dirac delta function δ_h developed by Peskin (2002) is used. The expression of δ_h for a 2-D case is assumed to be

$$\delta_{h}(\mathbf{r}) = \frac{1}{h^2} \phi(\mathbf{r}_1) \phi(\mathbf{r}_2) \tag{4.14}$$

where $r_1 = \frac{x_1}{h}$; $r_2 = \frac{x_2}{h}$; x_1 and x_2 are two different space components; h denotes the Eulerian grid size. The Eulerian grid size h is set to be at least two times larger than the Lagrangian grid size H to avoid missing when information is converted between mesh systems. The scalar function $\phi(r)$ has to obey the following criterions of a delta function in a discrete form:

- 1. $\phi(r)$ is continuous for all real r,
- 2. $\phi(\mathbf{r}) = 0$ for $|\mathbf{r}| \ge 2$,
- 3. $\sum_{i} j\phi(r-j) = r$ for all real r,

Based on the above conditions, the expression for $\phi(r)$ is given as

$$\phi(\mathbf{r}) = 0, |\mathbf{r}| \ge 2$$

$$= \frac{1}{8} (3 - 2|\mathbf{r}| + \sqrt{1 + 4|\mathbf{r}| - 4\mathbf{r}^2}), 0 \le |\mathbf{r}| \le 1$$

$$= \frac{1}{8} (5 - 2|\mathbf{r}| - \sqrt{-7 + 12|\mathbf{r}| - 4\mathbf{r}^2}), 1 \le |\mathbf{r}| \le 2$$
(4.15)

 $\phi(r)$ is a continuous and symmetric distribution plotted in Fig. 4.4. When |r| is larger than 2, $\phi(r)$ is δ_h has no contribution to information communication between two mesh systems. This generates a smooth but somewhat shape distribution at the vicinity of the immersed surface. Inclusion of more points blurs the boundary and reduces the accuracy while involvement of too few points might cause an extremely shape distribution which worsen the stability.

Fig. 4.3 shows how the delta distribution is used for information communication between two mesh systems. Take the Lagrangian point highlighted by a blue circle for example, in the spreading procedure, the force on the Lagrangian point is distributed through Eq. (4.14) to the blue dots on the Eulerian mesh. In the interpolation procedure, the same delta distribution function is used to interpolate the velocity on the blue dots of the Eulerian mesh to the velocity of the Lagrangian point circled blue.

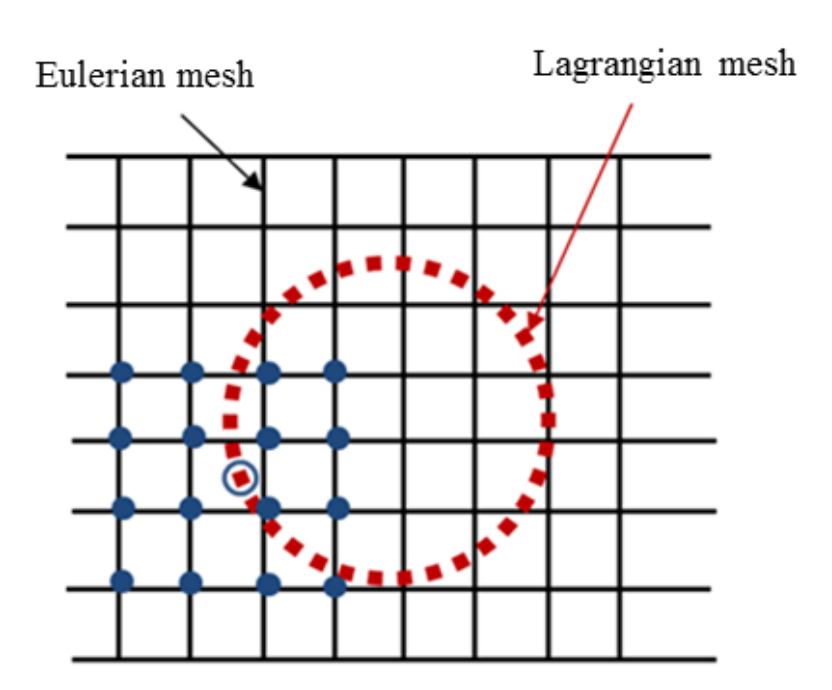


Figure 4.3: Schematic configuration shows two mesh systems and the Eulerian points involved in a spreading procedure and an interpolation procedure for one Lagrangian point.

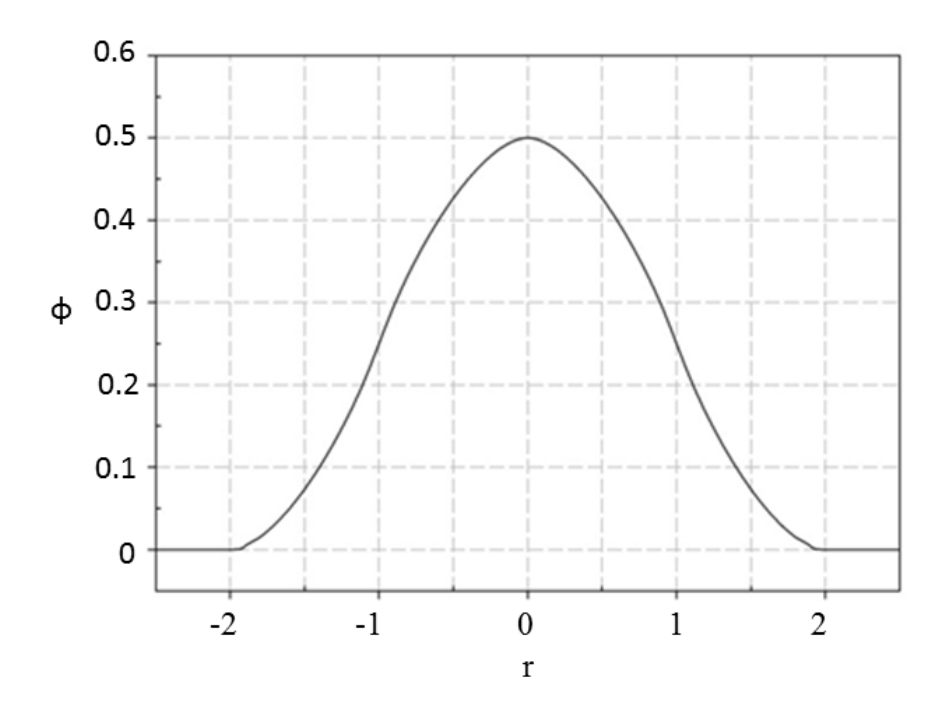


Figure 4.4: Distribution of $\phi(r)$ shows how the Dirac delta function works.

4.3 Algorithm

In this section, the algorithm of using the IB method based on the MacCormack scheme is provided for 2-D cases as the follows.

1. The predictor process solves the preliminary variables u^* , v^* , and ρ^* from the compressible N-S equation using the variables at the current time step u^n , v^n , and ρ^n .

$$\mathbf{G}_{i,j}^{*} = \mathbf{G}_{i,j}^{n} - \frac{\Delta t}{\Delta x} (\mathbf{E}_{i+1,j}^{n} - \mathbf{E}_{i,j}^{n}) - \frac{\Delta t}{\Delta y} (\mathbf{F}_{i,j+1}^{n} - \mathbf{F}_{i,j}^{n}) + \Delta t \mathbf{f}^{n}$$

$$(4.16)$$

2. The preliminary velocity at the Lagrangian points U^* , V^* is solved by Eq. (4.17) through an interpolation procedure. The Lagrangian points are moved to a preliminary location $X(s)^*$ from the location at the current time X(s) using Eq. (4.18).

$$\mathbf{U}^*(\mathbf{X}_k) = \sum_{\mathbf{x} \in \mathbf{g}_h} \mathbf{u}^*(\mathbf{x}) \delta_h(\mathbf{x} - \mathbf{X}_k^n) h^2$$
(4.17)

$$\mathbf{X}_{k}^{*} = \mathbf{X}_{k}^{n} + \Delta t \mathbf{U}(\mathbf{X}_{k})^{*}$$
(4.18)

3. Depending on whether the structure is stationary or movable in the fluid flow, the preliminary Lagrangian forcing $\mathbf{F}_{\mathbf{f}}^*$ is obtained from \mathbf{X}^n , \mathbf{X}^* , and κ using Eq (4.12) or Eq (4.13). The preliminary force density term \mathbf{f}^* is solved by Eq. (4.20) given as

$$\mathbf{f}(\mathbf{x})^* = \sum_{k=1}^{N_b} \mathbf{F_f}(\mathbf{X}_k, t)^* \delta_h(\mathbf{x} - \mathbf{X}_k) \mathbf{H}$$
(4.20)

4. Substitute the source term \mathbf{f}^* into Eq. (4.11) which is solved for the velocity and density at the next time step u^{n+1} , v^{n+1} and ρ^{n+1}

$$\mathbf{G}_{i,j}^{n+1} = \frac{1}{2} \left[\mathbf{G}_{i,j}^{n} + \mathbf{G}_{i,j}^{*} - \frac{\Delta t}{\Delta x} (\mathbf{E}_{i,j}^{*} - \mathbf{E}_{i-1,j}^{*}) - \frac{\Delta t}{\Delta y} (\mathbf{F}_{i,j}^{*} - \mathbf{F}_{i,j-1}^{*}) \right] + \frac{\Delta t}{2} \mathbf{f}^{*}$$
(4.21)

5. The location of the Lagrangian points at the time step n+1, \mathbf{X}^{n+1} is obtained by using the same equations in Step 2

$$\mathbf{U}^{n+1}(\mathbf{X}_k) = \sum_{\mathbf{x} \in \mathbf{g}_h} \mathbf{u}^{n+1}(\mathbf{x}) \delta_h(\mathbf{x} - \mathbf{X}_k^n) h^2$$
(4.22)

$$\mathbf{X}_{k}^{n+1} = \mathbf{X}_{k}^{n} + \Delta t \mathbf{U}(\mathbf{X}_{k})^{n+1}$$

$$(4.23)$$

6. Again the Lagrangian forcing $\mathbf{F_f}^{n+1}$ is computed and used to obtain the force density term for the next time step \mathbf{f}^{n+1} through Eq. (4.24)

$$\mathbf{f}(\mathbf{x})^{n+1} = \sum_{k=1}^{N_b} \mathbf{F}_{\mathbf{f}}(\mathbf{X}_k, t)^{n+1} \delta_h(\mathbf{x} - \mathbf{X}_k) \mathbf{H}$$
(4.24)

The steps above are repeated as time is matching. To reduce the numerical viscosity, one can use different combinations of forward/backward difference schemes for the space derivative discretization. In this work, the combinations are circled in an order shown in Table 4.1.

Table 4.1: Differencing sequence for the space derivative discretization

step	predictor		correcto	r
	$\partial / \partial x$	∂ / ∂y	$\partial / \partial x$	∂ / ∂y
1	F	F	В	В
2	F	В	F	В
3	В	В	F	F
4	В	F	В	F

F: forward B: backward

It is suggested by Tannehill et al. (1997) that circling those arrangements in the chronological order can reduce the truncation error. For particulate flow simulation or particle problems, Perrin and Hu (2006) found the arrangement helps avoid asymmetries due to the truncation error. To maintain second-order accuracy, the derivative terms in E and F are discretized differently. The terms with derivative in a different direction of $\partial \mathbf{E}/\partial x$ and $\partial \mathbf{F}/\partial x$ are always differenced with a central difference while the terms with derivative in the same direction of $\partial \mathbf{E}/\partial x$ and $\partial \mathbf{F}/\partial x$ are differenced in an opposite direction. For example, consider the term E₃ in the momentum equation in the y direction:

$$E_3 = \rho u v - \mu \frac{\partial u}{\partial y} - \mu \frac{\partial v}{\partial x}$$
 (4.25)

The term should be differenced in the predictor procedure as follows

$$\mathbf{E}_{i,j}^{n} = (\rho u v)_{i,j}^{n} - \mu_{i,j}^{n} \frac{u_{i,j+1}^{n} - u_{i,j-1}^{n}}{2\Delta y} - \mu_{i,j}^{n} \frac{v_{i,j}^{n} - v_{i-1,j}^{n}}{\Delta x}$$
(4.26)

The MacCormack scheme is an explicit time-marching approach. To obtain a converged solution, the time step has to satisfy the CFL condition. The following semi-empirical stability criterion is given by Tannehill et al. (1997)

$$\Delta t \le \frac{\sigma}{(1+2/\operatorname{Re}_{\Delta})} \left[\frac{|u|}{\Delta x} + \frac{|v|}{\Delta y} + c\sqrt{\frac{1}{\Delta x^2} + \frac{1}{\Delta x^2}} \right]^{-1}$$
(4.27)

where σ is a safety constant equal to 0.9; $Re_{\Delta} = \min(\rho|u|\Delta x/\mu, \, \rho|v|\Delta y/\mu)$ is the minimal mesh Reynolds number. According to this criterion, the MacCormack scheme will be inefficient for a small Reynolds number (Re<10). For a moderate Reynolds number, Perrin and Hu (2006) suggested using $\Delta t \leq 0.5 h/c$ as the time step. In this work, in order to obtain simulation convergence, we conduct a dependence study for both the grid size and the time step size.

4.4 Results and discussion

In order to test the performance of the numerical approach discussed above, the following 2-D cases are studied: (1) Poiseuille flow, (2) flow passing a stationary cylinder, and (3) rigid body impinging on a wall.

4.4.1 Poiseuille flow

Fig. 4.5 demonstrates the boundary conditions used for a simple Poiseuille flow and a Poiseuille flow with a stationary cylinder immersed. In Case 2, a cylinder with a diameter equal to L/6 (d_p =0.17) stays at the location of (5/12L, L/2). The computational domain for both cases is L (L=1) in width and 4L in length. The bounds at the top and at the bottom are wall using a noslip boundary condition (u=0, v=0). The pressure at the left bound (inlet) and at the right bound (outlet) are P₁=101 and P₁=101, respectively. The flow viscosity μ is equal to 0.01. The grid

number in the channel length N_x and the channel width N_y is [60,240] which creates a uniform Cartesian mesh for the fluid flow.

Analytical solution to the velocity profile is available for Poiseuille flows. For an arbitrary cross-section in the stream-wise direction, the velocity profiles are the same and given as

$$u(y) = cy(1-y)$$
 (4.28)

where c is a constant. Comparison of the velocity profile at the centerline of the channel length between the analytical solution and the numerical result is shown in Fig. 4.6. The plot shows that the MacCormack scheme is accurate in predicting the flow velocity.

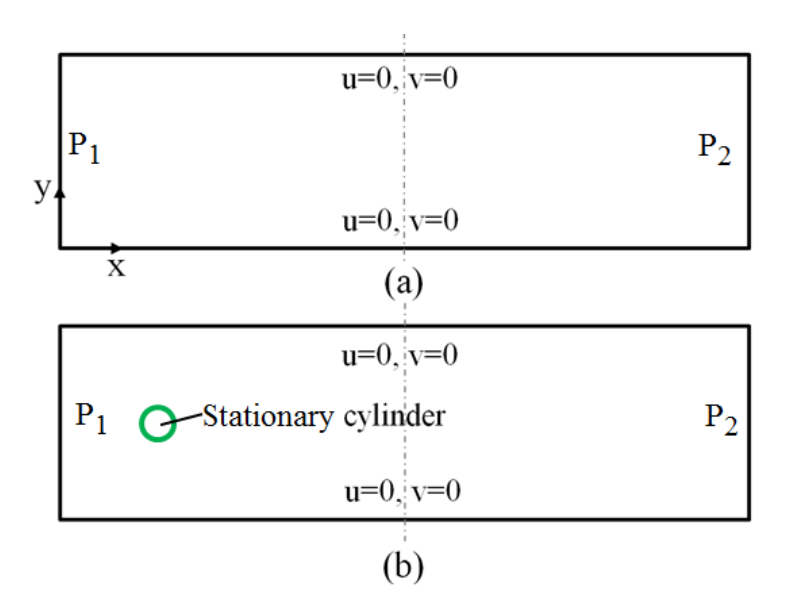


Figure 4.5: Schematic of a flow passing two parallel planes (a) without an immersed cylinder and (b) with an immersed cylinder

Fig. 4.7 demonstrates the comparison of the vector and vorticity distribution between the two cases. The vorticity is a measure of the local 'spin' or 'rotation' of the fluid and defined as the curl of the velocity field, $\omega = \nabla \times \mathbf{u}$. For a 2-D flow,

$$\omega = \frac{\partial \mathbf{v}}{\partial \mathbf{x}} - \frac{\partial \mathbf{u}}{\partial \mathbf{y}} \tag{4.29}$$

In Fig. 4.7a, the vector shows a parabolic profile cross the channel width. Since the flow is unidirectional, no vortex is observed in the flow domain. The figure on the top of Fig. 4.7b shows that the stationary cylinder located in the flow domain split the flow into two streams which are recovered downstream. Meanwhile, the velocity at the vicinity of the stationary structure is nearly zero. The figure on the bottom of Fig. 4.7b demonstrates that two vortices in an opposite direction are generated due to the presence of the cylinder.

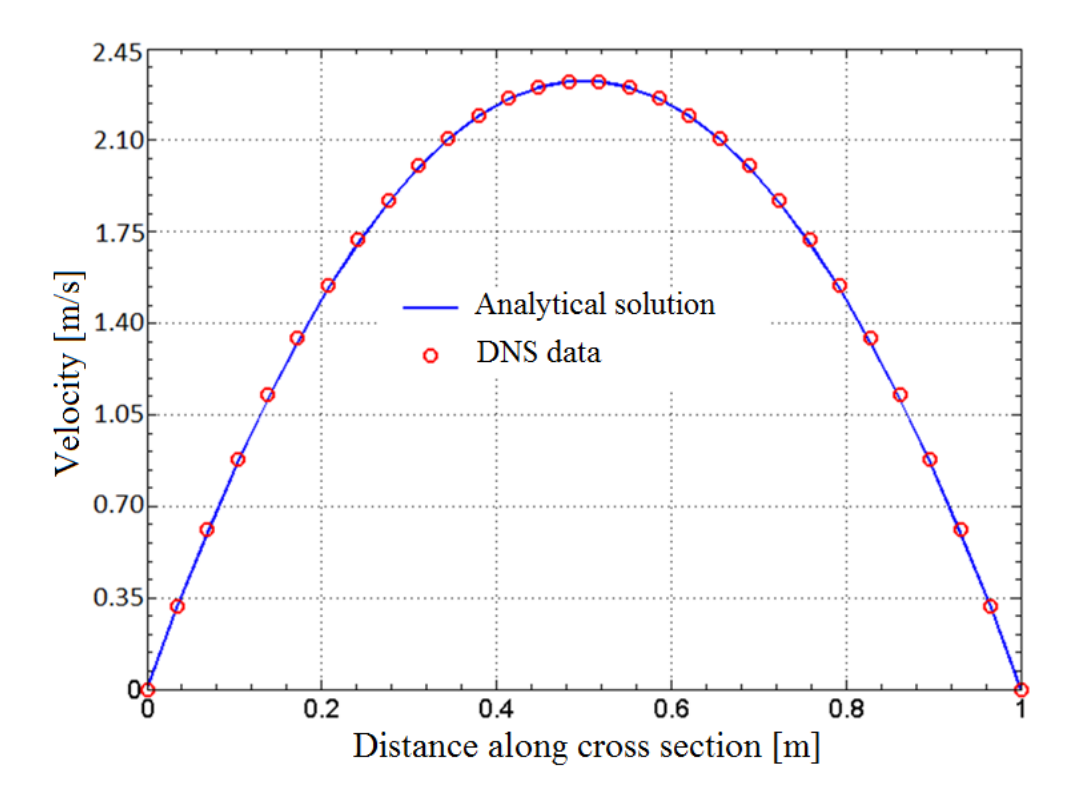


Figure 4.6: Comparison of the velocity profiles between the analytical solution and the numerical results cross the channel shows a very good agreement.

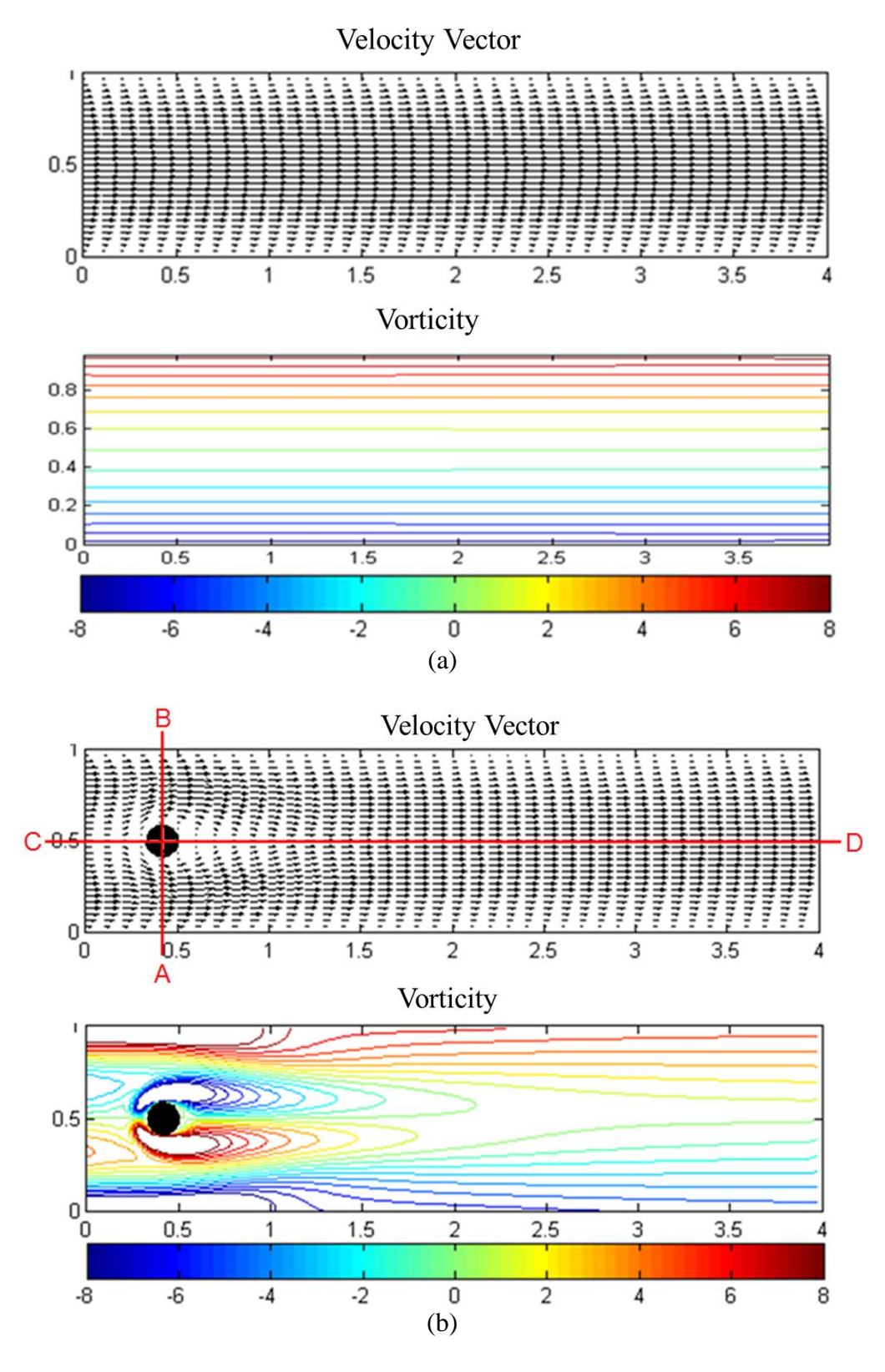


Figure 4.7: Comparison of the vector and the vorticity between (a) a Poiseuille flow (b) a Poiseuille flow interacted with a stationary structure.

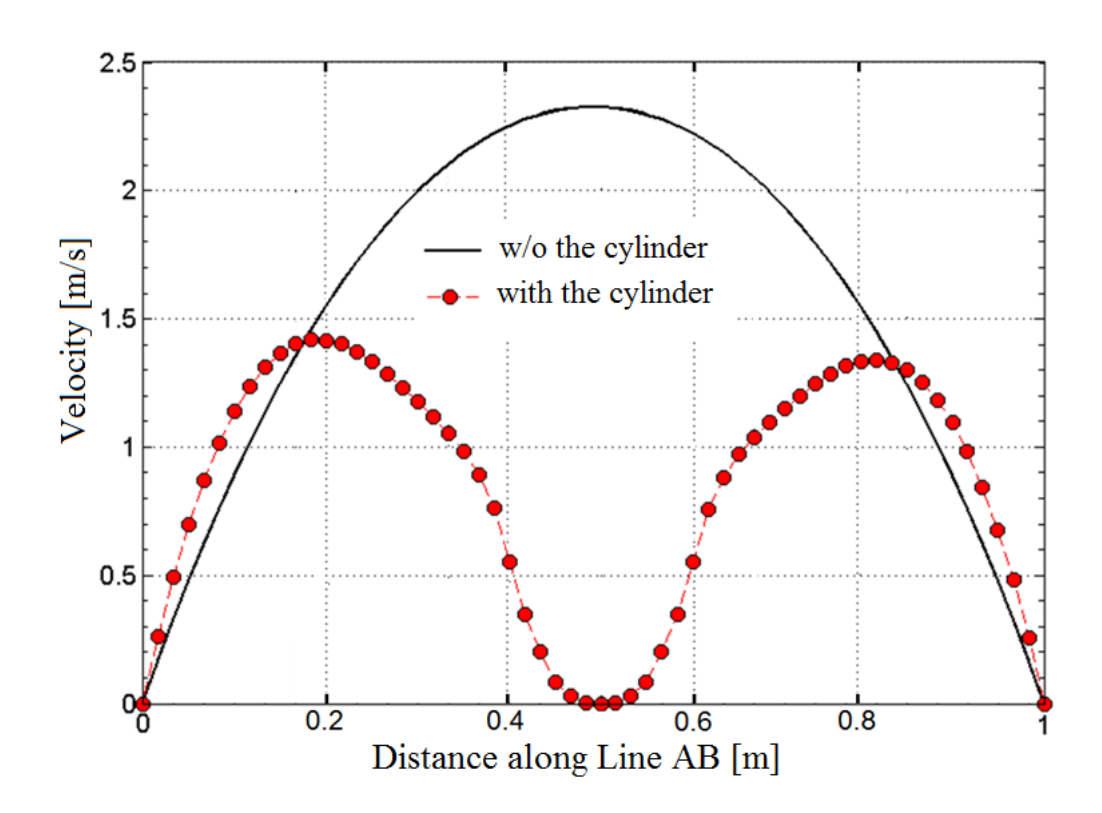


Figure 4.8: Comparison of the velocity profiles along Line AB between two cases

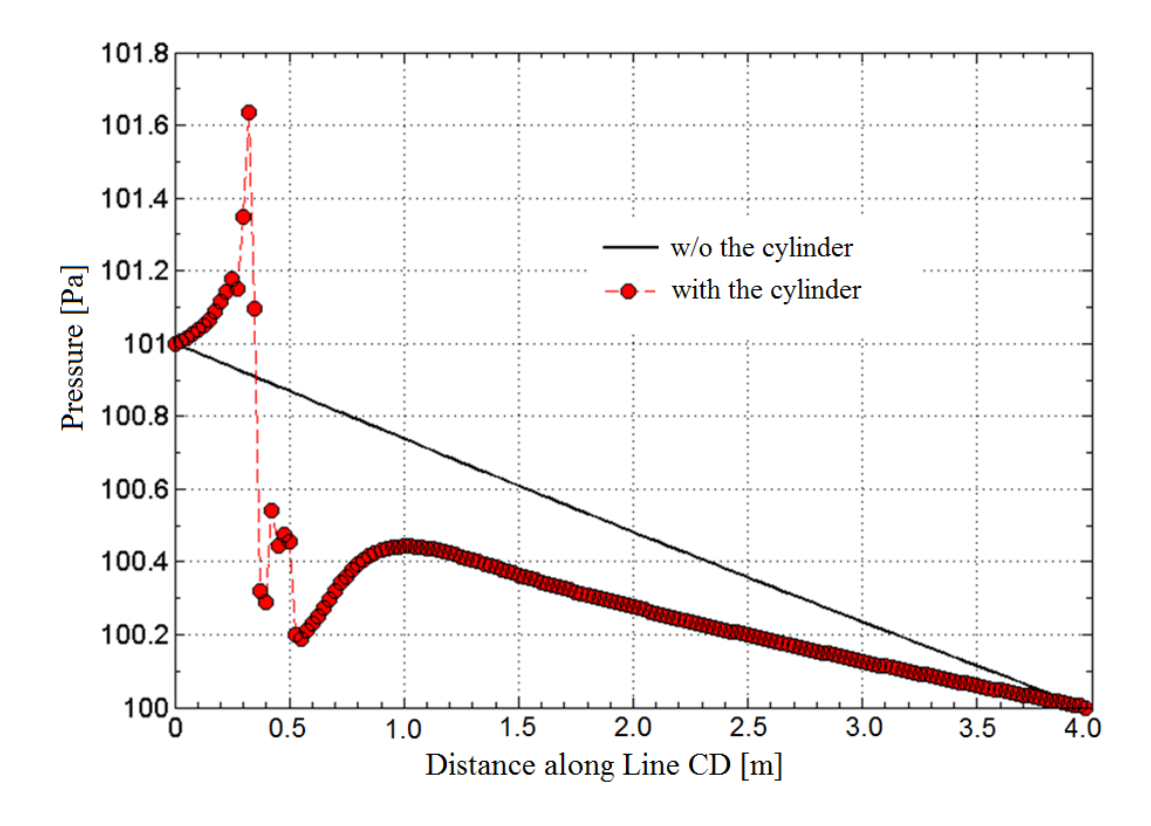


Figure 4.9: Comparison of the pressure distribution along Line CD between two cases

To study the impact of the stationary cylinder on the fluid flow, the velocity and the pressure along the line AB and CD in the above diagram are plotted in Fig. 4.8 and Fig. 4.9, respectively. The solid line in Fig. 4.8 shows a maximum velocity at the center when no cylinder is interrupting. The dash line with red dots shows that the maximum velocity is reduced due to the presence of the cylinder. In reality, velocity is equal to zero at the boundary and inside the cylinder. However, the result shows that the boundary is blurry for the Dirac delta function is used to smooth the structure surface. Accuracy would be improved by using a finer mesh. A mesh dependence study is conducted in the following section. In Fig. 4.9, the solid line shows a linear decrease along the stream-wise direction. For the other case, the presence of the stationary cylinder causes a high pressure in the front and a low pressure behind the cylinder. These phenomena are consistent with the observation in experiments.

4.4.2 Flow passing a stationary cylinder

Uniform flow passing a two-dimension stationary circular cylinder is often used as a benchmark case to evaluate the performance of a numerical method. Lai and Peskin (2000), and Uhlmann (2005) tackled the stationary cylinder by using the IB boundary method based on a projection method. Perrin and Hu (2006) enforced the no-slip boundary on the cylinder using a Taylor expansion and solved the fluid equation by the MacCormack scheme. Experiment of flow passing a stationary cylinder shows that the flow may present different flow patterns for different Reynolds number. Flow with a low Reynolds number generates two stable and symmetrical vortices behind the cylinder. Flow is unstable for Reynolds number in a certain range (typically 50<Re<10⁵), which leads to a periodic alternate shedding of vortices. This well-known phenomenon is referred to as "Kármán Vortex Street".

To characterize the flow, dimensionless numbers, such as Reynolds number Re, Strouhal number C_D , drag coefficient C_D , and the lift coefficient C_L are introduced. The Reynolds number is defined as

$$Re = \frac{\rho_f u_{\infty} d}{\mu_f} \tag{4.30}$$

where \mathbf{u}_{∞} is the far-field velocity, and d is the cylinder diameter. The Strouhal number is a measure to the vortex shedding frequency, defined as

$$Sr = f_c \frac{d}{u_\infty}$$
 (4.31)

where f_c is the vortex shedding frequency. The drag coefficient C_D and the lift coefficient C_L are to quantify the drag force or the lift force when an exterior flow is passing a blunt body. They are obtained respectively from

$$C_{D} = \frac{F_{x}}{1/2\rho_{f}u_{\infty}^{2}d}$$
 (4.32)

$$C_{L} = \frac{F_{y}}{1/2\rho_{f}u_{c}^{2}d} \tag{4.33}$$

where the drag force F_x and the lift force F_y are the force components exerted on the cylinder in the direction of the flow velocity and in the direction perpendicular the flow velocity, respectively.

Fig. 4.10 demonstrates the boundary condition used for the computational domain used for $[0, 0] \times [40d, 40d]$. A circular cylinder with d=0.2m in diameter is located at (6d, 20d). The boundary conditions on the left, bottom and top bounds are imposed with velocity $u = (u_{\infty}, 0)$

where the far-field velocity u_{∞} is equal to 1. The Neumann boundary condition is applied to the right bound using

$$\frac{\partial(\rho \mathbf{u})}{\partial \mathbf{x}} = \frac{\partial(\rho \mathbf{v})}{\partial \mathbf{x}} = 0 \tag{4.34}$$

The Reynolds number for the flow studied is equal to 100. The flow viscosity μ_f is 0.002. A low Mach number (Ma= 0.1) is maintained by using 10 for the speed of sound. Fig. 4.11 plots the vorticity patterns proceeding with time. At the beginning, two symmetric vortices rotating in the opposite direction are generated (Fig. 4.11a). With the increase of the time, the vortices are stretched further downstream (Fig. 4.11b). Fig. 4.11c shows that as the vortices grow with time, they are distorted due to the instability of the status. The vortices begin detaching from the cylinder at t=9.0s and form an alternative vortex shedding (Fig. 4.11d). This well-known phenomenon is referred to as the "Kármán Vortex Street". With the time growing, the Kármán Vortex Street becomes periodic in time (Fig. 4.11e). The above phenomena have a good agreement with the observation in experiments qualitatively.

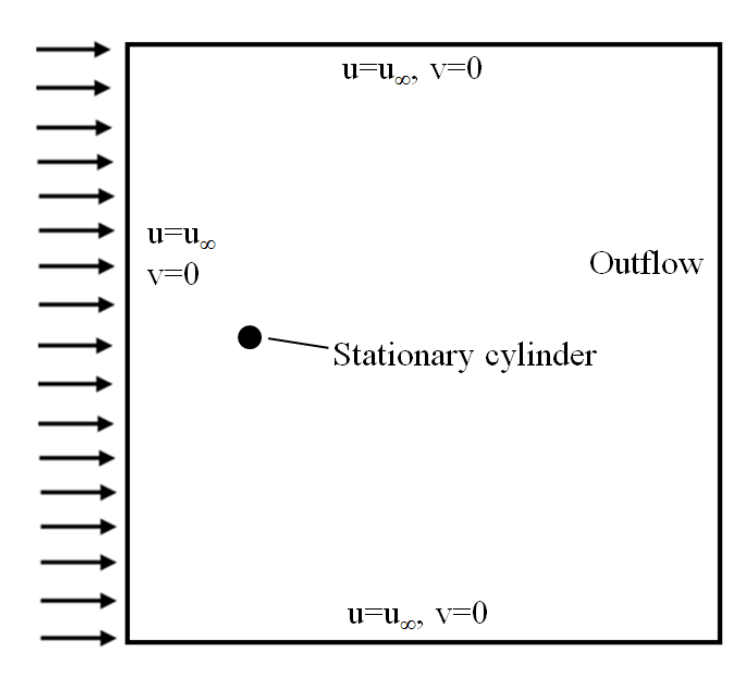


Figure 4.10: Schematic of the computational domain used for flow passing a stationary cylinder

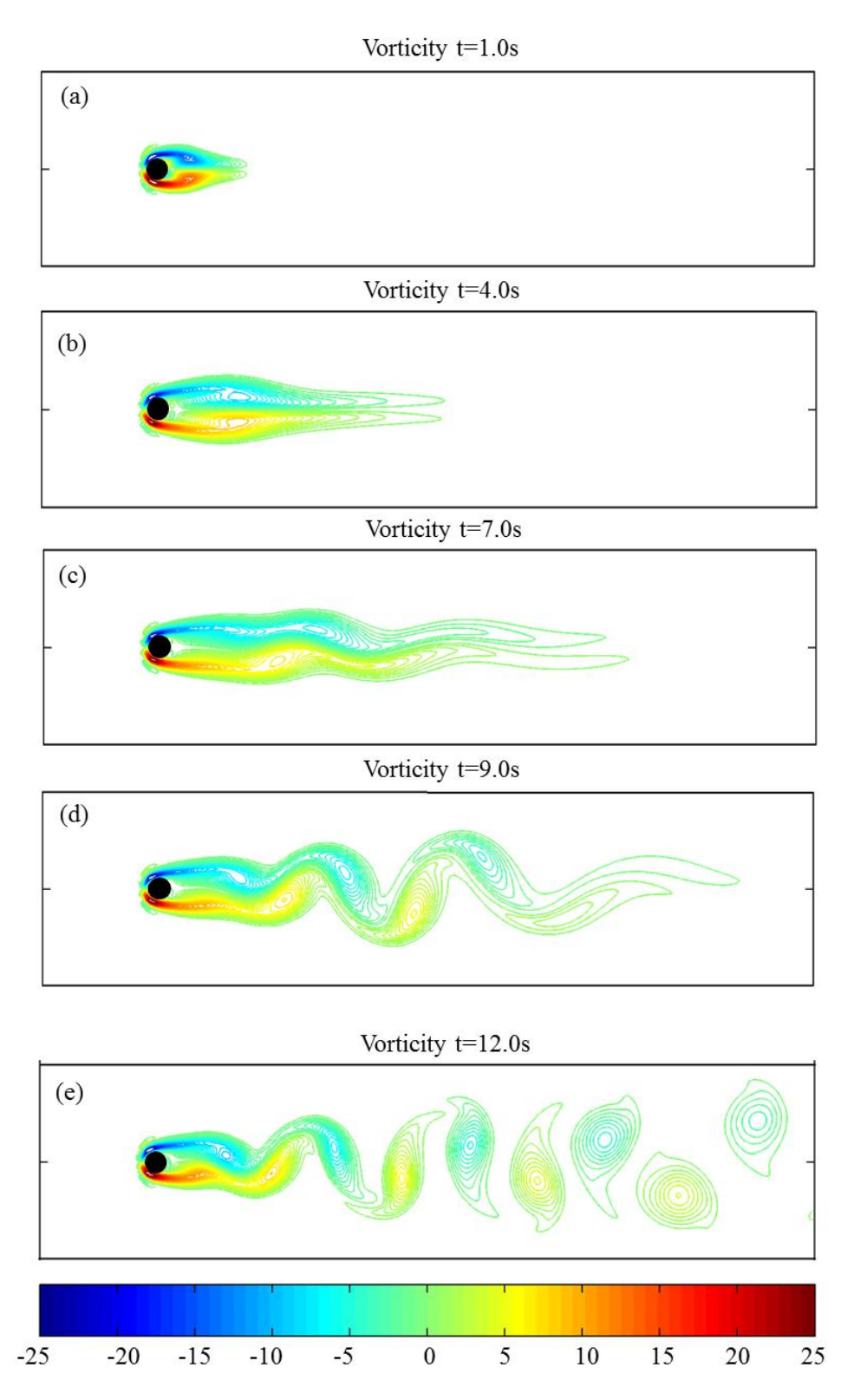


Figure 4.11: The developing vorticity patterns with a changing time shows the flow eventually breaks into a periodic K árm án Vortex Street.

Table 4.2 compares the drag coefficient C_D between the present scheme and the reference data provided by Liu et al. (1998). The reference drag coefficient is 1.35 for flow with Re=100. A mesh dependence study is conducted at first by using different grid sizes h equal to 1/32, 1/64, and 1/128. The time step uses the one suggested by Perrin and Hu (2006), which is $\Delta t = 0.5 g_h/c$. The table shows that the discrepancy of C_D predicted by the elastic forcing method is reduced drastically from 94.8% to 11.8% when the grid size is decreased from 1/32 to 1/128. Using a smaller time step 2/5 Δt improves the accuracy for the cases with the grid size 1/64 by 14%. Since no much change is obtained from 1/48 to 1/64 for time step 2/5 Δt , it can be concluded that the solution is mesh dependence. For time step 1/5 Δt with the mesh size 1/48, the discrepancy is reduced from 18.5% to 11.9%. Therefore, the time step size 1/5 Δt is recommended to avoid using a dense mesh. Although dependence study was performed in time and space for computational convergence, the scheme is inaccurate in predicting C_D with a discrepancy of 11.9%.

Table 4.2: Mesh dependence study in space and time for flow with Re=100

Time step	$\Delta t = 0.5g_h / c$		2/5∆t		1/5∆t		Reference C _D	
Mesh Size	C_{D}	Discrepancy	C_{D}	Discrepancy	C_{D}	Discrepancy	Lin et al.(1998)	
1/32	2.63	94.8%	1.87	38.5%	-	-	1.05	
1/48	-	-	1.60	18.5%	1.51	11.9%	1.35	
1/64	1.78	31.9%	1.59	17.8%	-	-		
1/128	1.51	11.9%	-	-	-	-		

4.4.3 Particle impinging on a wall

In this section, a rigid disc settling under gravity and impinging on a stationary wall is simulated using the elastic forcing method. The computational domain is shown in Fig. 4.12 with

the dimension of $[0\ 0] \times [48d_p\ 48d_p]$. A periodic boundary condition is imposed on all the bounds. The domain has grid points of $[480\ 480]$ to ensure 10 grid points are across the disc. At t=0, the disc is located at $(38.4d_p,\ 24d_p)$. A stationary wall is located below the disc at the cross section of y=6d_p. The disc is equal to 1 in diameter $(d_p=1)$. The ratio of the disc density and the fluid density is $\rho_p/\rho_f=1.1$ and the flow viscosity μ is 0.1. Both the wall and the disc are treated as immersed boundaries. The disc is released under the gravity g= (0,-9.8). The maximum Reynolds number Re_{max} for this case is $Re_{max}\approx 10$.

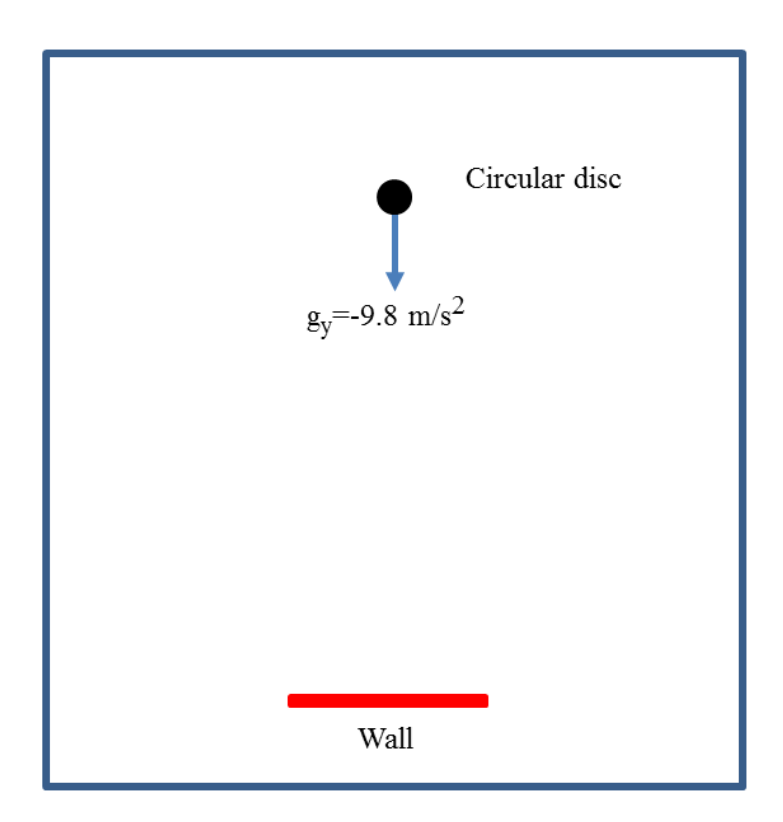


Figure 4.12: Schematic of computational domain for a disc settling under gravity and a stationary wall

The curves in Fig. 4.13 show the vertical velocity and the vertical location at the center of a disc as well as the wall location changing with time under gravity. The vertical axis on the left is velocity while on the right is location. The disc experiences four different stages as the plot shown. Snapshots of the velocity contour during this process are also shown in Fig. 4.14.

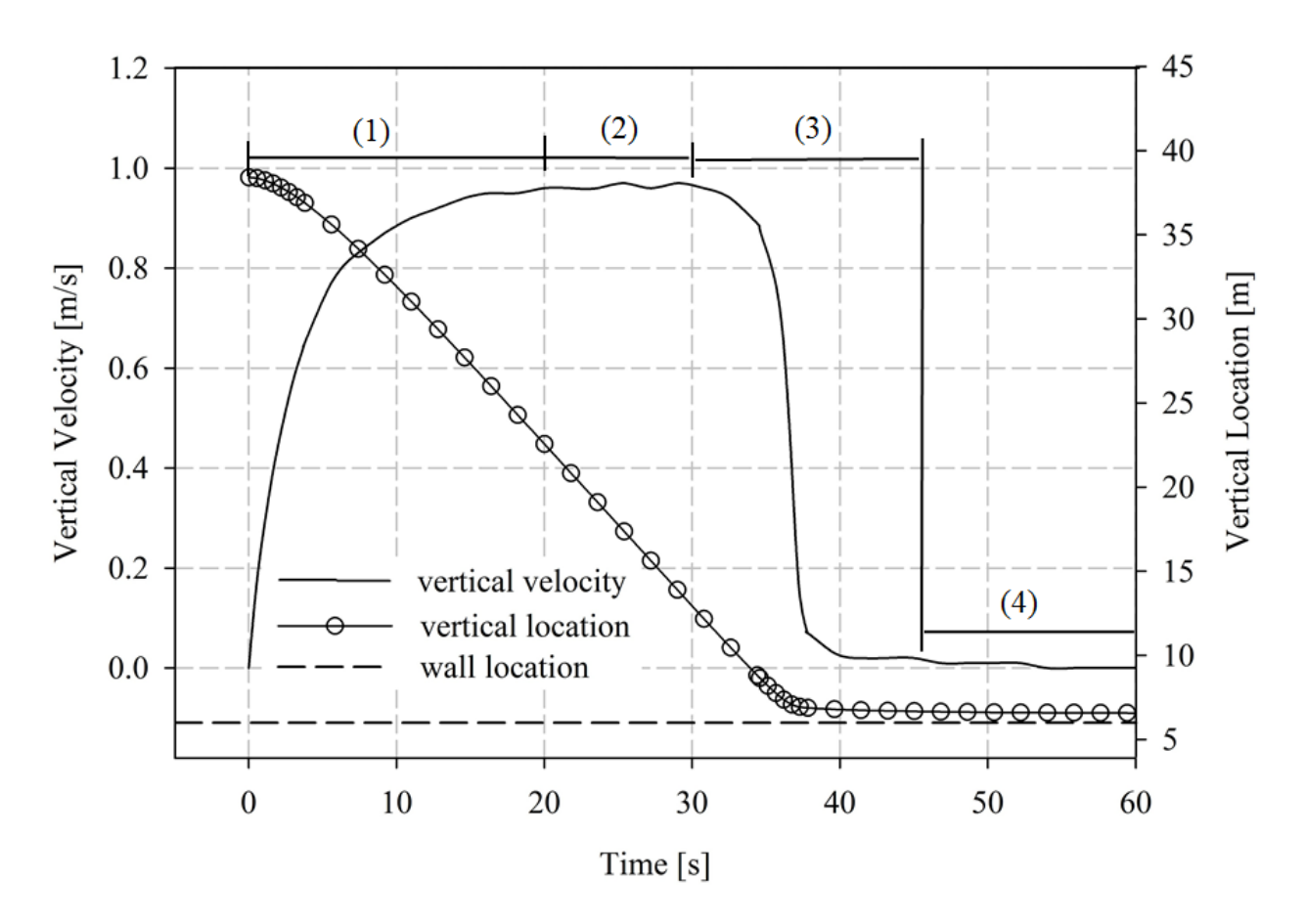


Figure 4.13: The vertical velocity and center location of the disc changing with time shows the settling disc is (1) accelerated, (2) with constant velocity, (3) decelerated, and (4) at rest.

At the beginning, the velocity of the disc speeds up very fast due to the gravitational force. The acceleration is slowed down when the drag force is enhanced due to an increasing disc Reynolds number. When the increasing drag force and the gravity become equilibrium at t=20s,

the disc reaches the maximum velocity called the "terminal velocity". Shown in Fig. 4.14b, the terminal velocity is 0.97m/s in the negative y direction. In stage 2, the disc is falling with the terminal velocity until the equilibrium between the drag force and the gravity is broken at t≈30s due to the presence of the wall. When a particle comes near a wall, the drag force is inversely proportional to the distance from the disc to the wall (Brenner 1961). This force is also referred to as "lubrication force" from the wall which is so large when the disc is getting close to the wall that the disc velocity is reduced dramatically in a short time (stage 3). Finally, the disc is resting on the top the wall. The curves in Fig. 4.13 show that the disc center and the wall location are 6.502m and 6m, respectively. Therefore, it is reasonable to say that the bottom of the disc is located right on the stationary wall. This can also be seen in Fig. 4.14d. Although no collision scheme is used when the disc is approaching to the wall, the elastic forcing method handles the boundary well. The gravity is balanced through the fluid flow in the vicinity of the disc contributed by the deformation of the stationary wall.

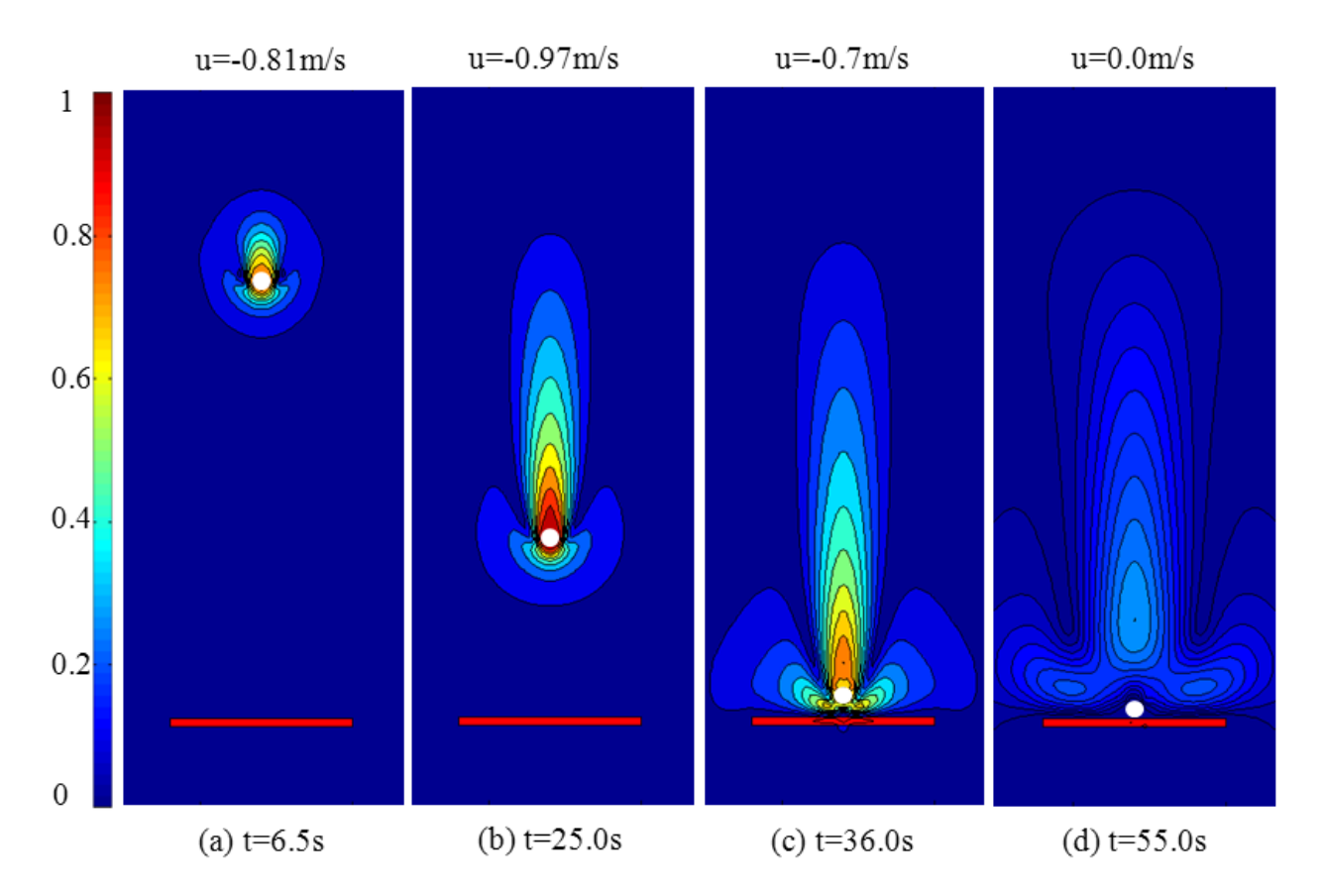


Figure 4.14: Schematic of velocity contour shows a disc is settling under gravity and impinging on a stationary wall.

4.5 Summary

An algorithm is developed for combining the MacCormack scheme with the IB method. The technique tracks the structure surface using a set of discrete Lagrangian points. The force exerted on the Lagrangian points is computed via an elastic forcing method. Considering the reacting force on the fluid flow in a source term of the momentum equation, the fluid equations were solved in a rectangular Cartesian mesh. The method is flexible and easy to implement. In this chapter, the method is tested in the cases of stationary disc in a Poiseuille flow, uniform flow passing a stationary cylinder, and particle impinging on a stationary wall.

For stationary bodies, result shows that the no-slip boundary is handled properly by the numerical approach. For example, using the elastic forcing method for a sealed stationary structure can avoid flow penetrating into the body. It is observed that blurry boundary due to the application of the Dirac delta function can cause numerical viscosity. This would be overcome by using a finer mesh in the vicinity of the immersed boundary. When two rigid bodies are approaching closely to each other, the hydrodynamic force generated is handled automatically by the method without using a collision scheme. This is a great benefit of using a virtual boundary method. The numerical method is promising and able to qualitatively capture important physical phenomena observed in experiment, such as K árm án Vortex Street, particle impinging on a wall, etc. However, quantitative study of flow passing a stationary cylinder indicates that the numerical approach is not accurate compared to other models in estimating the drag coefficient and the lift coefficient. A numerical viscosity is caused due to the intrinsic defect of treating a rigid surface as an elastic boundary. It seems that to reduce the numerical viscosity, one can use an extremely large stiffness coefficient for the springs. However using such a large stiffness coefficient could cause stability issue. To ensure the stability, the time step size Δt has to be larger than the characteristic time of spring damping and stretching t_s. A very large stiffness coefficient could dramatically reduce t_s and thus put a severe restriction on the time step used. In order to increase the accuracy while maintain the stability, a fictitious domain method is introduced to simulate particulate-laden flows in the following chapter.

CHAPTER 5

DIRECT NUMERICAL SIMULATION OF PARTICULATE-LADEN FLOW USING AN FICFICIOUS DOMAIN METHOD BASED ON THE IMMERSED BOUNDARY METHOD

In Chapter 4, it was found that the elastic forcing method can predict important physical phenomena, such as K árm án Vortex Street behind a cylinder and particles impinging on a wall. However, since the method treats a rigid body as a slightly deformable boundary using a large stiffness, the technique may exhibit stability problems during the solution. In this chapter, instead of using the elastic forcing method, the fictitious domain method developed by Uhlmann (2005) is employed to compute the force density terms used to enforce the no slip boundary condition. The technique is combined with the MacCormack scheme to simulate particulate-laden flows. A collision scheme introduced by Glowinski et al. (1999) is used to account for rigid body collision. Simulations of flow passing a stationary cylinder, particle sedimentation, and inertia-induced particle sedimentation are performed to test the numerical method. Finally, the method is used to validate the mixture model in the commercial software ANSYS FLUENT. Study focuses on the behavior of neutrally buoyant particles in a Couette flow and a Poiseuille flow.

5.1 The fictitious domain method

The immersed boundary method considers the impact of an immersed structure on a fluid flow in a force density term added to the momentum equation (Mohd-Yusof 1997). For a time derivative term evaluated at an intermediate time level, n+1/2, then the time-discretized incompressible N-S equation is given by

$$\frac{\mathbf{u}^{n+1} - \mathbf{u}^n}{\Delta t} = \mathbf{rhs}^{n+1/2} + \mathbf{f}^{n+1/2}$$
(5.1)

where $\mathbf{rhs}^{n+1/2}$ combines the convective, pressure and viscous terms. To satisfy the no-slip boundary condition, the desired velocity (\mathbf{v}) of a flow imposed on the immersed boundary generates the force density term given by

$$\mathbf{f}^{n+1/2} = \frac{\mathbf{v}^{n+1} - \mathbf{u}^n}{\Delta t} - \mathbf{rhs}^{n+1/2}$$
 (5.2)

Uhlmann (2005) states that Eq. (5.2) can be evaluated at the Lagrangian points representing the moving body through Dirac delta functions. The corresponding expression is given as

$$\mathbf{F}(\mathbf{X}_{k})^{n+1/2} = \frac{\mathbf{V}(\mathbf{X}_{k})^{n+1} - \tilde{\mathbf{U}}(\mathbf{X}_{k})}{\Lambda t}$$
(5.3)

where $\tilde{\mathbf{U}}$ is the Lagrangian form of the preliminary velocity $\tilde{\mathbf{u}}$

$$\tilde{\mathbf{u}} = \mathbf{u}^{n} - \Delta t \cdot \mathbf{rhs}^{n+1/2} \tag{5.4}$$

A compressible N-S equation can also be solved for $\tilde{\mathbf{u}}$ by using the MacCormack scheme introduced in Chapter 4. The desired velocity at the k_{th} Lagrangian point $V(X_k)$ can be obtained from

$$\mathbf{V}(\mathbf{X}_{k}) = \mathbf{u}_{c} + \mathbf{\omega}_{c} \times (\mathbf{X}_{k} - \mathbf{x}_{c}) \tag{5.5}$$

In Eq. (5.5), \mathbf{x}_c is the coordinate of the geometric center. \mathbf{u}_c is the translational velocity. For a 2-D case, the angular velocity ω_c is a scalar. For situation of stationary rigid boundaries, both the translational velocity and the angular velocity are set to be zero. When considering a moving rigid boundary, \mathbf{u}_c and ω_c are determined from the force balance equation and the torque balance equation, given as

$$V_{c}(\rho_{p} - \rho_{f})\dot{\mathbf{u}}_{c} = -\rho_{f} \int_{S} \mathbf{F} d\mathbf{x} + V_{c}(\rho_{p} - \rho_{f})\mathbf{g}$$

$$(5.6)$$

$$I_{c}(1 - \frac{\rho_{f}}{\rho_{p}})\dot{\omega}_{c} = -\rho_{f}\int_{S} (\mathbf{X} - \mathbf{x}_{c}) \times \mathbf{F} d\mathbf{x}$$
(5.7)

The derivation for Eq. (5.6)-(5.7) can be found in Appendix B. The discrete form of the above equations for a 2-D case is

$$V_c(\rho_p - \rho_f) \frac{\mathbf{u}_c^{n+1} - \mathbf{u}_c^n}{\Delta t} = -\rho_f \sum_k \mathbf{F}(\mathbf{X}_k) \Delta V_k + V_c(\rho_p - \rho_f) \mathbf{g}$$
(5.8)

$$I_{c}(1 - \frac{\rho_{f}}{\rho_{p}}) \frac{\omega_{c}^{n+1} - \omega_{c}^{n}}{\Delta t} = -\rho_{f} \sum_{k} (\mathbf{X}_{k} - \mathbf{x}_{c}) \times \mathbf{F}(\mathbf{X}_{k}) \Delta V_{k}$$

$$(5.9)$$

 ΔV_k is the control volume of the k_{th} Lagrangian point equal to the square of the Lagrangian grid size $H^2.$

The preliminary velocity on the Lagrangian points, $\tilde{\mathbf{U}}(\mathbf{X}_k,t)$, and the force density on the Eulerian mesh, $\mathbf{f}(\mathbf{x},t)$ are obtained through intergrating the Dirac delta function from Eq. (4.15). We have

$$\tilde{\mathbf{U}}(\mathbf{X}_{k}, t) = \sum_{\mathbf{X} \in g_{h}} \tilde{\mathbf{u}}(\mathbf{x}, t) \delta_{h}(\mathbf{x} - \mathbf{X}_{k}) h^{2}$$
(5.10)

$$\mathbf{f}(\mathbf{x},t) = \sum_{k=1}^{N_b} \mathbf{F}_k(\mathbf{X}_k,t) \delta_h(\mathbf{x} - \mathbf{X}_k) \Delta V_k$$
 (5.11)

5.2 Collision scheme

Unlike the elastic forcing method which directly moves the Lagrangian points, the fictitious domain method moves and rotates the geometric center of a rigid structure through the translational velocity \mathbf{u}_c and the angular velocity ω_c . Therefore, there is a possibility for surface superposition when two particles approach to each other. This violates the famous Stokes

paradox saying that two rigid bodies can never make contact in a finite time in a viscous fluid because of the infinite "lubrication force" when the distance approaches zero at the last moment of contact (Zhang et al. 2005). Therefore a collision scheme is necessary to prevent collision when two rigid structures approach closely to each other.

For particulate-laden flow, we use the collision scheme developed by Glowinski et al. (1999). Fig. 5.1 demonstrates the method used for two spherical particles and for a particle moving toward a stationary wall. In Fig. 5.1a, d_{12} denotes the distance between the center of two particles P_1 and P_2 . A safety zone with the thickness l_s is imposed on each particle to avoid collision. For particles in radius R_1 and R_2 , the repulsive force \mathbf{Fr} is generated when d_{12} is smaller than the critical distance $d_s = R_1 + R_2 + l_s$. For $d_{12} > d_s$, the repulsive force \mathbf{Fr} is zero. The above method can also be used to avoid collision when a rigid particle is approaching to a stationary wall by adding a ghost particle in the same radius in the wall (shown as in Fig. 5.1b). The equation for the collision scheme for m rigid particles is given as

$$\mathbf{F}\mathbf{r}_{i}^{p} = \sum_{j \neq i}^{m} \mathbf{F}\mathbf{r}_{i,j}^{p} = \begin{cases} 0 & d_{ij} > d_{s} \\ \sum_{j \neq i}^{m} \frac{1}{\varepsilon_{p}} (\mathbf{X}_{i} - \mathbf{X}_{j}) (d_{s} - d_{ij})^{2} & d_{ij} < d_{s} \end{cases}$$

$$(5.12)$$

where ϵ_p is a small stiffness constant; the critical distance between particle P_i and P_j is $d_s=R_i+R_j+l_s$; the distance between the center of P_i and P_j is computed by $|\mathbf{X}_i-\mathbf{X}_j|$. The force acting on the particle P_i is the summation of force exerted by all other particle P_j ($j\neq i$). For example, Fig. 5.2 plots the repulsive force for two particles with the same radius 1. The thickness of the safety zone is 0.1. The stiffness constant ϵ_p uses a small value 1×10^{-7} . The curve shows

that when the distance of two particles is larger than 2.1, the repulsive force acting on the particle is equal to zero. Within the safety zone, the force is activated and is increased exponentially with the decrease of the particle distance. This force is so large than two particles coming to together will be push back to their opposite directions. For elliptical particles, the scheme can be applied by using an equivalent diameter. The equivalent diameter for a ellipsoid is the diameter for a sphere possessing the same volume of this ellipsoid.

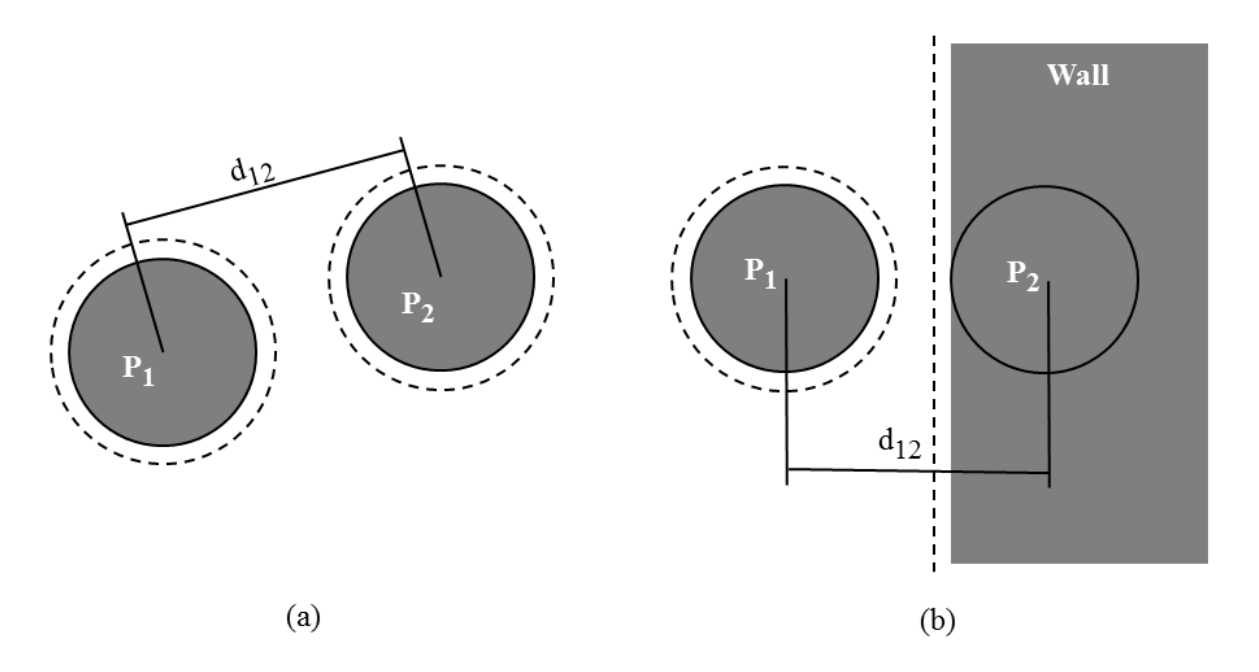


Figure 5.1: Schematic of the collision scheme used to prevent collision between (a) two particles (b) a particle and a stationary wall

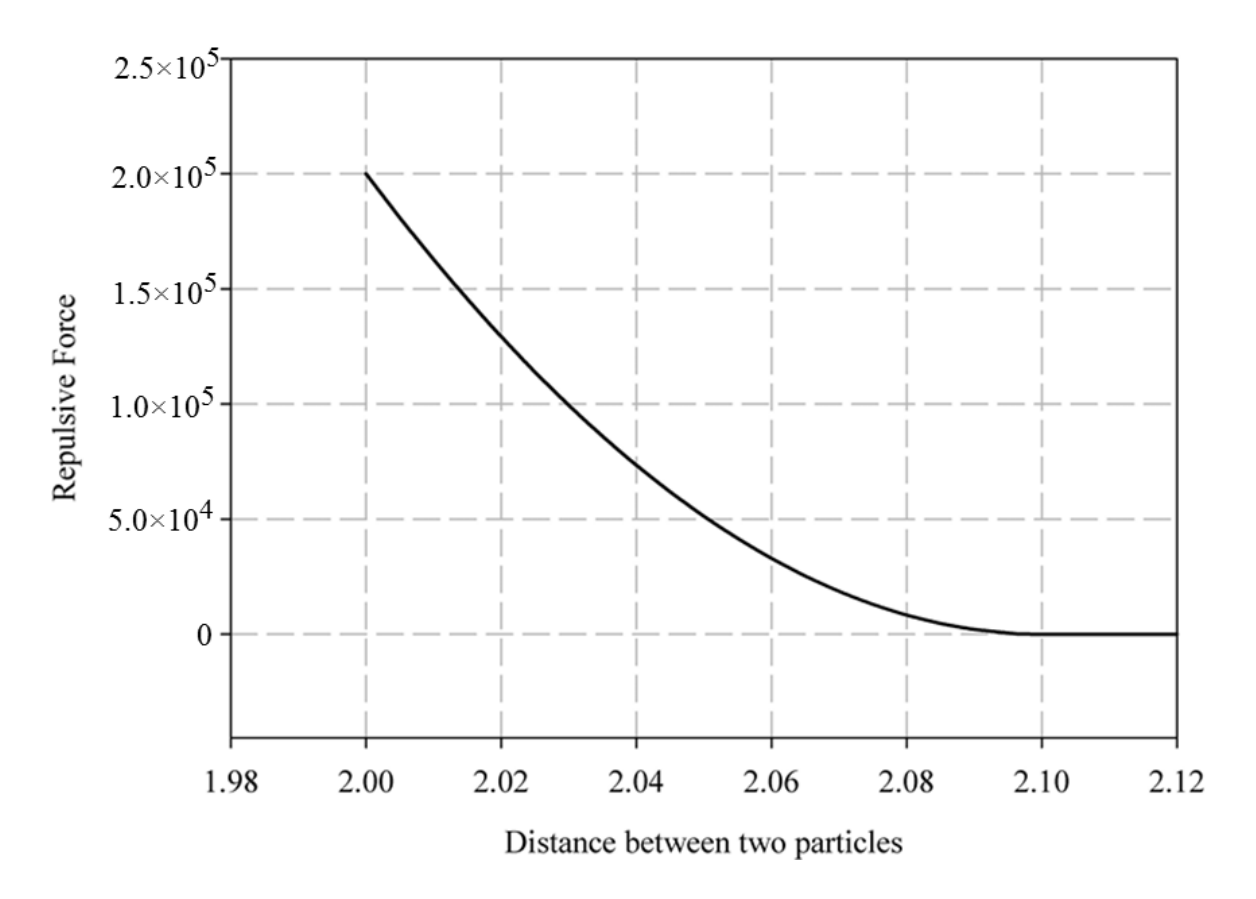


Figure 5.2: A curve shows the repulsive force acting on a rigid particle is decreased dramatically as the increase of particle distance within the safety zone and is zero out of the safety zone.

5.3 Test cases

The performance of the fictitious domain method based on the explicit MacCormack scheme is tested in the following cases: flow around a stationary cylinder, particle sedimentation, and inertia-induced particle migration.

5.3.1 Flow passing a stationary cylinder

In Chapter 4, simulation of flow passing a stationary rigid cylinder is performed by using the elastic forcing method. As a benchmark case, we use it to validate the fictitious domain method based on the MacCormack scheme. The application of the fictitious domain method on a

stationary rigid structure can be simply achieved through setting the desired velocity V(X) (Eq. (5.5)) equals to zero. The Reynolds number for this case is 100. One can refer to Section 4.4.2 for the detail of the case studied. Numerical results of the drag coefficient C_D , the drag coefficient fluctuation C_D , the lift coefficient C_L , and the Strouhal number Sr are compared to the elastic forcing method and other sources in Table 5.1. The mesh and the time step size used in this case are 1/48 and $1/5\Delta t$ (Δt =0.5h/c), respectively.

Compared to the reference data (Liu et al. 1998), the fictitious domain method performs the best in estimating the drag coefficient with a discrepancy of 0.7%. Lai & Peskin (2000) and Uhlmann (2005) used the elastic forcing method and the fictitious domain method based on a project method, respectively. The discrepancies of C_D from their schemes are both 7.4%. The reason that our scheme (the fictitious domain method based on the MacCormack solver) outmatches the other two models may be due to the small time step used.

Table 5.1: Comparison of results from the current schemes and other methods (Re=100)

	C_{D}	Discrepancy [%]	C _D '	C_{L}	Sr
Elastic forcing method	1.51	11.9	±0.014	±0.342	0.165
Fictitious domain method	1.34	0.7	±0.013	± 0.337	0.164
Lai & Peskin (2000)	1.45	7.4	-	± 0.329	0.165
Uhlmann (2005)	1.45	7.4	± 0.011	± 0.339	0.169
Perrin and Hu (2006)	2.0	48.1	-	-	0.233
Liu et al. (1998)	1.35	-	±0.012	±0.339	0.165

5.3.2 Particle sedimentation

In this section, simulations of disc settling under gravity are conducted. The cases include single disc sedimentation, two discs drafting-kissing-tumbling (DKT) and 240 particles settling in a sealed container.

(a) Single disc setting under gravity

A single circular disk falling under gravity is simulated using the MacCormack solver with the elastic forcing method and the fictitious domain method. The circular disc is 0.2m in diameter (d_p = 0.2m). It is located at the original point of the computational domain [-12 d_p , 12 d_p] × [-65 d_p , 7 d_p]. The ratio of the disc density ρ_p and the flow density ρ_f is 1.5. The mesh size uses 240×720. The boundary conditions on the top and the bottom are periodic. On the left and right bounds, the outflow boundary condition from Eq. (4.34) is used. At t=0, the velocity for the disc and the fluid flow are at rest. At t>0, the disc is released under the gravity \mathbf{g} = (0, -9.8m/s²). The computation is stopped when the disc reaches y=-7m.

Fig. 5.3a shows the comparison of the elastic forcing method and the fictitious domain method in estimating the center position of the disc settling. The maximum Reynolds number obtained for this case is 100. At the beginning of the settling process, it can be seen that no horizontal displacement Δy is generated for two methods. Due to the increase of the particle velocity, the Re number is increased and the elastic forcing method predicts a Δy for t>2.5s. Fig. 5.3b shows the comparison of the disc velocity from two methods. It can be seen that the velocity of the disc increases with time until the gravity is balanced with the increasing drag force. Thereafter, the disc velocity becomes a constant called the terminal velocity. Analytical solution to the terminal velocity is available for comparison. For Re=100, the analytical solution to the terminal velocity is 1.08m/s (shown as a dot line in Fig. 5.3b). Fig. 5.3b shows that the terminal velocity from the fictitious domain method has a good agreement with the analytical solution where a deviation of 3% is obtained. The elastic forcing method underestimates the terminal velocity with a deviation of 20%. Moreover, the elastic forcing method could cause

velocity fluctuation in the vertical direction u_x' and a horizontal velocity u_y when t>2.5s. The reason of causing the fluctuation may be due to the participation of large amount of springs to mimic a rigid body. For the fictitious domain method, no u_x' and u_y are observed in the results. This indicates that the method has a good stability.

Fig. 5.4 shows the comparison of the disc center position and the disc velocity between two methods for Re \approx 10. For a small Reynolds number, both the elastic forcing method and the fictitious domain method predict the disc falling on the centerline of the flow domain, which indicates both the methods are stable for flow with a low Reynolds number. The terminal velocity from the elastic force method is 14% lower compared to the result from the fictitious domain method. We know from the last section that the elastic force method tends to overestimate the drag coefficient C_D and thus reduces the terminal velocity. Since the fictitious domain method performs better in stability and accuracy on rigid particle simulation, we use this method for particle flow simulation for the rest cases.

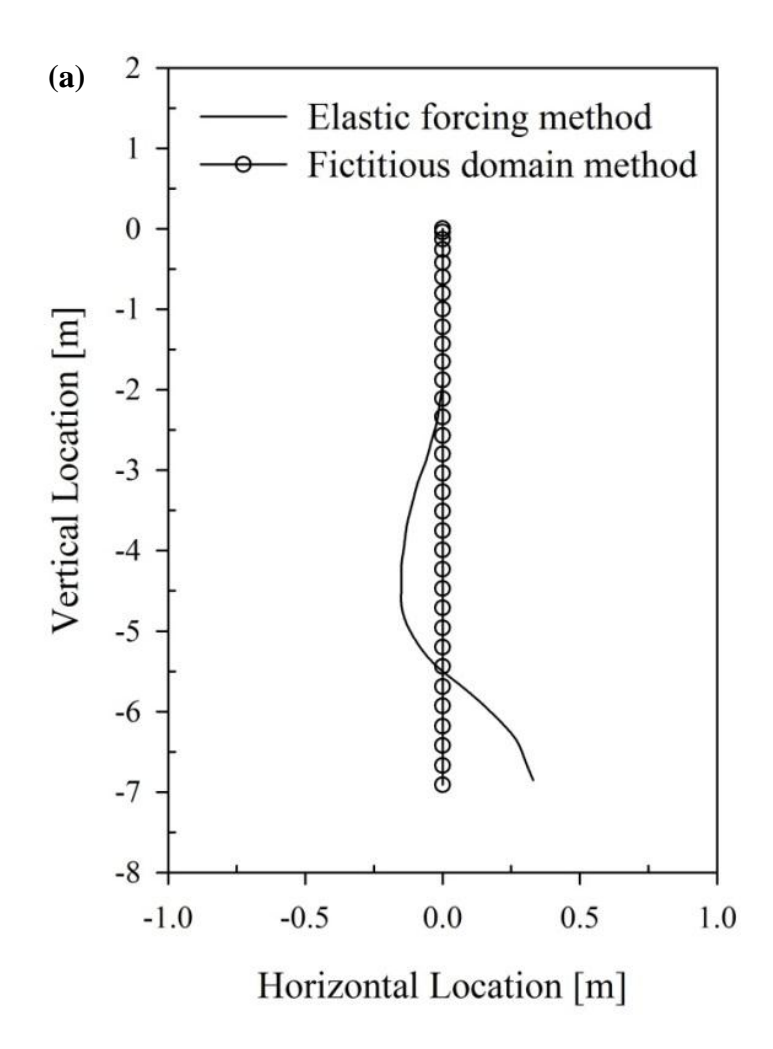
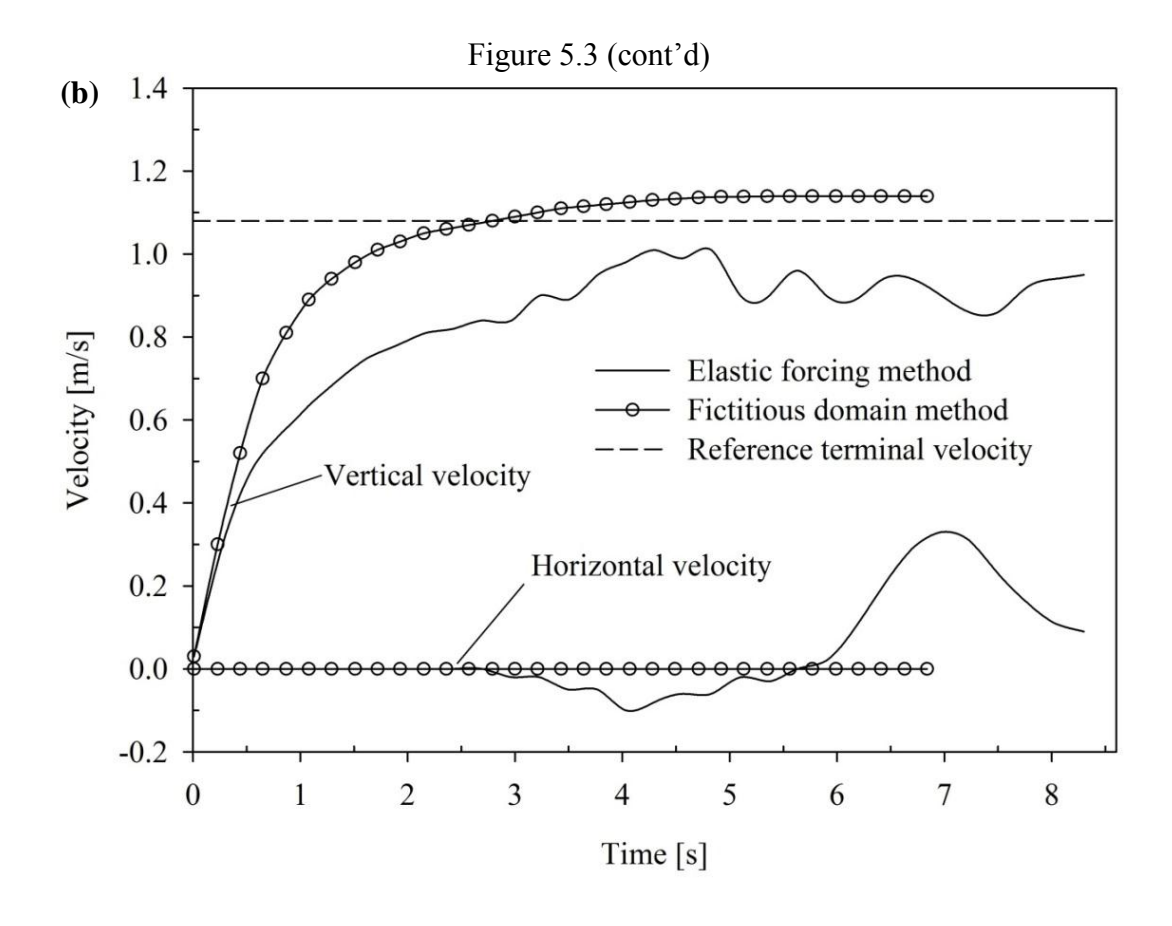


Figure 5.3: Comparison of (a) disc position and (b) disc velocity between the elastic forcing method and the fictitious domain method shows that the fictitious domain method (short dash) outperforms the elastic forcing method (solid line) in estimating the terminal velocity of a disc falling in a flow with Re=100.



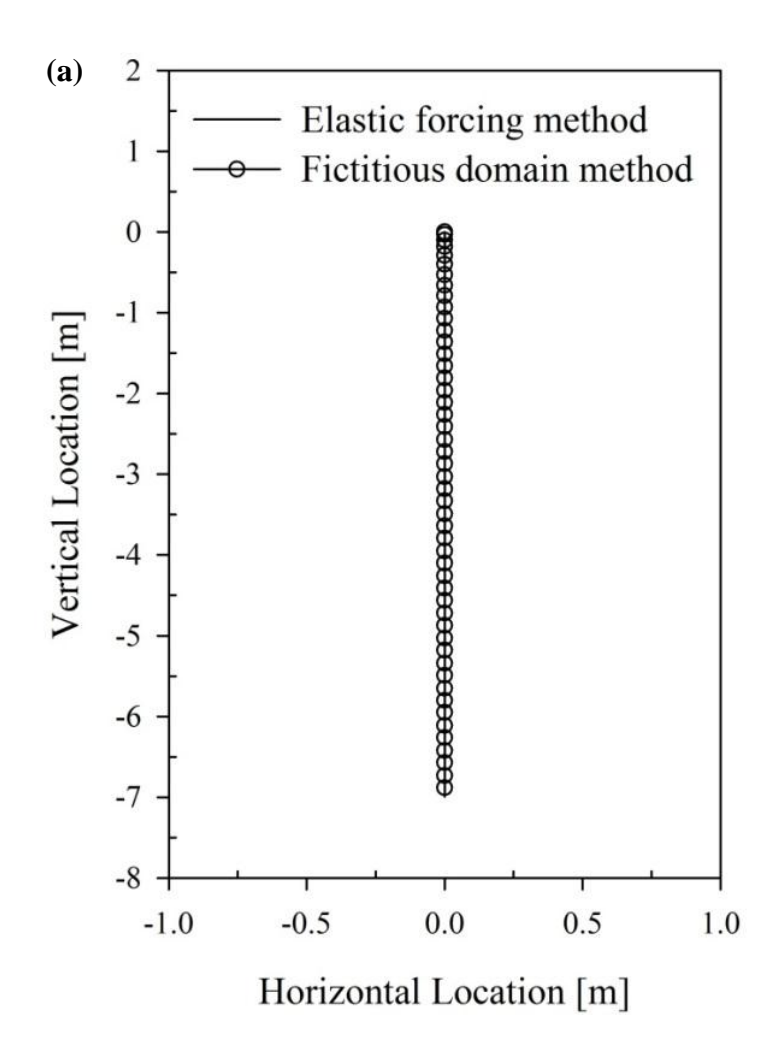
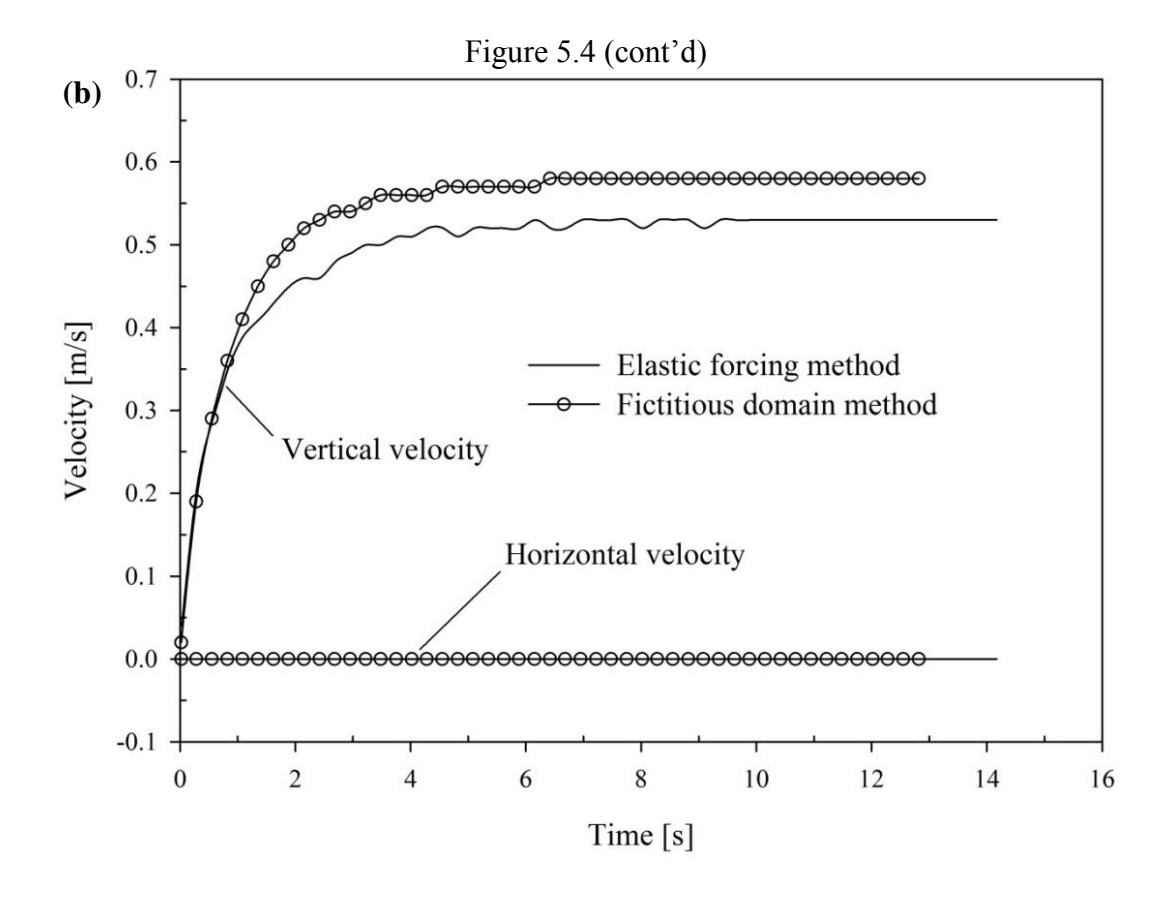


Figure 5.4: Comparison of (a) disc position and (b) disc velocity between the elastic forcing method and the fictitious domain method shows that both methods are numerically symmetric in estimating the terminal velocity of a disc falling in a flow with small Reynolds number (Re=10 for the fictitious domain method).



(b) Particles Drafting-Kissing-Tumbling

In this section, two discs settling under gravity are modeled via the fictitious domain method based on the MacComack scheme. The discs are with an identical size d_p =0.2m. The density ratio of the discs and the flow ρ_p / ρ_f is 1.5. The flow viscosity is μ =0.01kg/m s. At t=0s, Disc 1 is located at the original point of the computational domain [-12d_p, 12d_p] × [-7d_p, 65d_p]. The mesh size for this case is 240×720. The center of Disc 2 is located 2d_p below the center of Disc 1. When t>0s, two discs are released simultaneously under the gravity g= (0, -9.8m/s²).

Fig. 5.5 shows the velocity contour when two discs are falling under gravity. When a disc is settling, a low pressure wake is generated behind the disc. If another disc is caught in this zone, the disc could speed up due to the reduced drag force. This phenomenon is referred to as

"drafting". In Fig. 5.5a, Disc 1 is drafting behind Disc 2 at t=2.25s. The velocity of Disc 1 (u_{c1} = 0.78m/s) is larger than the velocity of Disc 2 (u_{c2} = 0.70m/s). Two discs are drafting for a while until the lagging disc catches up with the lead one, called "kissing" shown in Fig. 5.5b. In Fig. 5.5b, two kissing discs travel as a single long body in a position parallel to the flow at an identical velocity (u_{c1} = u_{c2} = 0.97m/s). The long body is not stable traveling at this position which would tumble to a position perpendicular to the flow stream (Fig. 5.5c). Two discs are pushed apart until a stable separation distance is established (Fig. 5.5d). The above phenomena obtained from the numerical results are consistent with the observation in the experiment conducted by Joseph et al. (1987).

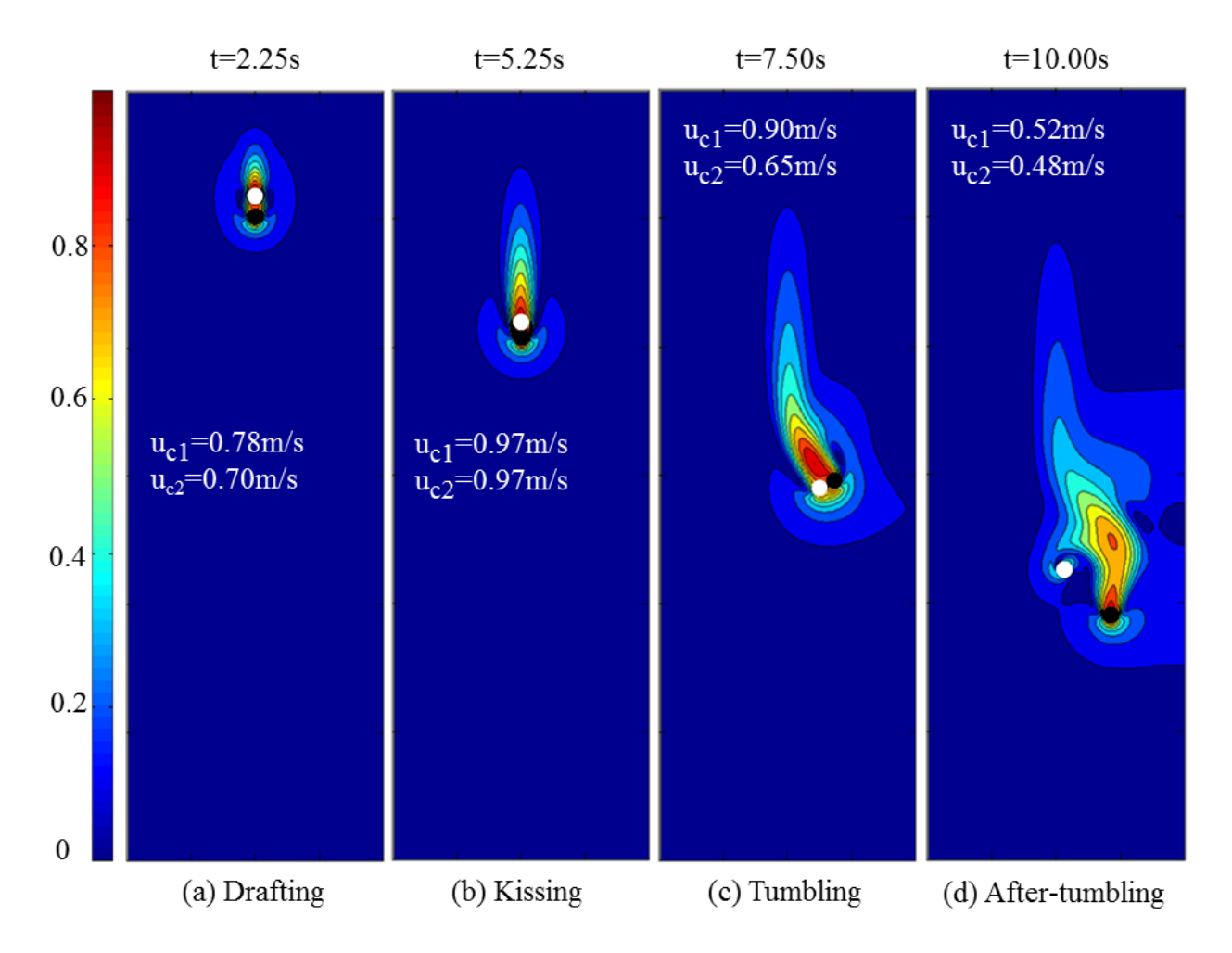


Figure 5.5: Schematic demonstration of two particles (a) drafting, (b) kissing, (c) tumbling and (d) being apart after tumbling.

(c) Particles settling in a sealed container

240 circular particles settling in a sealed container under gravity is investigated using the fictitious domain method based on the MacCormack scheme. The collision scheme is used to avoid collision among the particles and between a particle and the container wall. Fig. 5.6 shows the velocity vector and the particle position at time t=0s, t=2.5s, t=5s, t=7s, t=10s, and t=20s, respectively. The diameter d_p of all the particles is 0.2. The density ratio of the particle and the

fluid flow ρ_p/ρ_f equals to 2. The flow viscosity μ is 0.0075. In Fig. 5.6a, the discs are initially located on the top of a square container with [24.2d_p 24.2d_p] in dimension. For a sealed container, the no-slip boundary condition is enforced on all four bounds. The Eulerian mesh size h uses 1/20d so that there are 20 grids across each particle. The gap between two particles is 3h. The mesh grids for the computational domain in the x direction and y direction is 484×484. At t=0s, the particles at the bottom are marked in red to highlight the interface between two phases. When t>0s, the particles are settling under the gravity. Since the light phase is located at the bottom of the computational domain, the heavy particles on the top are pushed by flow which causes interface instability. This phenomenon was referred to as Rayleigh-Taylor instability

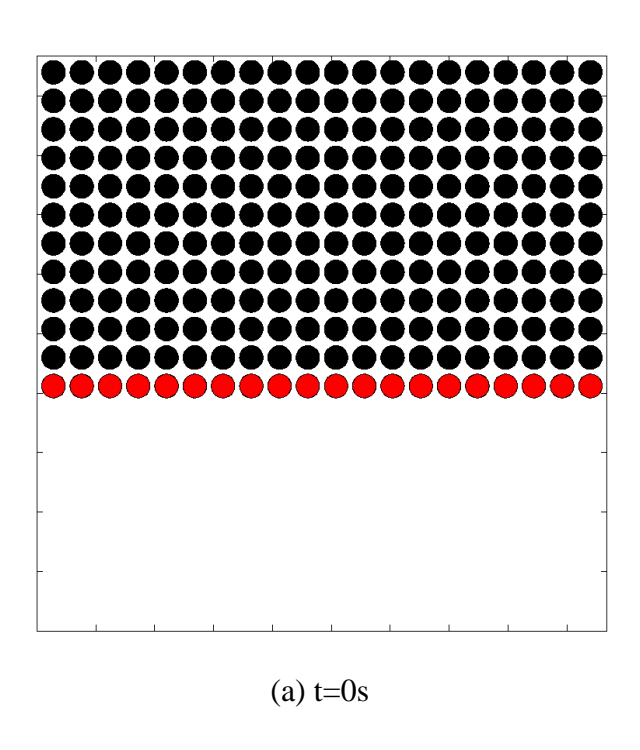
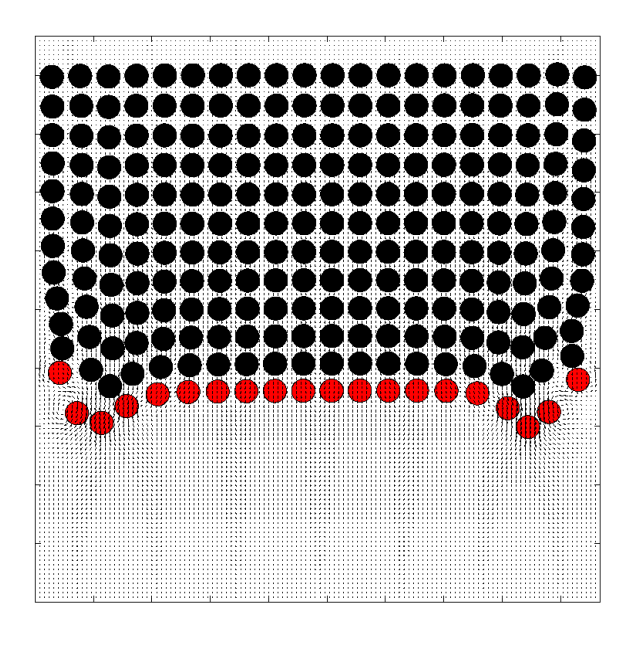
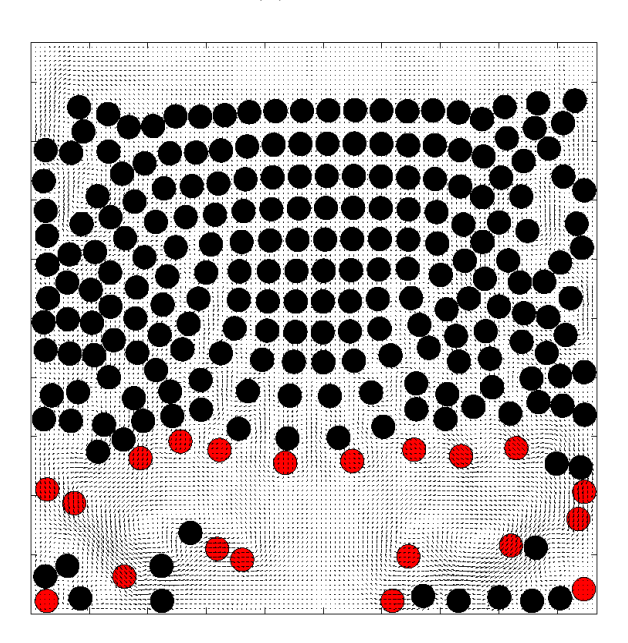


Figure 5.6: Schematic demonstration of 240 particles doing sedimentation under gravity in a sealed container at (a) t=0s, (b) t=2.5s, (c) t=5s, (d) t=7s, and (e) t=20s.

Figure 5.6 (cont'd)

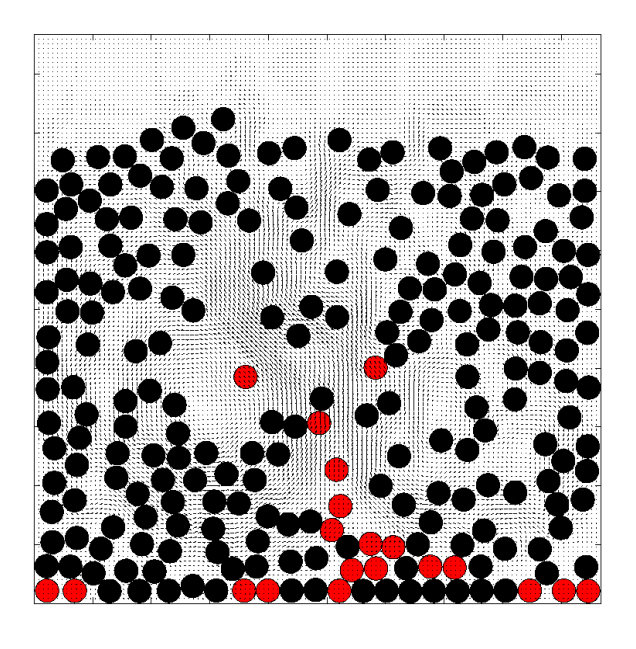


(b) t=2.5s

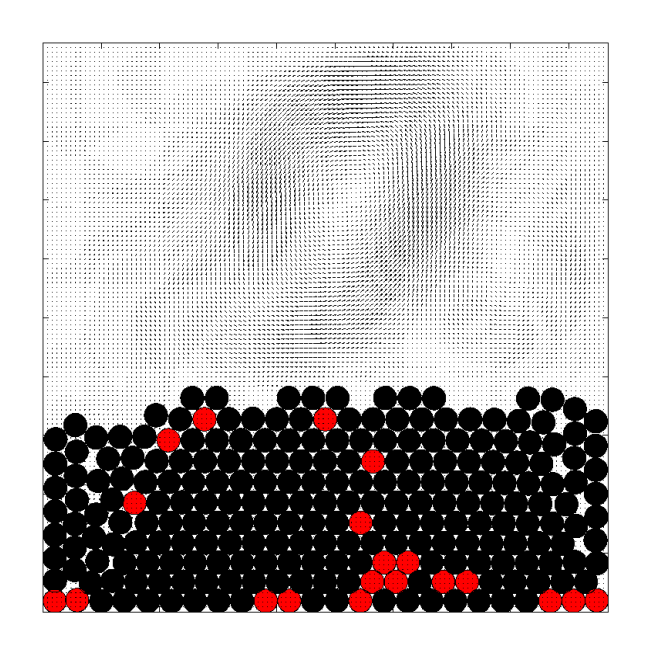


(c) t=5s

Figure 5.6 (cont'd)



(d) t=7s



(e) t=20s

(Sharp, D. H. 1984). Fig. 5.6b shows the interface is distorted due to Rayleigh-Taylor instability at t=2.5s. The interface instability keeps growing with two vortices generated close to the wall pulling down the particles on the sides. These two vortices develop with time and push those particles around the container center upward (Fig. 5.6c - d). Finally, a stable state is achieved when all the particles settle down at the bottom of the container (Fig. 5.6e).

5.3.3 Particle behavior

(a) Single elliptical fiber

Jeffery (1922) solved the translation and rotation of a neutrally buoyant ellipsoid in a shear Stokes flow. The case is used here to validate the present scheme in a 2-D scenario. Consider an elliptical disc located at the center of a square domain [L L] in Fig. 5.7. The elliptical disc has the aspect ratio r_e =1.5. The angle between the major axis and the horizontal direction is ϕ = π /2. The wall on the top is moving to the right with the velocity U_w =1 while the wall at the bottom is moving to the left with the same velocity. The shear rate is $\dot{\gamma}$ =0.4. The particle Reynolds number Re_p for an elliptical disc is defined through an equivalent diameter d_p^e and is obtained by

$$Re_{p} = \frac{\rho U_{w} d_{p}^{e}}{\mu} \tag{5.13}$$

To compare with the Jeffery's solution, simulation of particle Reynolds number equal to 0.4, 4, and 20 are performed. The angular velocity given by Jeffery's solution is

$$\omega_{c}(\phi) = \frac{-\dot{\gamma}}{r_{e}^{2} + 1} (r_{e}^{2} \sin^{2} \phi + \cos^{2} \phi)$$
 (5.14)

The period is obtained from

$$T = \frac{2\pi}{\dot{\gamma}} \left(\frac{r_e^2 + 1}{r_e} \right) \tag{5.15}$$

Fig. 5.8 shows the comparison of the angular velocity and the corresponding period between the DNS method and Jeffery's analytical solution. The angular velocity $\omega_c(\phi)$ is plotted against the angle ϕ . The negative sign indicates that the particle is rotating clockwise. When $Re_p=0.4$, the curve of the DNS data matches exactly that of Jeffery's solution. The difference of the period between two methods is marginal with 0.01s. This indicates that the fictitious domain method based on the MacCormack scheme is accurate. It can also be concluded that the flow with $Re_p=0.4$ is small enough to be treated as a Stokes flow. The DNS method underestimates the angular velocity for the cases $Re_p=4$ and $Re_p=20$, which leads to a longer period time. Jeffery's solution was derived based on Stokes flow ($Re_p\ll1$) and thus cannot handle flow with a large Re_p .

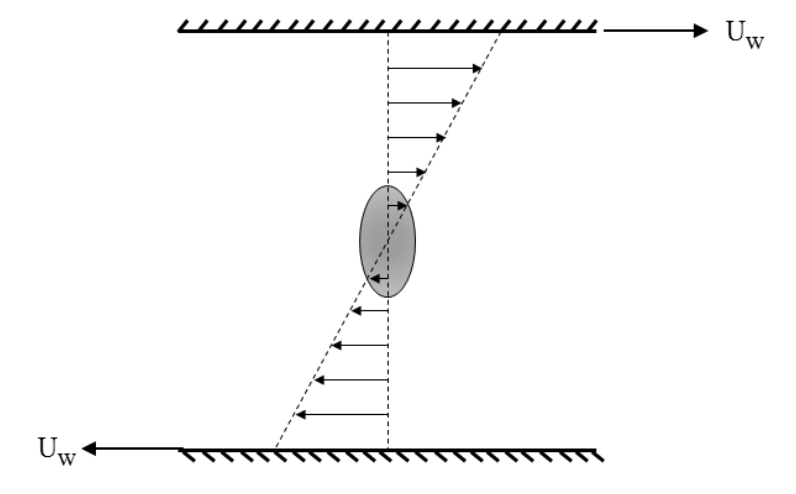


Figure 5.7: Schematic of computational domain for a neutrally buoyant elliptical disc moving in a Stokes shear flow.

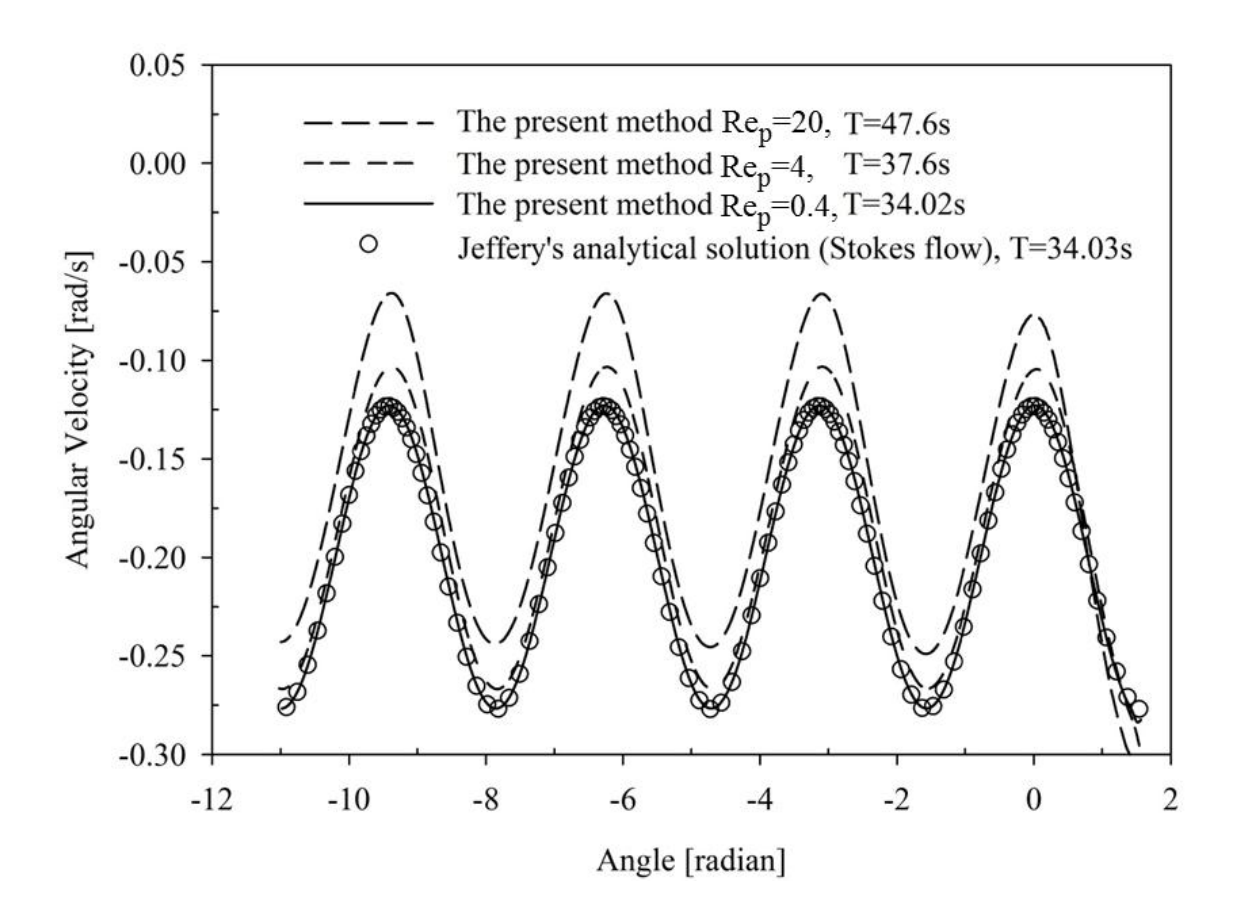


Figure 5.8: Comparison of results from the DNS method for different Re_p and Jeffery's solution shows that the angular velocity and the period are well predicted by the present DNS scheme for Re_p =0.4.

(b) Particle migration

One important phenomenon that could cause non-uniform distribution of a uniform suspension flow is particle moving across streamlines, referred to as particle migration. The phenomenon could be resulted from the effects of fluid inertia, particle inertia, particle-particle interaction, and particle Brownian motion. The effect of particle inertia was discussed in Chapter 2 and Chapter 3. The Brownian motion can be ignored as the size studied in this work is sufficiently large. Research of interest in this section focuses on neutrally buoyant particle

migration induced by fluid inertia. A neutrally buoyant particle is a particle in a condition that its density is equal to the density of the flow in which it is immersed.

Fig. 5.9 shows the computational domain and the initial location of a neutrally buoyant particle in a Couette flow. The boundary condition for the top and the bottom bounds are walls moving with U_w=7 in the opposition directions. The flow Reynolds number Re is 700. The minor radius of the disc ae is 0.1. The aspect ratio re is equal to 1.5. The particle density and the fluid density equal to 1. The effect of the particle size is investigated by using larger minor radiuses equal to $1.5a_e$ and $2a_e$. A circular disc with the equivalent diameter $d_p^{\ e}$ of the elliptical disc is also used to study the effect of the particle shape on the particle location. $d_p^{\ e}$ is the diameter when the area of the circular disc is equal to the area of the elliptical disc with a_e. Fig. 5.10 plots the dimensionless vertical location (y/L₂) with the dimensionless time (t U_w/L₂) for comparison. The non-dimensional centerline is located at 0.5. The curves show that all the particles would move to the centerline of the shear flow eventually regardless of the size and the shape of the particles. The curve of the circular disc with d_p^e is close to that of the elliptical disc which may indicate that the shape effect could be ignored if an equivalent diameter of an elliptical disc is used for a circular particle. Result also shows that the elliptical discs with a larger minor radius are faster to reach the equilibrium location as a faster angular velocity is obtained for a larger particle under a simple shear flow. Rubinow & Keller (1961) claimed that the lateral force (lift force) is function of the angular velocity.

Fig. 5.11 shows the configuration of the computational domain for a single particle moving in a Poiseuille flow. A periodic boundary condition is used for the left and the right bounds. A

pressure gradient is imposed on the domain which could generate a flow with Re=700. The noslip boundary condition is used to the top and the bottom bounds. Simulations are run for particles with the same shape and size as the last case. It can be seen from the curves in Fig. 5.12 that the particles regardless of their shape and size reach the vertical location around 0.2 which is 60% of the distance from the centerline of the flow to the bottom wall. This result is consistent with the observation in experiment of Segré & Silberberg (1962a,b) who stated that, for undisturbed flow, lateral migration of a neutrally buoyant sphere induced by fluid inertia can finally attain an equilibrium location about 60% from the centerline to the wall in a Poiseuille flow. The establishment of the equilibrium position is likely due to the balance between the lubrication force from the wall and the lift force induced by the fluid inertia. Autal et al. (1991) stated that when a rigid body is moving close to the wall, the lubrication force is inversely proportional to the distance between the body and the wall. Unlike the shear flow, the plot shows that the vertical location the particle is fluctuating around the equilibrium location in the pressure-driven flow, which indicates that the lift force induced by the fluid inertia and the lubrication force is fighting back and forth to find a balance.

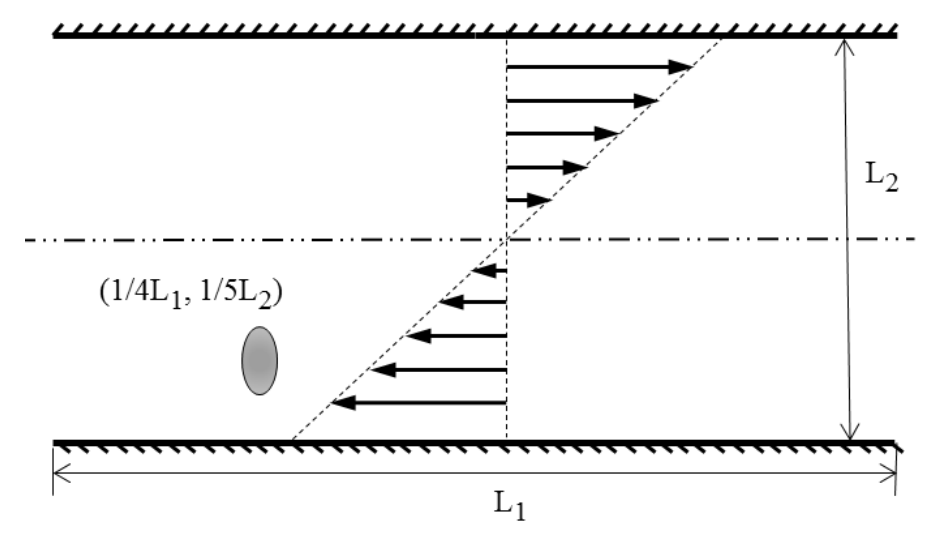


Figure 5.9: Schematic of the computational domain dimension [L_1 L_2] and the initial location of an elliptical disc located at (1/4 L_1 , 1/5 L_2) in a Couette flow with Re=700.

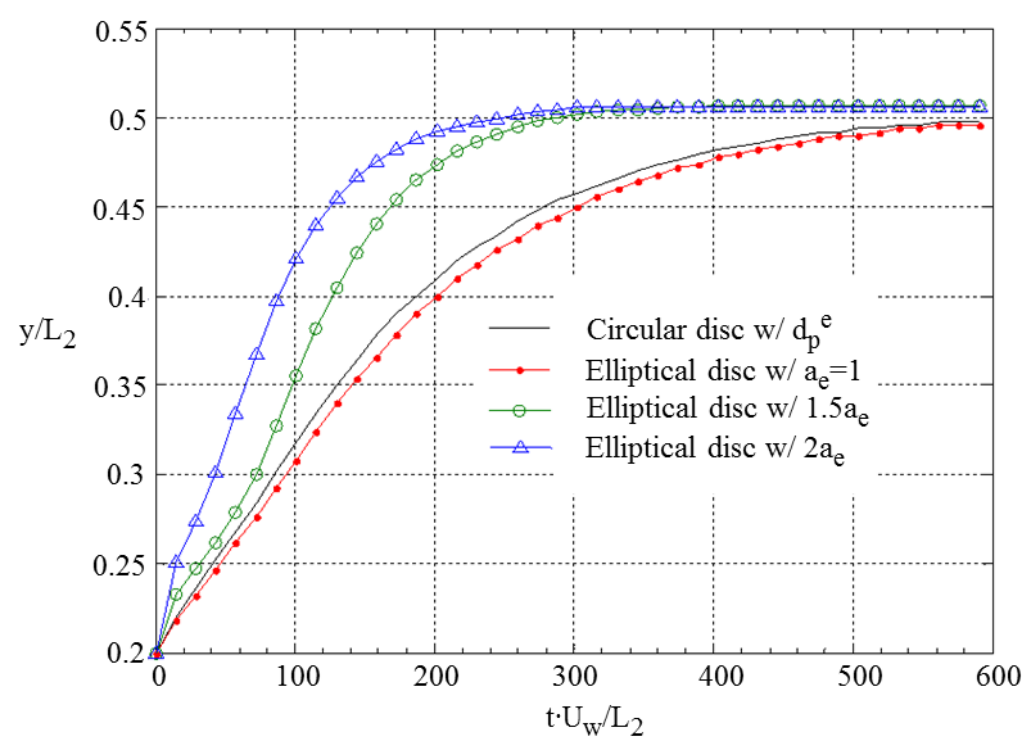


Figure 5.10: Comparison of the particle location changing with time in the vertical direction shows that particles attain the centerline in a Couette flow regardless of the size and shape of a particle

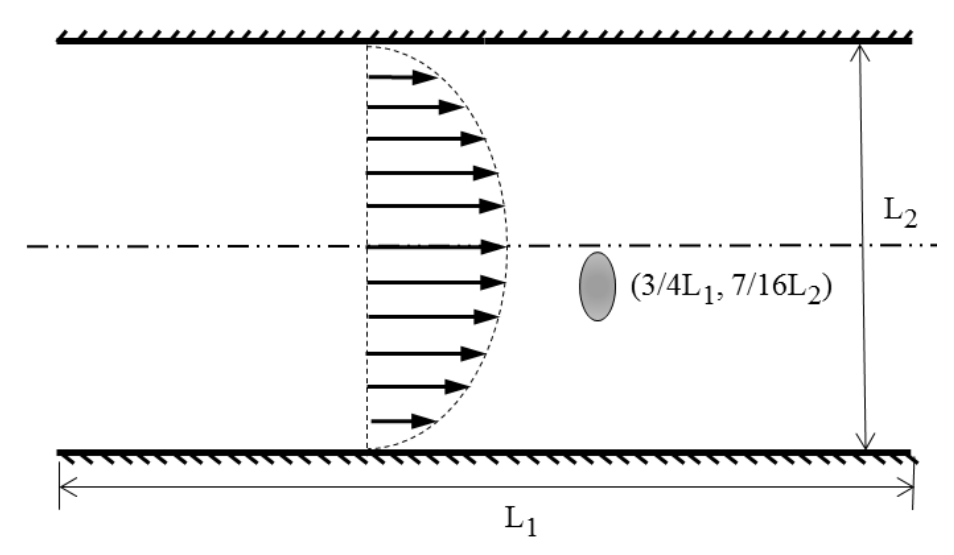


Figure 5.11: Schematic of the computational domain dimension [L_1 L_2] and the initial location of an elliptical disc located at (1/4 L_1 , 7/16 L_2) in a Poiseuille flow with Re=700.

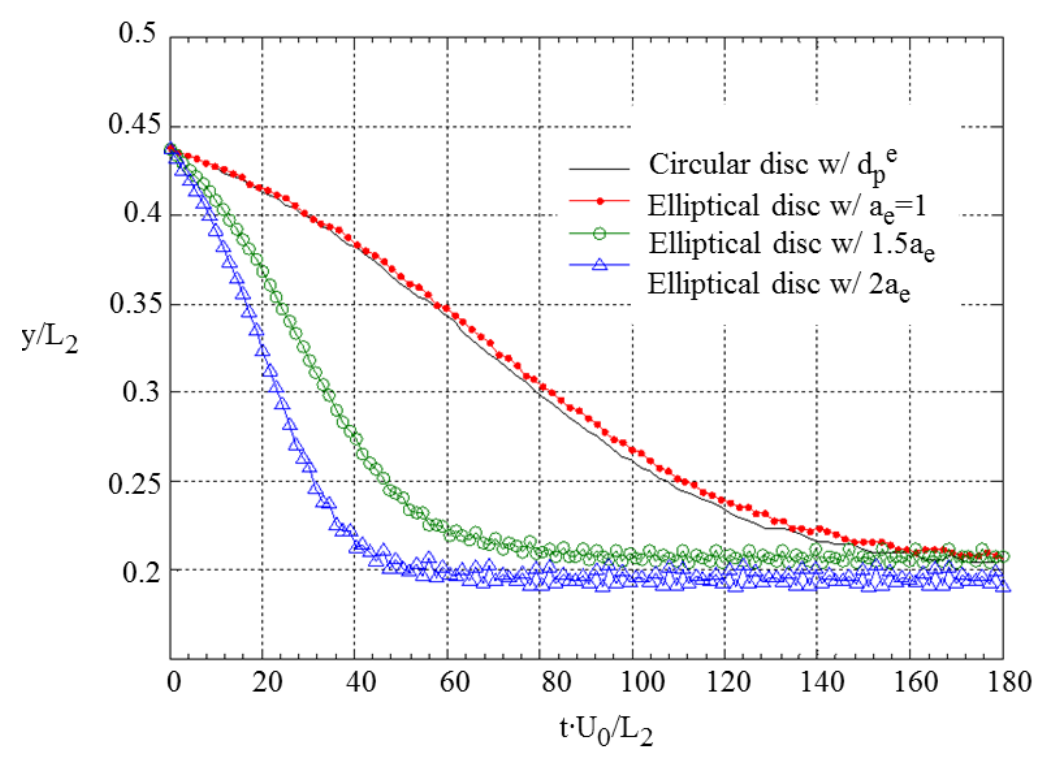


Figure 5.12: Comparison of the particle location changing with time in the vertical direction shows that particles attain approximately the location 60% from the centerline to the wall in a Poiseuille flow regardless of the size and shape of a particle.

Fig. 5.13 shows the velocity contour and the concentration distribution of a uniform particulate-laden flow changing with time in a Couette flow. At t=0s, elliptical particles are uniformly distributed in the flow domain. The flow is dilute with the volume fraction $\alpha_p\!\!=\!\!10\%$. Monodisperse particles are used with the minor radius $a_e=0.1$ and an aspect ratio equal to 1.5. The computational domain is square with the mesh size 250×250 . The Reynolds number Re is equal to 700. Fig. 5.13b shows that although the particles are moving with a different translational velocity along an arbitrary vertical cross-section, all the particles are rotating with an identical angular velocity caused by the single shear rate of a Couette flow. In Fig. 5.13c, the plot shows that the particles are moving toward the centerline due to the phenomenon of particle migration across streamlines. This leads to high concentration at the flow center. In Fig. 5.13d-e, due to the high concentration at the flow center, interaction between the elliptical particles becomes outstanding. It can be seen that both the velocity profile and the particle concentration are affected by particle-particle interaction. Finally, Fig. 5.13f shows that the flow forms clusters. It can be seen from those particles marked in the white circles that certain part of the particles overlap, which indicates that the collision scheme designed for body in spherical shape is not working properly for ellipsoids.

Fig. 5.14a shows the velocity contour and the concentration distribution of a uniform particulate-laden flow changing with time in a Poiseuille flow. The particles in the pressure-driven flow act totally differently from those in the shear flow. Since a Poiseuille flow possesses a parabolic flow pattern, along an arbitrary vertical cross-section the particles are rotating in a different angular velocity due to the non-uniform shear rate. Moreover, the particles in the upper half part of the domain are rotating in an opposite direction of those in the lower half shown as in Fig. 5.14b. Due to particle migration in the Poiseuille flow, most particles are moving toward the

wall (Fig. 5.14c-e) except for those located at the centerline. The particles at the centerline encounter shear in both directions. They stick near the centerline for a long time before they fall into the either side of the centerline and move toward the wall. Eventually, all the particles concentrate somewhere between the centerline and the walls. Fig 5.14f shows that the particles are clustering which forms larger structures near the wall.

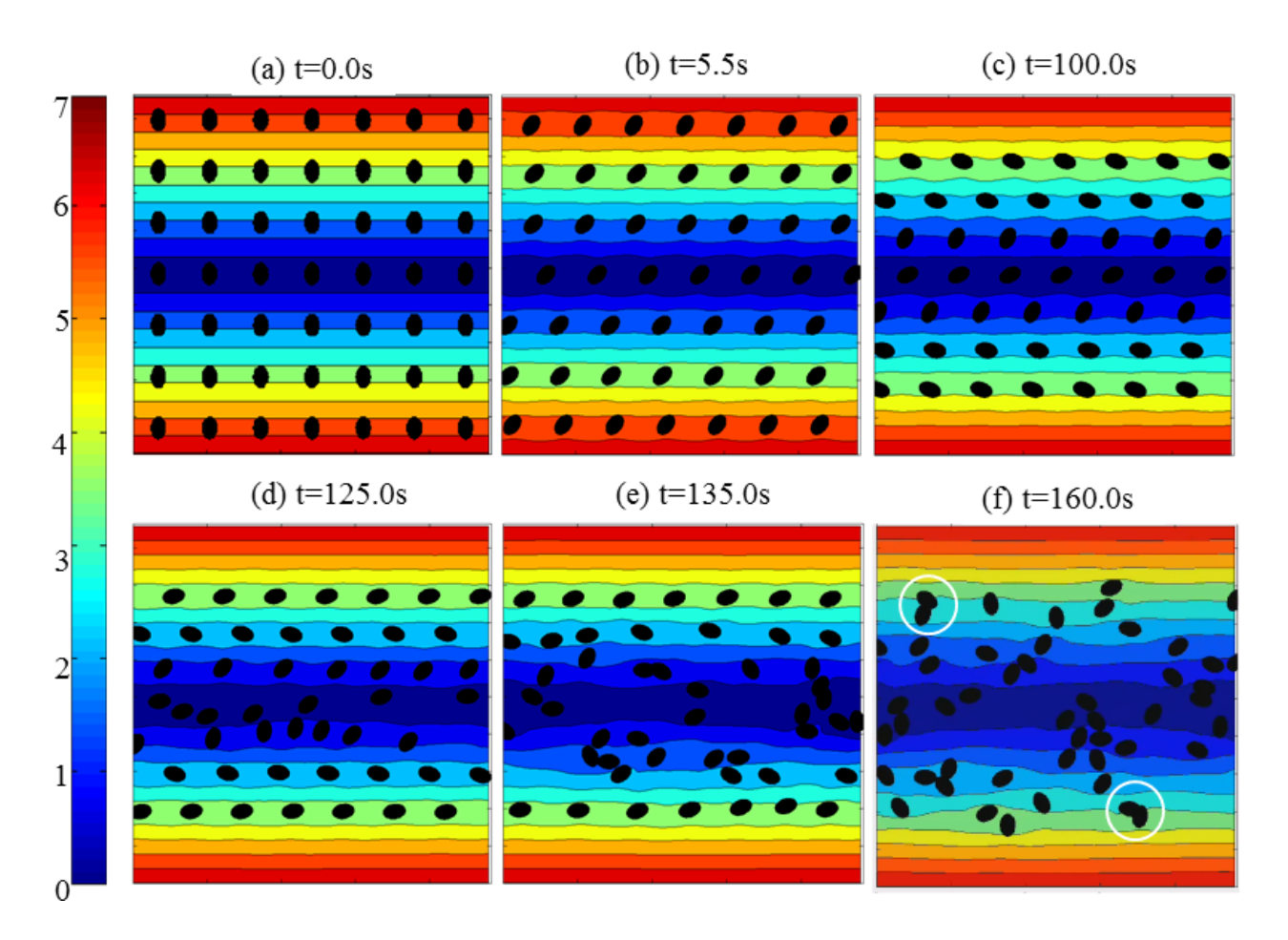


Figure 5.13: Schematic demonstration of the velocity contour and the concentration distribution of a uniform particulate-laden flow with α_p =10% in a Couette flow at t=0s, 5.5s, 100s, 125s, 135s and 160s.

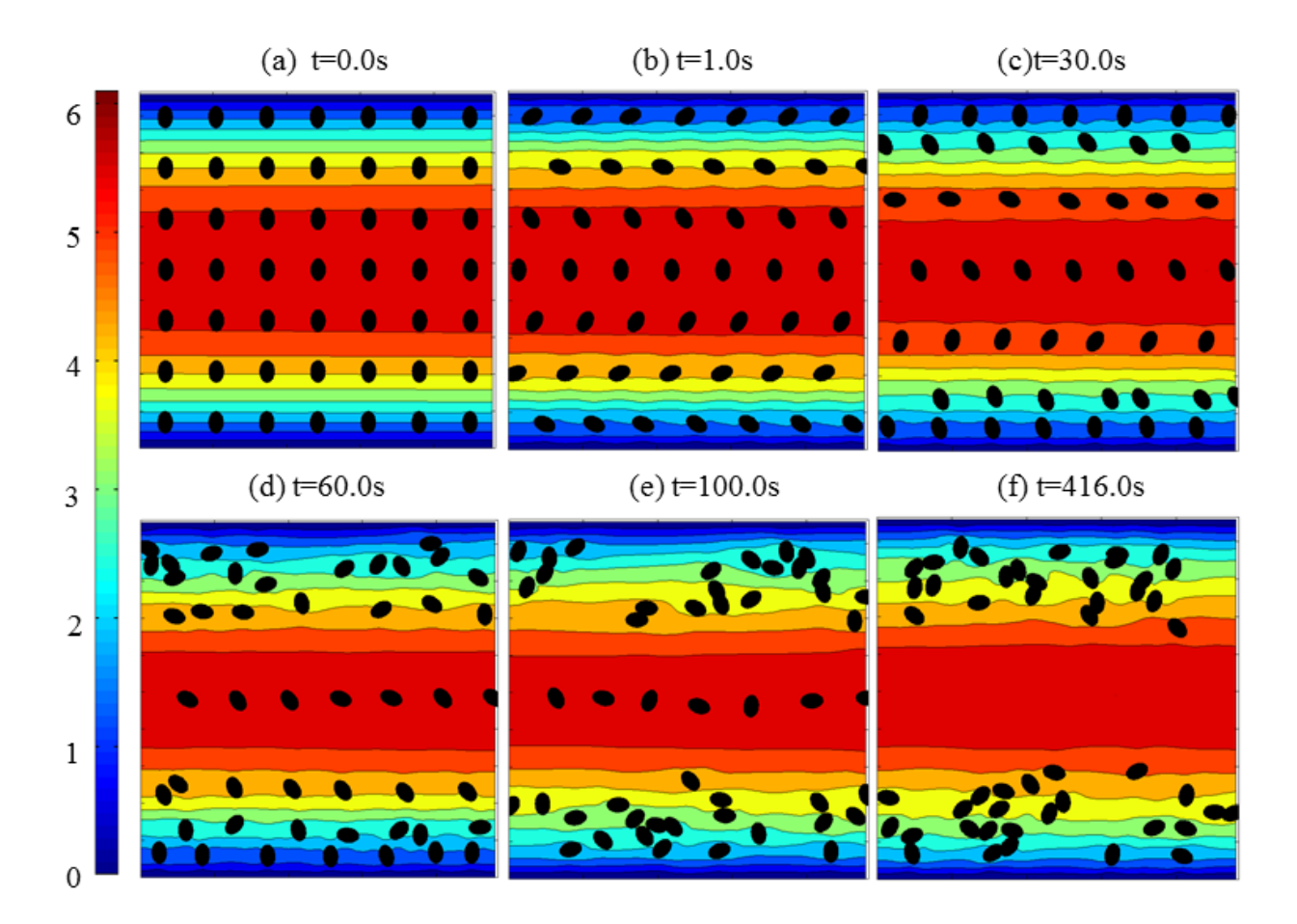


Figure 5.14: Schematic demonstration of the velocity contour and the concentration distribution of a uniform particulate-laden flow with α_p =10% in a Poiseuille flow at t=0s, 1s, 30s, 60s, 100s and 416.0 s

5.4 Validation of the mixture model in FLUENT

Based on the above study, the numerical approach, fictitious domain method with the MacCormack scheme, is accurate in predicting particle behavior in a viscous flow. The result can be used as a reliable reference to validate the mixture model in FLUENT. In this section, particulate-laden flows with a non-uniform concentration and a uniform concentration are investigated. Focus is put on the performance of the mixture model on predicting the concentration distribution of neutrally buoyant particles under a simple shear flow.

5.4.1 Transport of a non-uniform shear flow

Fig. 5.15 shows the initial concentration distribution of the disperse phase in the computational domain of [3 1]. The mesh size uses 750×250 in two methods. Both the carrier phase and the disperse phase are at rest at t=0s. The disperse phase concentrates in a square domain with the volume fraction α_p equal to 46%. The color in Fig. 5.15a shows the phase distribution. Red means the region for the highest concentration and blue indicates the location with zero concentration of the disperse phase. The disperse phase is neutrally buoyant and has an identical density as the carrier phase ($\rho_p = \rho_f = 1$). The wall on the top is moving to the right with the velocity $U_w=1$ while on the bottom is moving to the left with the same velocity. A periodical boundary condition is imposed on the left and the right bounds. The flow is within the laminar regime with Re=100.

Fig. 5.16 shows the comparison of the disperse phase distribution at t=10s. The concentration predicted by the mixture model is similar to the result from DNS. Under the shear, the square shape distribution is changed. It can be seen that the disperse phase closer to the wall is moving faster due to a higher flow velocity. In Fig. 5.16b, the edge on four corners becomes blurry with a lighter color which indicates a lower concentration at those places. This distribution is consistent with the result in Fig. 5.16a, showing as a longer distance among the particles on four corners. In Fig. 5.17, the distribution is stretched by the flow and forms a stripe at t=25s. Due to the periodic boundary condition, the disperse phase that passes the right bound will enter the left bound and vice versa. At t=50s, Fig. 5.18b shows that the concentrated disperse phase is stretched further with five stripes. The concentration is higher close to the centerline due to

slower velocity at the center. This distribution predicted by the mixture model is consistent qualitatively with the result by the fictitious domain method shown in Fig.5.18a.

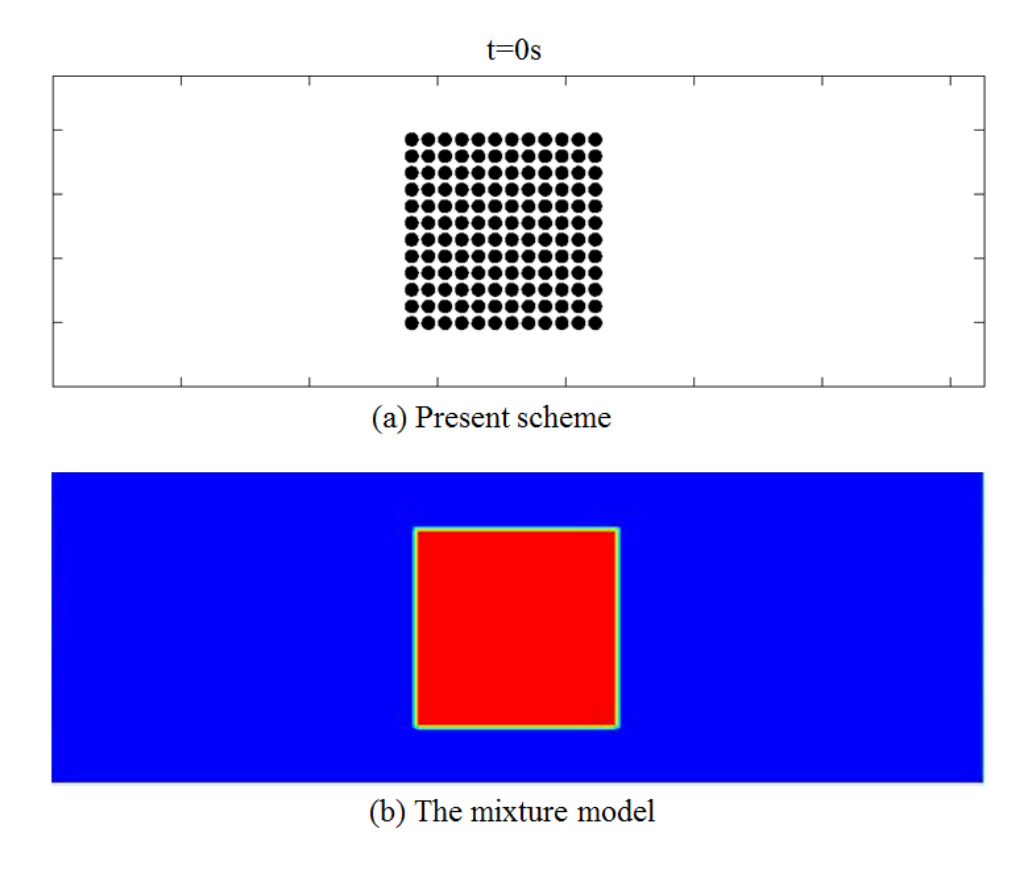


Figure 5.15: Initial condition shows the concentration of the dispersed phase in the computational domain for (a) the present scheme (b) the mixture model

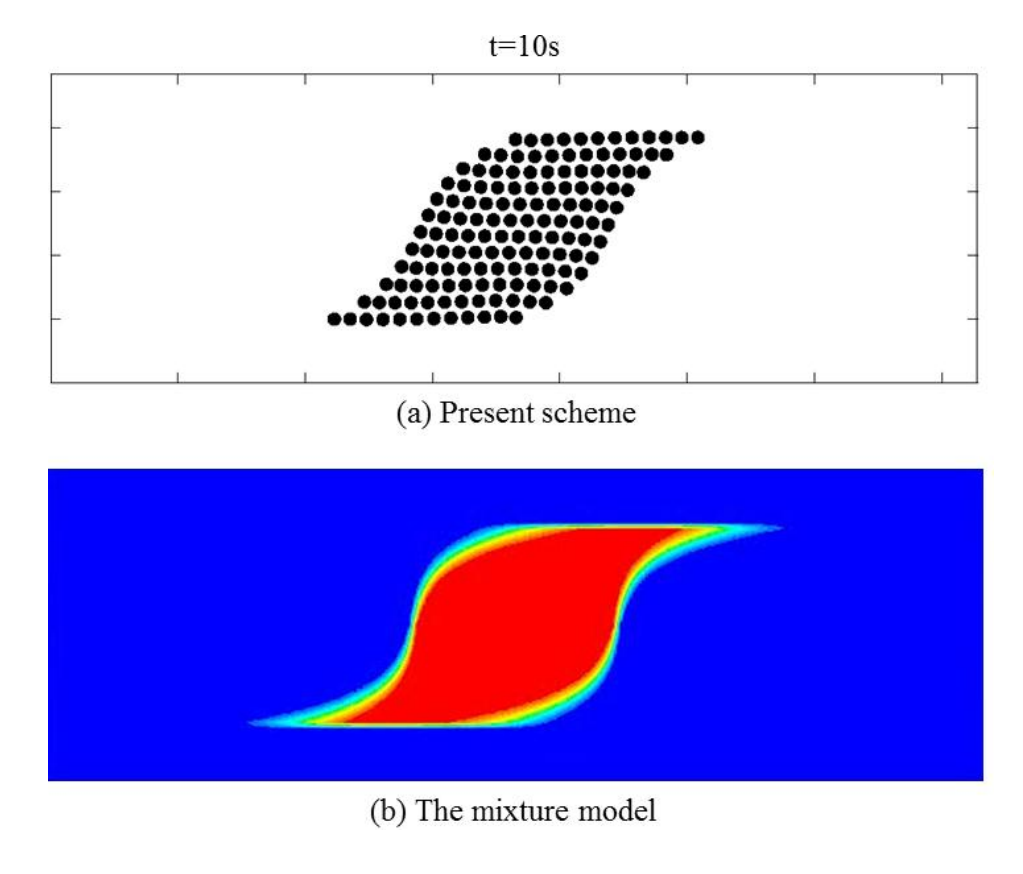


Figure 5.16: Comparison of the concentration of the dispersed phase at t=10s for (a) the present scheme (b) the mixture model

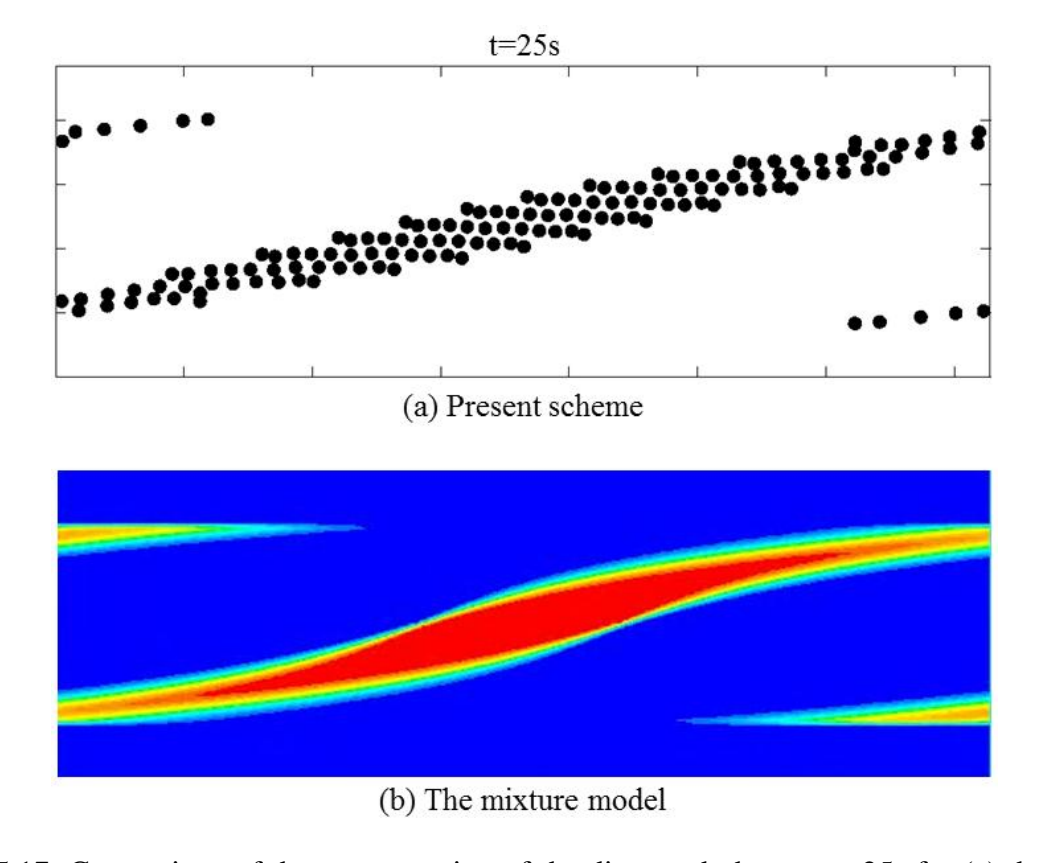


Figure 5.17: Comparison of the concentration of the dispersed phase at t=25s for (a) the present scheme (b) the mixture model

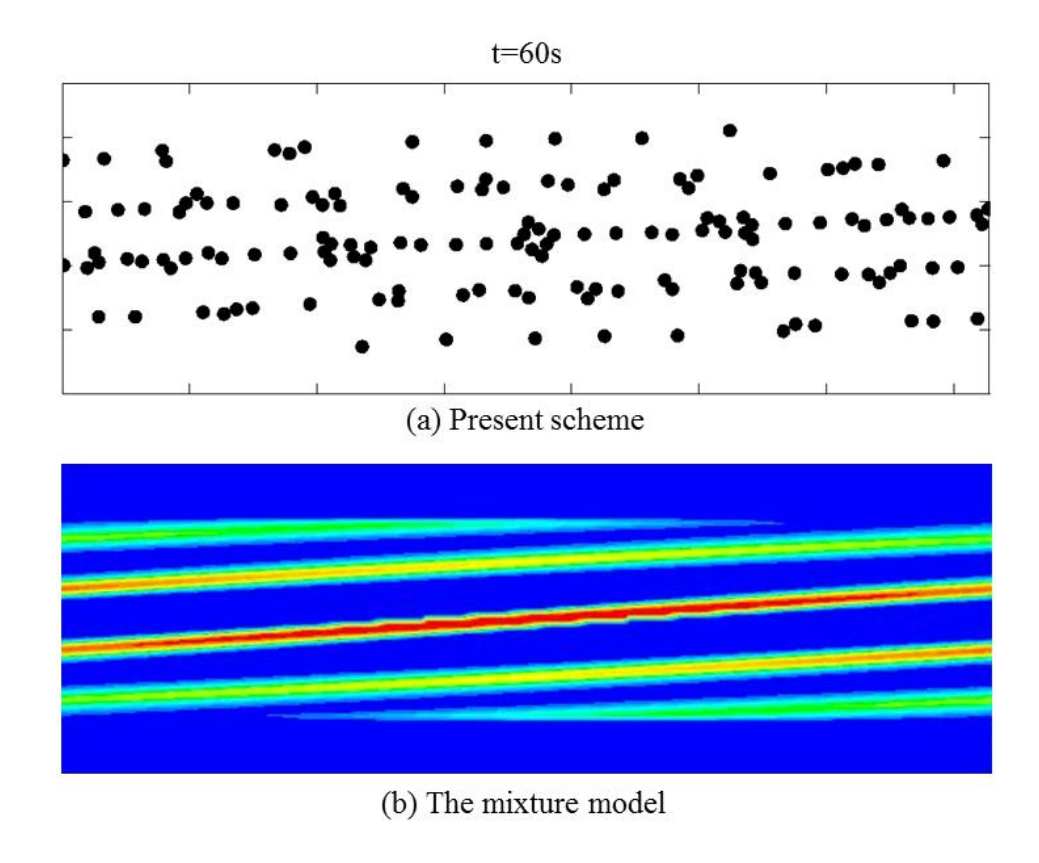


Figure 5.18: Comparison of the concentration of the dispersed phase at t=60s for (a) the present scheme (b) the mixture model

5.4.2 Transport of a uniform unidirectional flow

To validate the performance of the mixture model in transporting a uniform shear flow, simulations are run for a uniform particulate-laden flow in a Couette flow and a Poieuille flow. Fig. 5.19 shows a square domain [L L] in which neutrally buoyant particles are uniformly distributed. The volume fraction α_p is 10%. The mesh size uses 250×250. For the Couette flow, two walls are moving at a velocity U_w =7, the Reynolds number is 700. Fig. 5.20 shows the comparison of volume fraction distribution along an arbitrary vertical cross-section between the fictitious method based on the MacCormack scheme and the mixture model at t=50s and t=100s. The horizontal axis is a dimensionless location (y/L) and the vertical axis is the flow volume

fraction. Since the flow is symmetric to the centerline, only half of the line is plotted for simplicity. Result from the present scheme shows that at t=50s, the maximum flow concentration is 16.5% located at 0.2. At t=100s, a higher concentration is observed equal to 19%. The location for maximum concentration is moved from 0.2 to 0.4 which is closer to the centerline (0.5). On the other hand, the result shows that the distribution predicted by the mixture model stay at 10% along the cross-section which indicates that the model is not able to predict the distribution correctly. Fig. 5.21 shows the comparison of the flow volume fraction between two methods for the Poiseuille flow with Re=700. Result from the present scheme at t=20s and t=40s shows that the flow concentration becomes lower close to the centerline (0.5) and higher close to the wall (0.0). Same conclusion can be draw from the curves that the mixture model is not able to predict the phenomenon of disperse phase across streamline due to fluid inertia. The mixture model considers the impact of the disperse phase in a momentum term contributed by the slip velocity. We know from Chapter 3 that the slip velocity is the velocity between two phases which needs to be closed by model. The only model in ANSYS FLUENT 12 is called the algebraic slip model by Ishii (1975) (Eq. 3.16). It can be seen from the equation that the effect of the lateral force generated due to fluid inertia is not included in the equation which cause the model fail to predict the phenomenon studied in this work.

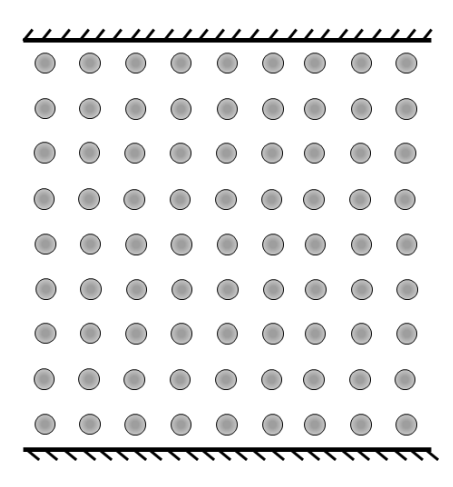


Figure 5.19: Schematic of the computational domain for a uniform flow with $\alpha_p\!\!=\!\!10\%$.

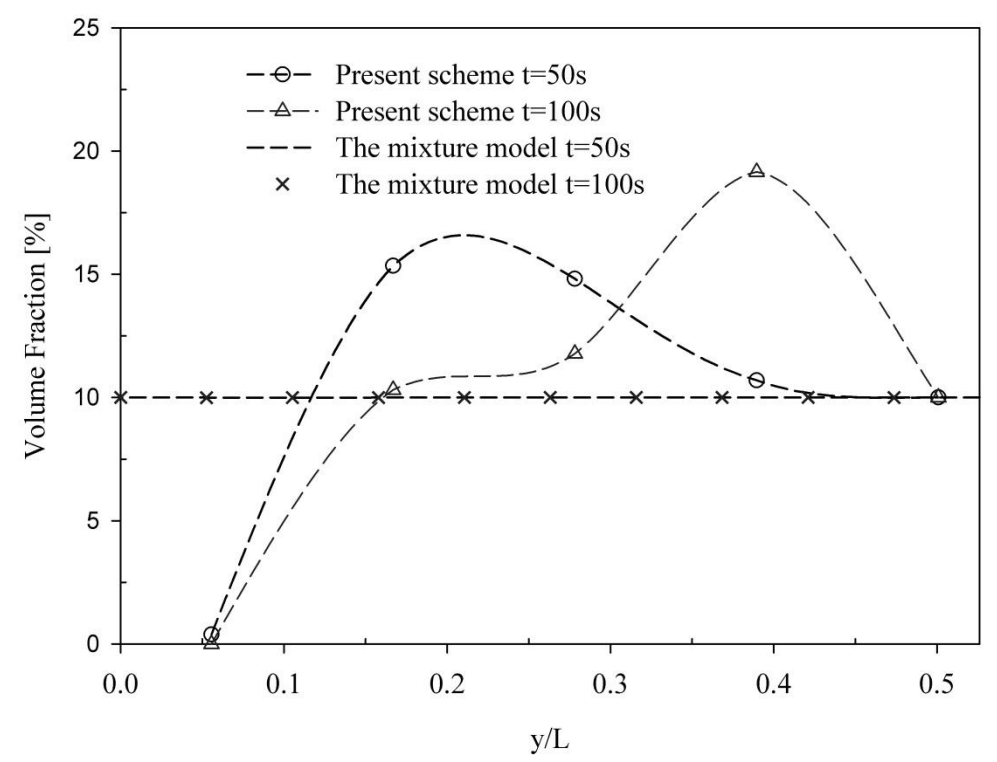


Figure 5.20: Comparison of volume fraction distribution along a vertical cross-section between two methods at t=50s and t=100s shows that the mixture model fails to predict a higher concentration near the center for a uniform particulate-laden shear flow.

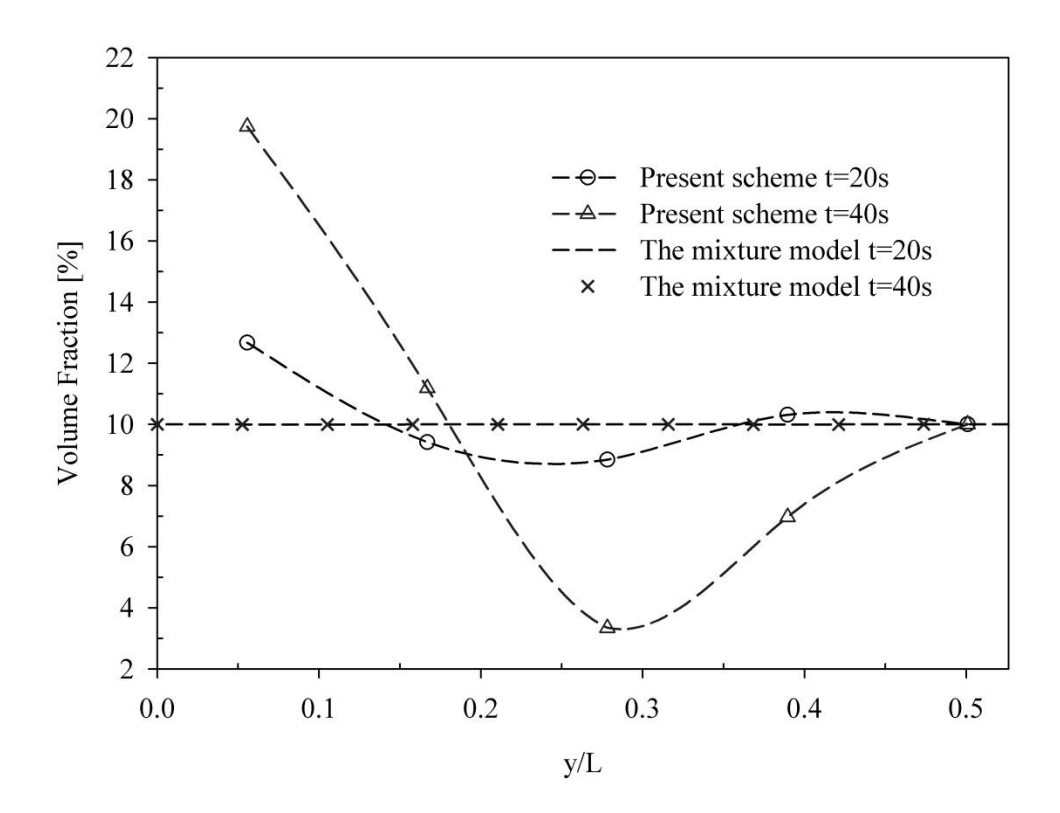


Figure 5.21: Comparison of volume fraction distribution along a vertical cross-section between two methods at t=20s and t=40s shows that the mixture model fails to predict a higher concentration close to the wall for a uniform particulate-laden pressure-driven flow (Re=700).

5.5 Summary

To improve the stability and accuracy of using the immersed boundary method for rigid structures immersed in a fluid flow, the fictitious domain method was used. The technique was combined with the MacCormack solver to simulate a flow passing a stationary rigid cylinder. Result shows that the method is accurate in estimating the drag coefficient. Later, the method, combined with a collision scheme, was applied to particulate-laden flow simulation. Result shows that the terminal velocity of a single particle settling was well predicted by the numerical method. In addition, compared to the elastic forcing method, the present method is more suitable for a movable rigid body since it can tackle flow with a higher Reynolds number. Result also

indicates that the present method can capture two particles DKT (drafting-kissing-tumbling) and the phenomenon of Rayleigh-Taylor instability at two phase interface. Subsequently, the method was used to study the behavior of a neutrally buoyant particle in both Couette flow and Poiseuille flow. Result shows that for a Couette flow, the particle would move toward the centerline while for a Poiseuille flow, the particle would finally attain an equilibrium location that is 60% of the distance from the centerline to the wall. Finally, the numerical approach was employed to validate the mixture model in predicting the disperse phase concentration in a simple shear flow and a pressure-driven flow. It can be concluded from the result that the mixture model is not able to predict the concentration distribution correctly. To predict the phenomenon, the constitutive equation used in the mixture model to close the slip velocity should include the effect of the lateral force induced by fluid inertia.

CHAPTER 6

SUMMARY, CONCLUSIONS, AND RECOMMENDATIONS

6.1 Summary and Conclusions

The work in this dissertation can be divided into two parts. The first part uses CFD modeling to study turbulent particulate-laden flows passing through curved pipes. The one-way coupling DPM in FLUENT is used for dilute flow with a low mass loading. The study focuses on the performance of the turbulent closures based on the RANS equation with different near-wall treatments on estimating the pressure drop and the particle deposition efficiency in bends. The effects of the particle Stokes number as well as the bend configuration, including the bend angle, the bend curvature ratio, and the bend diameter, are investigated. For dilute flows with a high mass loading, the mixture model in FLUENT is employed to study the effect of the disperse phase on the carrier phase. The flow patterns, pressure drop and liquid films are investigated. Bend design is conducted for performance related to pressure drop and deposition efficiency. In the second part, DNS of rigid structures immersed in a viscous fluid are performed at low Reynolds number using the IB method. The elastic forcing method and the fictitious domain method are used to compute the force density term contributed by the immersed structures. The IB method is combined with the explicit MacCormack scheme to solve the fluid equations. The performance is tested in the cases including flow passing a stationary cylinder, particle impinging on a wall, particle sedimentation, and particle behavior in unidirectional flows. Finally, DNS result is used to validate the mixture model in predicting concentration distribution of neutrally buoyant particle flows in a Couette flow and a Poiseuille flow. Important observations associated with these studies are presented below.

Turbulent air flow passing through a curved pipe possesses complicated flow patterns that change with bend configuration and flow Reynolds number. A tight bend with a curvature ratio δ less than 3 is usually associated with a recirculation zone located at the inner bend wall. Flow passing a curved pipe generates secondary vortices and the intensity of these secondary vortices is stronger at the inner wall and can become as high as 35% of the bulk velocity. For flows with a high mass loading, the patterns are significantly affected by the dispersed phase and become even more complex. For example, the disperse phase with a large size would reverse the direction of the secondary vortices or cause multi-pair secondary vortices in a bend cross-section.

When examining the pressure drop of a turbulent air flow through curved pipes, computed results are obtained from different near-wall treatments based on the k- ϵ model and the RSM; all results are close to experimental measurements provided that the mesh meets the y^+ requirement for the wall treatment selected except the local pressure at the outer and inner pipe of the U-bend. For a flow with a high mass loading, the dispersed phase affects the pressure drop significantly. The pressure drop is proportional to the volume fraction of a dispersed phase. Comparison between the numerical results and the empirical models shows the pressure drop estimated by the model agree well with Paliwoda's work. Since the deviation of the pressure drop predicted by different empirical models is large, it is uncertain whether the mixture model is accurate. But it can be concluded that the model predicts results in a reasonable range.

To increase particle deposition, using one-way coupling flow simulations through curved pipes, it was found that one can either decrease the curvature ratio, increase the residence time, or decrease the duct diameter, holding the other two parameters constant. The grade efficiency for this flow is well predicted by the one-way coupling DPM provided that RSM, EWT, and the stochastic model are used. The grade efficiency is found to be related to the particle St number,

the bend angle θ , and the bend curvature ratio δ and can be estimated through the empirical model (Eq. (2.15)) developed in this work. For flows with a high mass loading, the liquid film formed by droplet deposition could be predicted by the mixture model. The film is usually stratified along the outer bend but it can be inversed to the inner bend of a horizontal pipe when the flow is with a very small volume fraction $\alpha_p < 0.0037$. Both the one-way DPM and the mixture model are capable of predicting particles moving across streamlines due to high inertia of a large particle.

As regards DNS of flow interacting with rigid structures, the IB method based on the MacComack scheme appears to be promising. The elastic forcing method is able to capture important physical phenomena qualitatively. In addition, the hydrodynamic force generated by two approaching bodies can be automatically taken care by this method without using a collision scheme. Nevertheless, approximation used in this method of treating a rigid body as a slightly deformable structure may lead to numerical viscosity and instability. The accuracy and the stability of the IB method are improved by using the fictitious domain method. The results accurately match Jeffery's solution in predicting the motion of an ellipsoid in Stokes flow and agree well with the observation in experiment for particle migration in a unidirectional flow. Finally, it can be concluded from the comparison between the DNS method and the mixture model that the latter is not able to correctly predict the concentration distribution of neutrally buoyant particles in a uniform unidirectional flow. To capture the phenomenon, the closure for the slip velocity should be modified to include the effect of the lateral force caused by fluid inertia.

6.2 Recommendations for future work

In the present study, the fictitious domain method with the MacCormack scheme was used to simulate particulate-laden flow and used to validate the mixture model in FLUENT. Suggestions are listed in the following for potential extensions of the present study.

- 1. To avoid collision of two approaching particles, Glowinski's collision scheme is used to provide a repulsive force. The method is designed for rigid spherical bodies. Using an equivalent diameter, one can apply the method to an ellipsoid. This is a good approximation for ellipsoids with a small aspect ratio. However, for ellipsoids with a large aspect ratio or rigid bodies in an arbitrary shape, the method can cause problems, such as particles superposition, and incorrect particle behavior. To deal with particles of arbitrary shape, a more sophisticated collision strategy such as a lubrication model by Maury (1997) is needed.
- 2. To predict particle migrating across streamlines in a unidirectional flow using the mixture model in FLUENT, the constitutive equation for the slip velocity has to be modified to include the lateral force caused by fluid inertia. Rubinow & Keller (1961) suggested to compute this force from

$$F_{L} = \pi (d_{p} / 2)^{3} \rho \omega_{c} \times \mathbf{u}_{c}$$

$$(6.1)$$

The parameters in the above equation are all known except the angular velocity $\omega_{\rm c}$. This unknown quantity can be modeled using the DNS data obtained from the numerical method studied in this work.

3. Code implemented in this work is applied to 2-D cases. There is a possibility to extend the code to 3-D application in the turbulent regime which would be more valuable to validate the mixture model in FLUENT.

4. To increase the computational efficiency, parallel computing technique is necessary. One can use the parallel computing strategy developed by Wang et al. (2008) to implement immersed boundary method discussed in this work to simulate particulate-laden flows.

APPENDICES

APPENDICES

A. Realizable k-\(\epsilon\) equation for two-phase flows

The modified transport equation for k is given as

$$\begin{split} \nabla \cdot \left(\mathbf{u}_{a} \mathbf{k} \right) &= \nabla \cdot (\frac{v_{T}}{\sigma_{k}} \nabla \mathbf{k}) + 2 v_{T} S \nabla \mathbf{u}_{f} - \underbrace{\mathbf{g} v_{T} \nabla \alpha_{p}}_{\text{generation of } k} \\ &\qquad \qquad \text{due to the gravity} \end{split}$$

$$- \underbrace{\frac{\rho_{p}}{\rho_{f} \tau_{w}} (2 \alpha_{p} \mathbf{k} \frac{\tau_{w}}{\tau_{w} + \tau_{l}} + D_{p} \mathbf{u}_{f,p} \nabla \alpha_{p}) - \epsilon}_{\text{dissipation due to the water droplets}} \end{split}$$
 (A-1)

The modified transport equation for ε is presented as

$$\nabla \cdot \left(\mathbf{u}_{f} \varepsilon\right) = \nabla \cdot \left(\frac{v_{T}}{\sigma_{\varepsilon}} \nabla \varepsilon\right) - \underbrace{\frac{\rho_{p}}{\rho_{f} \tau_{w}} (\alpha_{p} \varepsilon \frac{\tau_{w}}{\tau_{w} + \tau_{l}})}_{\text{dissipation due to the water droplets}}$$

$$-C_{2} \frac{\varepsilon}{k + \sqrt{v_{T} \varepsilon}} (\varepsilon + \underbrace{\mathbf{g} v_{T} \nabla \alpha_{p}}_{\text{generation of } \varepsilon})$$

$$\underbrace{\frac{\rho_{p}}{\rho_{f} \tau_{w}} (\alpha_{p} \varepsilon \frac{\tau_{w}}{\tau_{w} + \tau_{l}})}_{\text{generation of } \varepsilon}$$

$$\underbrace{\frac{\rho_{p}}{\rho_{f} \tau_{w}} (\alpha_{p} \varepsilon \frac{\tau_{w}}{\tau_{w} + \tau_{l}})}_{\text{generation of } \varepsilon}$$

$$\underbrace{\frac{\rho_{p}}{\rho_{f} \tau_{w}} (\alpha_{p} \varepsilon \frac{\tau_{w}}{\tau_{w} + \tau_{l}})}_{\text{dissipation due to the water droplets}}$$

$$\underbrace{\frac{\rho_{p}}{\rho_{f} \tau_{w}} (\alpha_{p} \varepsilon \frac{\tau_{w}}{\tau_{w} + \tau_{l}})}_{\text{dissipation due to the water droplets}}$$

$$\underbrace{\frac{\rho_{p}}{\rho_{f} \tau_{w}} (\alpha_{p} \varepsilon \frac{\tau_{w}}{\tau_{w} + \tau_{l}})}_{\text{dissipation due to the water droplets}}$$

$$\underbrace{\frac{\rho_{p}}{\rho_{f} \tau_{w}} (\alpha_{p} \varepsilon \frac{\tau_{w}}{\tau_{w} + \tau_{l}})}_{\text{dissipation due to the water droplets}}$$

where τ_1 is the Lagrangian time-scale, given as

$$\tau_1 = 0.3 \frac{k}{\varepsilon} \tag{A-3}$$

The turbulent viscosity for the air phase is defined as

$$v_{\rm T} = C_{\mu} \frac{k^2}{\varepsilon} \tag{A-4}$$

To ensure the realizability (that is positivity of normal stresses in the flow domain), the turbulent coefficient C_{μ} is computed as follows:

$$C_{\mu} = \frac{1}{A_0 + A_s \frac{k}{\varepsilon} \tilde{S}}$$

$$A_0 = 4.04; \ A_s = \sqrt{6}\cos\phi$$

$$\phi = \frac{1}{3}\cos^{-1}(\sqrt{6}W)$$

$$W = \frac{S_{ij}S_{jk}S_{ki}}{\tilde{S}^3}, \ \tilde{S} = \sqrt{S_{ij}S_{ij}}, \ S_{ij} = \frac{1}{2} \left(\frac{\partial u_j}{\partial x_i} + \frac{\partial u_i}{\partial x_j} \right)$$

The k and ϵ transport equations for two-phase flows are similar to those for single-phase flows except two extra two terms due to existence of the water droplets and the external field such as gravity.

B. Analysis of force acting on a particle

$$\rho_{p}V_{c}\dot{\mathbf{u}}_{c} = \rho_{f} \oint_{\partial S} \boldsymbol{\tau} \cdot \mathbf{n} d\sigma + (\rho_{p} - \rho_{f})V_{c}\mathbf{g}$$
(B-1)

$$I_{c}\dot{\boldsymbol{\omega}}_{c} = \rho_{f} \oint_{\partial S} (\mathbf{X} - \mathbf{x}_{c}) \times (\boldsymbol{\tau} \cdot \mathbf{n}) d\sigma$$
(B-2)

where where ρ_f and ρ_p are the fluid density and the interior structure density, respectively; I_c is the moment of inertia of the object; V_c is the volume of the rigid body; τ is the shear stress tensor and n denotes the outward normal vector of the rigid structure. According to the divergence theorem, the surface integral on the right hand size of Eq. (B-1) and Eq. (B-2) are

$$\oint_{\partial S} \mathbf{\tau} \cdot \mathbf{n} d\sigma = -\int_{S} \mathbf{F} d\mathbf{x} + \frac{d}{dt} \int_{S} \mathbf{u} d\mathbf{x} \tag{B-3}$$

$$\oint_{\partial S} (\mathbf{X} - \mathbf{x}_{c}) \times (\mathbf{\tau} \cdot \mathbf{n}) d\sigma = -\int_{S} (\mathbf{X} - \mathbf{x}_{c}) \times \mathbf{F} d\mathbf{x} + \frac{d}{dt} \int_{S} (\mathbf{X} - \mathbf{x}_{c}) \times \mathbf{u} d\mathbf{x}$$
(B-4)

The first term on the right hand size of Eq. (B-3) and Eq. (B-4) are simply obtained by summing up the force $\mathbf{F}(\mathbf{X}_k)$ and the torque $(\mathbf{X}_k-\mathbf{x}_c)\times\mathbf{F}_k$ for all the Lagrangian points. According to Uhlmann (2003), the second term of Eq. (5.8) is the rate-of-change term which satisfies a rigid-body motion on the structure surface, obtained

$$\frac{\mathrm{d}}{\mathrm{dt}} \int_{\mathbf{S}} \mathbf{u} d\mathbf{x} = V_{\mathbf{c}} \dot{\mathbf{u}}_{\mathbf{c}} \tag{B-5}$$

The second term of Eq. (B-5) is the angular momentum changed due to non-rigid motion of fluid inside the object domain, $d\Omega$. Under the assumption of rigid-body motion inside the object domain, this term is approximated to

$$\frac{\mathrm{d}}{\mathrm{dt}} \int_{\mathbf{S}} (\mathbf{X} - \mathbf{x}_{c}) \times \mathbf{u} d\mathbf{x} = \frac{I_{c}}{\rho_{p}} \dot{\boldsymbol{\omega}}_{c}$$
 (B-6)

BIBLIOGRAPHYS

BIBLIOGRAPHYS

- [1] Abuzeid, S., Busnaina, A.A., and Ahmadi, G. (1991) Wall deposition of aerosol particles in a turbulent channel flow. Journal of Aerosol Science, 22 (1), 43-62.
- [2] Adib, M.A.H.M., Osman, K. and Jong, R.P. (2010) Analysis of blood flow into the main artery via mitral valve: fluid structure interaction model, 2010 International Conference on Science and Social Research.
- [3] ANSYS FLUENT 12.1 Documentation. (2009). Theory Guide.
- [4] Autal, S.P., Lahey, R.T., and Flaherty, J.E., (1991) Analysis of phase distribution in fully developed laminar bubbly two-phase flow, International Journal of Multiphase Flow, 7, 635-652.
- [5] Azzopardi, B.J. (1985) Drop sizes in annular two-phase flow, Experiments in Fluids, 3, 53-59.
- [6] Azzi, A., Friedel, L.and Belaadi, S. (2000) Two-phase gas/liquid flow pressure loss in bends, Forschung im Ingenieurwesen, 65, 309-318.
- [7] Banerjee, S., Rhodes, E. and Scott, D.S. (1967) Film inversion of concurrent two-phase flow in helical coils, AIChE Journal, 13 (1), 189-191.
- [8] Berger, S.A., Talbot, A., and Yao, L.-S. (1983) Flow in curved pipes. Annual Review of Fluid Mechanics, 15, 461-512.
- [9] Beyer R.P. (1992) A computational model of the cochlea using the immersed boundary method, Journal of Computational Physics, 98, 145-162.
- [10] Berrouk A.B., and Laurence D. (2008) Stochastic modeling of aerosol deposition for LES of 90 °bend turbulent flow. International Journal of Heat and Fluid Flow, 29, 1010-1028.
- [11] Boussinesq, J. (1877) "Essai sur la théorie des eaux courantes," Mémoires présentés par divers savants à l'Acad. Sci. Inst. Nat. France, 23, 46-50.
- [12] Brenner, H. (1961) The slow motion of a sphere through a viscous fluid towards a plane surface, Chem Eng Sci, 16, 242–251.
- [13] Breuer, M., Baytekin, H.T., and Matida, E.A. (2006) Prediction of aerosol deposition in 90° bends using LES and an efficient Llagrangian tracking method. Journal of Aerosol Science, 37, 1407-1428.

- [14] Brockmann, J.E. (1993) Sampling and Transport of Aerosol, in Aerosol Measurement: Principles, Techniques, and Applications. Van Nostrand Reinhold: New York.
- [15] Cash, J.R., and Karp, A.H. (1990) A variable order Runge-Kutta method for initial value problems with rapidly varying right-hand sides. ACM Transactions on Mathematical Software, 16, 201-222.
- [16] Chang, S.M., Humphrey, J.A.C., and Modavi, A. (1983) Turbulent flow in a strongly curved u-bend and downstream tangent of square cross-sections. PCH Physico-chemical Hydrodynamics, 4, 243-269.
- [17] Chisholm, D. (1971) Prediction of pressure drop at pipe fittings during two-phase flow, 13th Int. Cong. of Refrigeration, Washington, 2, 781-789.
- [18] Clarke, D., Salas, M., and Hasan, H. (1996) Euler calculations for multi-element airfoils using Cartesian grids. AIAA, 24, 1128-1135.
- [19] Cheng, Y-S., and Wang C-S. (1975) Inertial deposition of particles in a bend. Journal of Aerosol Science, 6, 139-145.
- [20] Crane V. (1957) Flow of fluids through valves, fittings and pipe, Technical Paper, No. 410.
- [21] Crane (1957) Flow of fluids through valves, fittings and pipe, Technical Paper No. 410.
- [22] Crowe C. Sommerfeld, M., and Tsuji, Y. (1998) Multiphase flows with droplets and particles, CRC Press.
- [23] Cunningham, E. (1910) On the velocity of steady fall of spherical particles through fluid medium. Proceedings of the Royal Society, 83, 357-65.
- [24] Dean, W.R. (1928) Fluid motion in a curved channel. Proceedings of the Royal Society-London Series A, 121, 402-420.
- [25] Elghobashi, S. (1991) Particle-laden turbulent flows: direct simulation and closure models, Applied Scientific Research, 48, 301-314.
- [26] Eustice, J. (1910) Flow of water in curved pipes. Proceedings of the Royal Society-London Series A, 84, 107-118.
- [27] Fitzsimmons, D.E. (1964) Two-phase pressure drop in piping components, HW-80970, Rev. 1, General Electric Hanford Laboratories, Richland, OH.
- [28] Fadlun, E.A., Verzicco, R., Orlandi, P., and Mohd-Yusof, J. (2000) Combined immersed-boundary finite-difference methods for three-dimensional complex flow simulations, Journal of Computational Physics, 161, 35-60.

- [29] Fogelson, A. and Peskin, C. (1988) A fast numerical method for solving the three-dimensional Stokes' equations in the presence of suspended particles, Journal of Computational Physics, 79, 50–69.
- [30] Gibson, M.M., and Launder, B.E. (1978) Ground effects on pressure fluctuations in the atmospheric boundary layer. Journal of Fluid Mechanics, 86, 491-511.
- [31] Glowinski, R., Pan, T.-W., Hesla, T., and Joseph, D. (1999) A distributed Lagrange multiplier/fictitious domain method for particulate flows, International Journal of Multiphase Flow, 25, 755–794.
- [32] Goldstein, D. Handler, R., Sirovich, L. (1993) Modeling a no-slip flow boundary with an external force field, Journal of Computational Physics, 105, 354-366.
- [33] Gore, R.A. and Crowe, C.T. (1989) Effect of particle size on modulating turbulent intensity, International Journal of Multiphase Flow, 15, 279- 285.
- [34] Hart, J., Ellenberger, J. and Hamersma, P.J. (1988) Single- and two-phase flow through helically coiled tubes, Chemical Engineering Science, 43 (4), 775-783.
- [35] Hetsroni, G. (1989) Particle-turbulence interaction, International Journal of Multiphase Flow, 15, 735-746.
- [36] Hewitt, G.F. and Robertson, D.N. (1969) Studies of Two-Phase Flow Patterns by Simultaneous X-ray and Flash Photography, Rept AERE-M2159, UKAEA, Harwell.
- [37] Ho, B.P., and Leal, L.G. (1973) Inertial migration of rigid spheres in two-dimensional unidirectional flows, Journal of Fluid Mechanics, 65, 365-400.
- [38] Hoang, K. and Davis, M.R. (1984) Flow structure and pressure loss for two-phase flow in return bends, ASMEJ. Fluids Eng., 106, 30-37.
- [39] Hossain, A. and Naser, J. (2004) CFD investigation of particle deposition around bends in a turbulent flow, 15th Australasian Fluid Mechanics Conference, the University of Sydney, 13-17.
- [40] Höfler, K., and Schwarzer, S. (2000) Navier-Stokes simulation with constraint forces: Finite-difference method for particle-laden flows and complex geometries, Physical Review E, 61 (6), 7146-7160.
- [41] Ishii, M. (1975) Thermo-fluid dynamic theory of two-phase flow (book), Paris: Eyrolles.
- [42] Ito, H. (1959) Friction factors for turbulent flow in curved pipes. ASME Journal of Basic Engineering, 81, 123-134.
- [43] Ito, H. (1987) Flow in curved pipes. JSME International Journal, 30, 543-552.

- [44] Jang, D.S., and Acharya, S. (1988) Calculation of particle dispersion due to turbulence in elliptic flows. AICHE, 34, 514 518.
- [45] Jeffery, G.B. (1922) The motion of ellipsoidal particles immersed in a viscous fluid, Proceedings of the Royal Society A, 102, 161-179.
- [46] Johansen, S.T., Anderson, N.M. and de Silva, S.R. (1990) A two-phase model for particle local equilibrium applied to air classification of powers, Power Technology, 63, 121-132.
- [47] Joseph, D.D., Fortes, A.F., Lundgreen, T.S., and Singh, P. (1987) Nonlinear mechanics of fluidization of beds of spheres cylinders and disks in water, in Advances in Multiphase Flow and Related Problems (Papanicolau, G. ed.), SIAM, 101–122.
- [48] Kim, S.-E., and Choudhury, D. (1995) A near-wall treatment using wall functions sensitized to pressure gradient, ASME, 217, Separated and Complex Flows.
- [49] Kim, J., Kim, D. and Choi, H. (2001) An immersed-boundary finite-volume method for simulations of flow in complex geometries, Journal of Computational Physics, 171 132–150.
- [50] Kim, Y., Lim, S., Raman, S., Simonetti, O.P. and Friedman, A. (2009) Blood flow in a compliant vessel by the immersed boundary method, Annals of Biomedical Engineering, 37 (5), 927-942.
- [51] Kim, Y. and Peskin, C.S. (2006) 2-D parachute simulation by the immersed boundary method. The SIAM Journal on Scientific Computing, 28 (6), 2294-2312.
- [52] Kim, Y. and Peskin, C.S. (2009) 3-D parachute simuation by the immersed boundary method. Computers and Fluids, 38, 1080-1090.
- [53] Kovacs, S. J., McQueen, D. M., and Peskin, C. S. (2001) Modeling cardiac fluid dynamics and diastolic function, Philos. Trans. R. Soc. Lond. Ser. A, 359, 1299–1314.
- [54] Kundu, P.K., and Cohen, M.I. (2004) "Fluid Mechanics," third ed., 686-687.
- [55] Lai, M.-C., and Peskin, C.S. (2000) An immersed boundary method with formal second-order accuracy and reduced numerical viscosity, Journal of Computational Physics, 160, 705-719.
- [56] Launder, B.E., and Sharma, B.I. (1972) Application of the energy dissipation model of turbulent to the calculation of flow near a spinning disc. Letters in Heat and Mass Transfer, 1 (2), 131-138.
- [57] Launder, B.E., and Spalding, D.B. (1974) The numerical computation of turbulent flows. Computer Methods in Applied Mechanics and Engineering, 3, 269-289.

- [58] Launder, B.E., Reece, G.J., and Rodi, W. (1975) Progress in the development of a Reynolds-stress turbulence closure. Journal of Fluid Mechanics, 68 (3), 537-566.
- [59] Lee, C. (2003) Stability characteristics of the virtual boundary method in three-dimensional applications, Journal of Computational Physics, 184, 559–591.
- [60] Liu, C., Zheng, X. and Sung, C. (1998) Preconditioned multigrid methods for unsteady incompressible flows, Journal of Computational Physics, 139, 35-57.
- [61] Lockhart, R.W. and Martinelli, R.C. (1949) Proposed correlation of data for isothermal two-phase flow, two-component flow in pipes, Chem. Eng. Prog., 45(1), 39-45.
- [62] Longest, P.W., and Oldham, M.J. (2008) Numerical and experimental deposition of fine respiratory aerosols: Development of a two-phase drift flux model with near-wall velocity corrections. Journal of Aerosol Science, 39, 48-70.
- [63] MacCormack, R.W. (1969) The effect of viscosity in hypervelocity impact cratering, AIAA paper, 69-354.
- [64] Majumdar, S., Iaccarino, G., and Durbin P.A. (2001) RANS solver with adaptive structured boundary non-conforming grids, Annual Reviews Briefs, Center for Turbulence Research 353–364.
- [65] Mandal S.N. and Das, S.K. (2001) Pressure losses in bends during two-phase gas-Newtonian liquid flow, Ind. Eng. Chem. Res., 40, 2340-2351.
- [66] Manninen, M., Taivassalo, V., Kallio, Sirpa, and Akademi, Å.(1996) On the mixture model for multiphase flow, VTT Publications.
- [67] Matida, E.A., Finlay, W.H., Lange, C.F., and Grgic, B. (2004) Improved numerical simulation of aerosol deposition in an idealized mouth-throat. Journal of Aerosol Science, 35, 1-19.
- [68] Marcus, R., Leung, L., Klinzing, G., and Rizk, F. (1990) Pneumatic Conveying of Solids, Chapman and Hall, London.
- [69] Maury, B. (1997) A many-body lubrication model, C.R. Acad. Sci., Paris, Serie I-Mathematics, 325, 1053-1058.
- [70] Maxey, M.R., and Riley, J.J. (1983) Equation of motion for a small rigid sphere in a nonuniform flow. Physics of Fluids, 26 (4), 883-889.

- [71] McFarland, R.A., Gong, H., Muyshondt, A., Wente, W.B., and Anand, N.K. (1997) Aerosol deposition in bends with turbulent flow. Environmental Science and Technology, 31, 3371-3377.
- [72] McQueen, D. M. and Peskin, C. S. (2001) Heart simulation by an immersed boundary method with formal second-order accuracy and reduced numerical viscosity, in Mechanics for a New Millennium, Proceedings of the International Conference on Theoretical and Applied Mechanics (ICTAM) 2000, H. Aref and J. W. Phillips, eds., Kluwer Academic Publishers, Norwell, MA.
- [73] Miyoshi, M., Mori, K., and Nakamura, Y. (2009) Numerical Simulation of Parachute Inflation Process by IB Method, Journal of the Japan Society for Aeronautical and Space Sciences, 57 (670), 419-425.
- [74] Mohd-Yosuf, J. (1997) Combined immersed boundary/B-spline methods for simulation of flow in complex geometries. Annual Research Briefs, Center for Turbulence Research, 317-328.
- [75] Morsi, S.A. and Alexander, A.J. (1972). An investigation of particle trajectories in two-phase flow systems. Journal of Fluid Mechanics, 55 (2), 193-208.
- [76] Norstebo, (1986) A. Pressure drop in pipe components in two-phase gas-liquid flow, Doctoral Thesis, The Norwegian Institute of Technology, NTH, Division of R.
- [77] Pacull, F. (2006) "A numerical study of the immersed boundary method and application to blood flow," Ph.D. Thesis, University of Houston.
- [78] Paliwoda A. (1992) Generalized method of pressure drop of refrigerants. Rev. Int. Froid, 15 (2), 120-126.
- [79] Patankar, N., Singh, P., Joseph, D., Glowinski, R., and Pan, T.-W. (2000) A new formulation of the distributed Lagrange multiplier/fictitious domain method for particulate flows, International Journal of Multiphase Flow, 26, 1509–1524.
- [80] Patankar, S.V., and Spalding, D.B. (1972) A calculation procedure for heat, mass and momentum transfer in three-dimensional parabolic flows. International Journal of Heat Mass Transfer, 15, 1787-1806.
- [81] Peskin, C.S. (1972) Flow patterns around heart valves: a digital computer method for solving the equations of motion. Ph.D. Thesis, Albert Einstein College of Medicine.
- [82] Peskin, C.S. (2002) The immersed boundary method, Cambridge University Press: Acta Numerica 2002, 11, 479-518.
- [83] Peters, T.M., and Leith, D. (2004) Particle deposition in industrial duct bends. The Annals of Occupational Hygiene, 48 (5), 483-490.

- [84] Perng, C.Y., Street, R.L. (1989) Three-dimensional unsteady flow simulations: Alternative strategies for a volume-averaged calculation. International Journal for Numerical Methods in Fluids, 9 (3), 341-362.
- [85] Perrin, A. and Hu, H.H. (2006) An explicit finite-difference scheme for simulation of moving particles, Journal of Computational Physics, 212, 166-187.
- [86] Picart, A., Berlemont, A. and Gouesbet, G. (1986) Modelling and predicting turbulence fields and the dispersion of discretre particles transported by turbulent flows, Int. J. Multiphase Flow, 12 (2), 237-261.
- [87] Pourahmadi, F. (1982) Turbulence modeling of single-and two-phase curved-channel flows, Ph. D. Thesis, University of California-Berkeley.
- [88] Pui, D.Y.H., Romay-Novas, F., and Liu, B.Y.H. (1987) Experimental study of particle deposition in bends of circular cross section. Aerosol Science and Technology, 7, 301-315.
- [89] Saiki, E. and Biringen, S. (1996) Numerical simulation of a cylinder in uniform flow: application of a virtual boundary method, Journal of Computational Physics, 123, 450–465.
- [90] Schiller, L. and Naumann, Z. (1935) A drag coefficient correlation. Z. Ver. Deutsch. Ing. 77, 318-327.
- [91] Shih, T.-H., Liou, W.W., Shabbir, A., Yang, Z., and Zhu, J. (1995) A New Eddy-Viscosity Model for High Reynolds Number Turbulent Flows-Model Development and Validation, Computers and Fluids, 24, 227–238.
- [92] Sharp, D.H. (1984) An overview of Rayleigh-Taylor instability. Physica D: Nonlinear Phenomena, 12, 3-18.
- [93] Segr & G., Silberberg, A. (1962a.) Behaviour of macroscopic rigid spheres in Poiseuille flow. Part 1, Journal of Fluid Mech. 14, 115-135.
- [94] Segr & G., Silberberg, A. (1962b.) Behaviour of macroscopic rigid spheres in Poiseuille flow. Part 2, Journal of Fluid Mech. 14, 136-157.
- [95] Spurk, J.H. (1997). Fluid Mechanics. Springer: New York.
- [96] Starkey, T.V. (1956) Viscosity and action, British Journal of Applied Physics, 7, 448-450.
- [97] Sookprasong, P. (1980) Two-phase flow in piping components, MSc Thesis, University of Tulsa.

- [98] Repetti, R.V. and Leonard, E.F. (1966) C~hem Engng Frog. Symp. 8cr. 62, 80.
- [99] Rubinow, S.I. and Keller, J.B. (1961) The transverse force on a spinning sphere moving in a viscous fluid, Journal of Fluid Mechanics, 11, 447-459.
- [100] Wolfshtein, M. (1969) The velocity and temperature distribution of one-dimensional flow with turbulence augmentation and pressure gradient, Int. J. Heat Mass Transfer, 12, 301-318.
- [101] Sudo, K., Sumida, M., and Hibara, H. (1998) Experimental investigation on turbulent flow in a circular-sectioned 90-degree bend. Experiments in Fluids, 25, 42-49.
- [102] Sudo, K., Sumida, M., and Hibara, H. (2000) Experimental investigation on turbulent flow through a circular-sectioned 180 °bend. Experiments in Fluids, 28, 51-57.
- [103] Theofanous, T.G. and Sullivan, J. (1982) Turbulence in Two-Phase Dispersed Flows, Journal of Fluid Mechanics, 116, 343-362.
- [104] Tannehill, J.C., Anderson, D.A., and Pletcher, R.H. (1997) "Computational Fluid Mechanics and Heat Transfer," second ed., Taylor & Francis, Washington, DC.
- [105] Thomson, J. (1876) On the origin of windings of rivers in alluvial plains, with remarks on the flow of water round bends in pipes. Proceedings of Royal Society-London Series A, 25, 5-8.
- [106] Tunstall, M.J., and Harvey, J.K. (1968) On the effect of a sharp bend in a fully developed turbulent pipe-flow. Journal of Fluid Mechanics, 34, 595-608.
- [107] Uhlmann, M. (2003) First experiments with the simulation of particulate flows, Technical Report No. 1020, CIEMAT, Madrid, Spain, ISSN 1135-9420.
- [108] Uhlmann, M. (2005) An immersed boundary method with direct forcing for the simulation of particulate flows, Journal of Computational Physics, 209, 448-476.
- [109] Vigmond, E. J., McQueen, D. M. and Peskin, C. S. (2003) The cable as a basis for a mechanoelectric whole heart model, Internat. J. Bioelectromagnetism, 5, 183-184.
- [110] Wang, Z., Fan J., and Luo, K. (2008) Parallel computing strategy for the simulation of particulate flows with immersed boundary method, Science in China Series E: Technological Sciences, 51, 1169-1176.
- [111] Wilson, R.E., Mcadams, W.H., and Seltzer, M. (1922) The flow of fluids through commercial pipelines. The Journal of Industrial and Engineering Chemistry, 14, 105-119.
- [112] Wolfshtein, M. (1969) The velocity and temperature distribution of one-dimensional flow with turbulence augmentation and pressure gradient. International Journal of Heat Mass Transfer, 12, 301-318.

- [113] Wu, J., and Shu, C. (2010) An improved immersed boundary-lattice Boltzmann method for simulating three-dimensional incompressible flows, Journal of Computational Physics, 229, 5022-5042.
- [114] Zhang, P., Roberts, R.M. and Bénard, A. (2012) Computational Guidelines and an Empirical Model for Particle Deposition in Curved Pipes Using an Eulerian-Lagrangian Approach, Journal of Aerosol Science, 53,1-20.
- [115] Zhang, W., Noda, R., Horio, M. (2005) Evaluation of lubrication force on colliding particles for DEM simulation of fluidized bed, 158, 92-101.